UC404
LBL-28965

Center for Advanced Materials

CAM

Scanning Tunneling Microscopy Studies of Chemisorbed Layers on Metal Surfaces

D.M. Zeglinski
(Ph.D. Thesis)

April 1990

For Reference

Not to be taken from this room

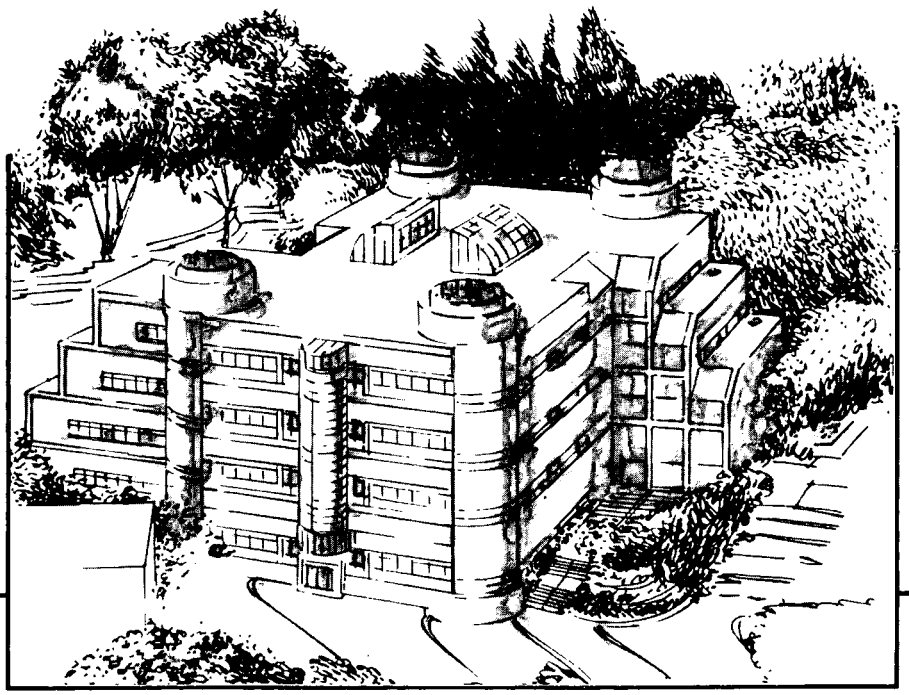

Materials and Chemical Sciences Division

Lawrence Berkeley Laboratory • University of California

ONE CYCLOTRON ROAD, BERKELEY, CA 94720 • (415) 486-4755

Prepared for the U.S. Department of Energy under Contract DE-AC03-76SF00098

LBL-28965
Copy 1
Bldg. 50 Library.

DISCLAIMER

This document was prepared as an account of work sponsored by the United States Government. While this document is believed to contain correct information, neither the United States Government nor any agency thereof, nor the Regents of the University of California, nor any of their employees, makes any warranty, express or implied, or assumes any legal responsibility for the accuracy, completeness, or usefulness of any information, apparatus, product, or process disclosed, or represents that its use would not infringe privately owned rights. Reference herein to any specific commercial product, process, or service by its trade name, trademark, manufacturer, or otherwise, does not necessarily constitute or imply its endorsement, recommendation, or favoring by the United States Government or any agency thereof, or the Regents of the University of California. The views and opinions of authors expressed herein do not necessarily state or reflect those of the United States Government or any agency thereof or the Regents of the University of California.

LBL-28965

Scanning Tunneling Microscopy Studies of Chemisorbed Layers on Metal Surfaces

David Mark Zeglinski

Department of Chemistry
University of California

and

Materials and Chemical Sciences Division
Lawrence Berkeley Laboratory
University of California
Berkeley, CA 94720

This work was supported by the Director, Office of Energy Research, Office of Basic Energy Sciences, Materials Science Division, of the U.S. Department of Energy under Contract No. DE-AC03-76SF00098.

Scanning Tunneling Microscopy Studies of Chemisorbed Layers on Metal Surfaces
copyright ©1990
David Mark Zeglinski

Scanning Tunneling Microscopy Studies of Chemisorbed Layers on Metal Surfaces

David Mark Zeglinski

ABSTRACT

Scanning Tunneling Microscopy (STM) is introduced as a technique for surface studies by outlining the tunneling process, the instrument capabilities, and the experimental requirements. STM theory is summarized, beginning with a simple description of quantum tunneling. Metal-vacuum-metal junction theory is presented using Bardeen's transfer Hamiltonian formalism. Most STM imaging theory is based on this construct. A review of the theoretical work pertaining directly to STM concludes the summary.

STM studies of adsorbates are introduced with a brief description of surface chemical bond classifications, adsorbate interactions and adsorbate concentration effects. Following this is a review of previous STM work done on metal surfaces in Ultra-High Vacuum (UHV). Since the structure of the metal surface itself influences adsorbate geometry, both clean and adsorbate covered surfaces are discussed.

The design and operation of a new STM is described. A review of other designs is presented for comparison. The microscope fits standard UHV systems as an add-on instrument. Sample motion is accomplished by electrical signals, eliminating mechanical feedthroughs. Samples are easily transferred to a modified Varian manipulator for heating and interfacing with other surface science techniques. *In situ* tip replacement and sample transfer in and out of the UHV system is also possible. The techniques, Auger Electron Spectroscopy (AES), and Low Energy Electron Diffraction (LEED) are described since these surface sensitive methods are used to characterize the adsorbate systems studied.

The surface structure of a graphitic carbon overlayer on a Pt(111) single crystal

has been imaged with atomic resolution. The surface appears identical to images obtained on bulk graphite with STM. An attempt is made to correlate these results with a theoretical model for STM imaging of bulk graphite.

The real space surface structure of the sulfur chemisorption series on Re(0001) surfaces has been imaged. While the saturation coverage structure ($(2\sqrt{3}\times2\sqrt{3})$R30°) passivates the surface and can be imaged in air, the sub-saturation coverage structures can only be studied in UHV. The structure of the $\begin{bmatrix} 3 & 1 \\ 1 & 3 \end{bmatrix}$ and $(3\sqrt{3}\times3\sqrt{3})$R30° overlayers has been solved. The p(2×2) structure forming at $\Theta_S = 0.25$ has been imaged. Studies of this low coverage structure have revealed features which are not observable with LEED because of their small domain size. Images in which simultaneous imaging of overlayer and substrate metal are presented and discussed.

Preface

Looking back to when I first arrived at Berkeley, and comparing those memories to my present experience creates a feeling of excitement and sometimes disbelief. I never could have imagined my current situation. This all began with my decision to come to Berkeley for Physical Chemistry graduate studies. Berkeley is such a dynamic and diverse institution, it is impossible to draw from more than a fraction of its resources in four years. I am grateful I was able to scratch the surface. I feel I have grown immensely over the course of my graduate work; both professionally and personally. This work has been a part of my life since I arrived in California. I must express my feelings of sadness and loss as a chapter closes for me. The other side of this is my excitement over the beginning of another, entirely new chapter. I would like to take time now to thank the people who have contributed their time and effort, and in doing so, I feel they are a part of me and this work.

I would like to thank Professor Gabor Somorjai for acting as my thesis advisor in my graduate studies. I admire Gabor's enthusiasm for science and his humor, especially during group meetings. Dr. Miquel Salmeron has been my professional and, at times, personal mentor. I thank him for providing the opportunity to perform research in his group. I cannot express in words what his effort has meant to me. Thank you, Miquel. The software that produced the structure models was provided by, and is commercially available from Dr. Michel Van Hove. Michel has been a wonderful and patient mentor, enabling me through our discussions to grasp some of the complexities associated with surface structure theory. The members of the Somorjai group, past and present, are the reason this research team is one of the best in the world. Gabor, Miquel, and Michel provide stimulus for American and international scientists visiting and working at the laboratory. Dr. Wigbert Seikhaus of Lawrence Livermore National Laboratory was involved at the onset of the project. Wigbert is a master of government funding use and recycling previously-enjoyed lab equipment. His style is appealing, and I hope I have learned from it. While I cannot list everyone, many group members have profoundly influenced my career. Dr. D. Frank Ogletree joined the STM team when I arrived. He continues to work in the group while somehow balancing his responsibilities as Manager of the Lawrence Berkeley Laboratory

Surface Analysis Facility. Frank never ceases to amaze me with his broad and deep knowledge of surface and solid state physics, computer architecture and software design, and beer and wine selection. I will miss Frank very much. Dr. Robert Hwang has shared in the excitement and craziness of my final year at Berkeley. Thank you Bob for intimate scientific, philosophical and personal discussions, STM design improvements, and volleyball. See you in Germany. Frank, Bob, Dr. David Denly (Shell Oil Research), Dr. Thomas Beebe, Amadeo Vasquez-de-Parga, and Pin Chen have contributed phenomenal effort in STM design and/or image acquisition. I thank Frank and Bob for critical reading of this thesis. Also I would like to mention Brian Nasz, Greg Blackman for picnics and softball, Hiroko Ohtani, Dave Kelly for introducing me to UHV techniques, Dr. Bruno Marchon for teaching me French slang, Dr. Carmen Ocal, Dr. Ian Harrison for friendship and rebuilding old Porches, Dan Strongin professional softball player and closet comedian, Gil Vandentop for many good times, clan Beebe in Utah, and finally the many group members (Somorjai and STM subdivision) I enjoyed knowing and sharing research with, but whose names would fill a page or two.

Technically, the staff at the Lawrence Berkeley Laboratory (LBL) numbers among the best in the world. I would like to thank: [Building 62 machine shop] Weyland Wong (sample transfer assembly and manipulator design), Dan Colomb (wobble-stick and much more), Chip Flor, Bob Wright and Tony Tammer, the Building 77 and 25 technical staff, the LBL metal stores staff (thanks Marlin and Wally), [LBL electronics shop] Joe Katz (STM electronics), Mike Press, Jim Severns (electron bombardment heater supply and much more), Hank Brendel, Gary Tabler and Bob Ybarra, [optics shop] Rodney Post (piezo cutting), [vacuum technology] Peter Ruegg, [metallurgy] John Holthuis, James Wu, and John Jacobsen. The facilities support staff is also invaluable. Those I have interacted with, and have kept me on the twisted LBL path are: [purchasing] Sandy Stewart, Paula Conant, and John Lee, [photography and illustration] Doug McWilliams, Steve Adams (instrument and image photography), Gus Lockhart (thesis figure composition), and Bill Bero (line drawings), the administrative staff at Building 66, and all the folks who make LBL a top-notch research facility. Bob McAllister of McAllister Technical Services has also been helpful by

providing machined parts and heated discussions.

Personally, the people mentioned next have been as important to me as my professional friends and colleagues. Thank you Mom and Dad. You may not understand what I do, but you have always encouraged me to educate myself in any way I chose, and I appreciate your desire to receive copies of my publications. I would like to thank Gina Calisesi for teaching me so much about things non-scientific. Thank you Jane Shearrer, Francis Goodwin, Chuck Carden, Dorie Gallinatti, Dr. Steven Wall (lets go MX racing!), Neila Hallenbeck, Lary Heath, Gabrielle Zink, Greg and Marjorie Went, Janet Griffiths, and soon to be Doctor, Judy Speed. Without these people in my life, I would surely be a different person.

This thesis was written using PC-LaTeX on an IBM compatible 80386/7.

Berkeley, April 1990

Contents

I Principles of Scanning Tunneling Microscopy **1**

1 Scanning Tunneling Microscopy Technique **2**
1.1 Introduction 2
1.2 The STM Experiment 3

2 Scanning Tunneling Microscopy Theory **7**
2.1 Introduction 7
2.2 Square Potential Barrier 8
2.3 Metal-Vacuum-Metal Junction 8
2.4 STM Imaging Theory 11

II Scanning Tunneling Microscopy Studies of Overlayer/Metal Systems and Clean Metal Surfaces **15**

3 Overlayer Formation on Metal Substrates **16**
3.1 Introduction 16
3.2 Bonding to Surfaces 17

4 Metal Surfaces: Previous Scanning Tunneling Microscopy Studies **19**
4.1 Introduction 19
4.2 STM Studies of Metal Surfaces in UHV 20

III Scanning Tunneling Microscopy Studies in Ultra-High Vacuum: Instrumentation **22**

5 Design and Construction of a Scanning Tunneling Microscope for Ultra-High Vacuum **23**
5.1 Introduction 23
5.2 Instrument Design Types 26
5.3 A UHV STM for Surface Science Studies 27
5.4 Electronics and Software 48

6 Auger Electron Spectroscopy and Low Energy Electron Diffraction 50
6.1 Introduction 50
6.2 Auger Electron Spectroscopy 50
6.3 Low Energy Electron Diffraction 51

IV Scanning Tunneling Microscopy Studies in Ultra-High Vacuum: Experimental Results 53

7 Incommensurate Graphite on the Pt(111) Surface 54
7.1 Introduction 54
7.2 Overlayer Preparation 59
7.3 STM Results and Discussion 59

8 Sulfur on the Re(0001) Surface 64
8.1 Introduction 64
8.2 Overlayer Preparation 67
8.3 STM Results and Discussion 69

A Design Sketches for the Ultra-High Vacuum Scanning Tunneling Microscopy System. 104

List of Figures

2.1 Square potential barrier. A classical particle with energy less than V_0 would be totally reflected by the barrier. 9

2.2 (a) Trapezoidal barrier. F_1 and F_2 define the Fermi levels of the electrodes, Θ_1 and Θ_2 are the work functions defined as the energy difference between the Fermi level and the vacuum level (dashed line), and eV is the applied voltage. This voltage establishes empty states in one electrode which increase the potential for tunneling. (b) During an STM experiment, the separation, s, is small (5 - 10 Å). The barrier does not maximize at the system vacuum level. It is useful then, to define a local barrier height, ϕ. An electron, depicted as a wave, is shown tunneling from left to right through the barrier. 10

5.1 Conceptual depiction of the STM scanning system. 25

5.2 (a) Cross-section of the STM head. Tips can be exchanged by inserting a "wobble-stick" (see Fig. 5.4) into the inner piezo from the left side. A sample holder (see Fig. 5.7) rests in the quartz tube, and is provided bias voltage by contact with a hanging gold foil strip. 28

5.2 (b) Side view photograph of the STM. This closeup shows the STM head mounted on the stainless steel support plate. 29

5.3 Detailed view of the Vespel tip holder, tip retaining Cu-Be spring, and Pt/Rh tip held in an aluminum collar. 30

5.4 (a) Schematic of the STM head and its support structure mounted to an eight inch conflat flange. Two vibration isolation stages are shown consisting of Cu-Be springs and a stack of stainless steel plates separated by silicone cord. The wobble-stick transfers tips from the carousel opposite the microscope head. Electrical contact is provided by two ten-pin feedthroughs, and a linear motion feedthrough is used to clamp the microscope baseplate for tip and sample transfers. . . . 32

5.4 (b) Side view photograph of the STM. 33

5.4 (c) Perspective view photograph of the STM. 34

5.4 (d) Coaxial view photograph from the instrument's vacuum side. Notice the tip, tip collar, and Vespel holder (see Fig. 5.3). 35

5.4 (e) Coaxial view photograph from the instrument's vacuum side. The sample holder (see Fig. 5.7) is resting in the quartz tube. 36

5.5 (a) Equatorial cross-section of the UHV chamber indicating instrument positions. Sample transfer from air to UHV is accomplished through a $2\frac{3}{4}$ inch flange between the STM and viewport. 37
5.5 (b) Photograph of the chamber along the transfer system axis. 38
5.5 (c) Photograph of the upper chamber section along the viewport axis. 39
5.6 Fourier transform of the in-range Z piezo response prior to scanning. The microscope is in UHV, and the sample is the Re(0001)/S-p(2×2) surface. Tunneling parameters are: -0.1 V sample bias, 2 nA current setpoint, and 50 MΩ gap resistance. This measurement indicates an RMS noise level of 0.3 Å over a bandwidth of 50 kHz. 40
5.7 (a) Sectional view of the sample holder. The sapphire balls are mechanically fastened to the holder. The balls are secured by two stainless steel retaining plates. (b) Perspective view of the sample holder. . . . 42
5.8 The approach/retract voltage waveform is digitally generated, and is basically a sawtooth. The ramp contracts (for sample approach) or expands (for sample retract) the outer piezo tube. 44
5.9 A photograph of the manipulator arm through the STM flange. Visible are the electron bombardment heater filament, and sample clamping lever. The copper V-block used for sample holder cooling is also visible at lower right. The nozzle protruding from the arm supports the sample holder through its bored hole. For sample heating, an electron bombardment heating filament exists in the nozzle, and is controlled by an emission regulated power supply. 46
5.10 Assembly drawing of the sample transfer system. The right flange of the gate valve is mounted to the UHV chamber. The sample holder rests in the basket shown at the end of the transfer rod. 47
7.1 Model for the catalytic thermal dehydrogenation of an adsorbed organic molecule (in this case, ethylene). The alkylidyne species (upper schematic) formed when alkenes are adsorbed at room temperature sit in three-fold hollow sites with the carbon-carbon axis perpendicular to the surface. The final reaction product is a graphitic overlayer. (Figure courtesy of B. E. Bent and M. B. Salmeron.) 55
7.2 Surface side-view depicting carbidic carbon intercalated between a graphite overlayer and the platinum substrate. This model is used to explain the unusually large graphite-platinum bond distance measured by LEED. (Figure courtesy of D. F. Ogletree.) 57
7.3 Graphite surface top view. The second layer is represented by dashed lines. A sites (circled dots) have second layer neighbors, B sites do not, and C sites are the holes in the center of the surface hexagon extending to the second layer. 58
7.4 Auger electron spectrum of the graphitic carbon layer on the Pt(111) surface. The lineshape of the *KVV* carbon transition at 272 eV indicates graphitic surface carbon. 60

7.5 Low energy electron diffraction pattern of the Pt(111)/C(gr) surface taken an 55 eV. The ring-like overlayer spots at long radius in the pattern indicate an incommensurate graphitic overlayer. The first-order substrate spots are visible inside the overlayer spots. This indicates the graphite unit cell (2.46 Å) is smaller than the Pt-Pt unit cell (2.78 Å). 61
7.6 Current image of the Pt(111)/C(gr) surface. The image is 15×15 Å, and clearly indicates the three-fold symmetry observed on high-resolution bulk graphite images. 62
8.1 LEED patterns for the Re(0001)/S overlayer structures. The clean Re(0001) pattern is also given. 70
8.2 Diagrams for the diffraction patterns presented in Figure 8.1. The asterisk represents a reciprocal lattice vector. The ($3\sqrt{3}\times3\sqrt{3}$)R30° pattern is discussed in detail in the text. 71
8.3 (a) Topographic image of the c($\sqrt{3}\times5$) overlayer. The substrate rhenium atoms are visible between the rows of sulfur. A defect in which a sulfur atom has shifted position can be seen in the upper right corner of the image. 72
8.3 (b) A cursor cross section indicates the STM images the sulfur atoms with 3.0 Å corrugation, greater than expected from a hard-sphere model. 73
8.3 (c) This cursor cross section shows rhenium atoms are imaged as ~0.5Å corrugations, greater than expected from a hard-sphere model. 74
8.4 Real space model for the Re(0001)/S-c($\sqrt{3}\times5$) structure. The STM image shows sulfur sits in three-fold hollow sites. The substrate atoms imaged are those between the sulfur rows without sulfur neighbors. . 75
8.5 Substrate lattice mesh overlaid onto the image in Figure 8.3. The lattice points on the mesh agree well with the positions of the rhenium atoms in the image. 77
8.6 (a) p(2×2) overlayer imaged in topographic mode. Clusters of sulfur atoms are imaged at lower left. 78
8.6 (b) Computer graphics magnification of an area at lower right of Figure 8.6(a) showing the p(2×2) structure in detail. 79
8.6 (c) Tetramers of sulfur near an atomically resolved p(2×2) region. . . 80
8.6 (d) Well ordered tetramers of sulfur coexisting with regions of p(2×2). 81
8.6 (e) Two rotational domains of tetramers. The domain orientation angle is approximately 60° suggesting substrate geometry influences overlayer formation. 82
8.7 Real space model for the Re(0001)/S-p(2×2) system. One substrate atom per unit cell lacks sulfur neighbors, and is imaged by STM. . . . 83
8.8 Computer graphics magnification of Figure 8.6(c), lower left. Corrugation enhancements in the corner of each p(2×2) unit cell correspond to rhenium atoms without sulfur neighbors (see Fig. 8.7). 85
8.9 (a) ($3\sqrt{3}\times3\sqrt{3}$)R30° overlayer on the Re(0001) surface. An anti-phase domain boundary exists, traversing the image from center-bottom to center-left. 86

8.9 (b) High resolution image of the $(3\sqrt{3}\times3\sqrt{3})$R30° overlayer. Single atoms are resolved. Sulfur binds as single atoms, and three- and four-atom clusters. 87
8.10 Real space model of the Re(0001)/S-$(3\sqrt{3}\times3\sqrt{3})$R30° surface. The anti-phase domain boundary is also shown. 88
8.11 Fourier transform, using a single-atom basis, of the $(3\sqrt{3}\times3\sqrt{3})$R30° structure depicted as a LEED pattern. 89
8.12 Results from a kinematic calculation for the $(3\sqrt{3}\times3\sqrt{3})$R30° overlayer. The circle radius increases with beam intensity. Along the (11) direction, the spot extinctions and intensity reductions are displayed. 90
8.13 Representative image for some areas of a $(3\sqrt{3}\times3\sqrt{3})$R30° overlayer. Formation of some trimers, even at low local coverage is seen. Areas such as this may explain the coverage range measured by AES. 91
8.14 $\begin{bmatrix} 3 & 1 \\ 1 & 3 \end{bmatrix}$ overlayer. The unit cell basis is formed by sulfur tetramers. . 93
8.15 (a) High resolution image of the $\begin{bmatrix} 3 & 1 \\ 1 & 3 \end{bmatrix}$ overlayer. The lack of a mirror plane encompassing the substrate first and second layers along the minor tetrameric axis is imaged as a larger corrugation for one sulfur atom. This rotational domain is rotated 60° from the domain imaged in Figure 8.14. 94
8.15 (b) Real space model for the Re(0001)/S-$\begin{bmatrix} 3 & 1 \\ 1 & 3 \end{bmatrix}$ system. 95
8.16 (a) Three atom basis for the $\begin{bmatrix} 3 & 1 \\ 1 & 3 \end{bmatrix}$ overlayer. 96
8.16 (b) Real space model for the three atom basis. 97
8.16 (c) Two atom basis for the $\begin{bmatrix} 3 & 1 \\ 1 & 3 \end{bmatrix}$ overlayer. 98
8.16 (d) Real space model for the two atom basis. 99
8.17 (a) Image of the Re(0001)/S-$(2\sqrt{3}\times2\sqrt{3})$R30° surface. 100
8.17 (b) Real space model of the Re(0001)/S-$(2\sqrt{3}\times2\sqrt{3})$R30° surface. . . 101

List of Tables

8.1 Summary of some sulfur chemisorption studies on metal substrates. The superlattice basis consists of one or two atoms, and LEED intensity analysis has indicated sulfur binds in four-fold or three-fold hollow sites. 66
8.2 Sulfur chemisorption on the Re(0001) surface; overlayer structures, annealing temperatures, and coverage ranges from AES. (Table courtesy of D. G. Kelly.) 68
8.3 Summary of STM results for the Re(0001)/S chemisorption system. . 103

Part I

Principles of Scanning Tunneling Microscopy

Chapter 1

Scanning Tunneling Microscopy Technique

1.1 Introduction

Scanning Tunneling Microscopy (STM)[1] takes advantage of the fact that a current can be measured when electrons tunnel through a classically forbidden energy gap between two conducting or semiconducting solids. This current is exponentially proportional to the gap separation and the height of the energy barrier at the tunneling region. Atomic resolution images in real space of many surfaces are obtained with STM. The exponential dependence of the tunneling current on these parameters is the origin of the remarkable vertical resolution (< 0.1 Å) contained in the images. The lateral resolution (~ 1 Å) is related to the electrode geometry. One electrode is typically planar or near-planar. The opposite electrode is a very sharp tip. An STM image consists of a raster of line scans produced by moving the probe tip across the surface. The change in tunneling current or gap separation is measured during each line scan. The best spatial resolution is obtained when tunneling is between the planar surface and an isolated atom on the probe tip. Difficulties arise in the experiment when one attempts to create, control and maintain tunneling conditions. While the tunneling current is sensitive to small changes in the electrode separation, distances of 5–10 Å are required so tunneling current is measurable. Though creation of a stable tunneling gap can be diffucult, methods exist which provide excellent vibration isolation, precise control of the probe tip, and detection of the minute tunneling currents. These aspects

[1] G. Binnig, H. Rohrer, Ch. Gerber, and E. Weibel, *Applied Physics Letters*, vol. 40, p. 178, 1982; *Physical Review Letters*, vol. 49, p. 57, 1982; *Physica*, vol. 109/110b, p. 2075, 1982.

are discussed in more detail in this manuscript.

STM experiments can be performed in many environments and on many samples. The requirements are essentially: the electrode materials must conduct electrons, and the environment must be non-conductive. Since insulating materials possess defects acting as electron traps, this localization of charge creates an electrostatic potential which essentially blocks the tunneling process, and causes the tip to make physical contact with the surface. This contact generally destroys the delicate probe, ending that particular experiment. STM imaging can take place at pressures ranging from several atmospheres to 10^{-10} torr, depending on the needs of the experimental system. Care must be taken in the pressure range from 0.001 to 1 torr, since a plasma discharge can be excited by the relatively high voltages used to operate the instrument. This discharge can severely damage the instrument components and sensing electronics. Operation is also possible in aqueous environments. Since the tunneling current is localized at the microscopic apex of the tip, it is possible to prevent by electrical shielding unwanted conduction through the liquid. Imaging can take place from liquid helium temperature to several hundred degrees celsius. Thermal gradients between sample and tip which disturb the rastering and gap control must be minimized in these studies. While the STM experiment is conceptually simple, the instrumental and theoretical details necessary for obtaining images and interpreting the results can be complicated. Compared to many surface sensitive techniques, STM is in its infancy, and the state-of-the-art changes frequently. Much progress has been made in instrument performance, and new theories can predict the observations. The next section outlines some experimental needs and methods.

1.2 The STM Experiment

Bringing a sample a macroscopic distance away from an STM tip to a distance of several angstroms without physical contact, maintaining that separation during a scan, and rastering the probed tip across the surface is done with piezoelectric transducers (piezos). These devices are formed in various geometries from lead or barium zirconate-titanate ceramics. Rectangular bars or cylindrical tubes are commonly used. The ceramics change dimension in a predictable manner in the presence of an electric

field. This field is created in STM by applying a voltage via a metallic contact. The piezo arrangement in an STM instrument can be calibrated by imaging a surface with a known lattice parameter. For STM, highly-oriented pyrolitic graphite is used frequently. Problems arise when using piezos, since hysteresis and creep reduces the predictability of the piezo motion. All ceramic unit cells in the transducer do not return to their original configuration after a cyclic voltage is applied. Therefore, the piezo may not provide a reproducible starting and ending geometry after a line scan (hysteresis). Creep occurs when the piezo continues to change geometry after voltage changes have ceased. This can be mistaken for thermal drift when imaging. By minimizing the magnitude and duration of high applied voltages, these effects can be essentially eliminated during an STM scan.

Electronic control for STM consists of: a power supply and circuitry for driving the scanning piezos, a bias supply for the sample or tip, feedback circuitry for driving the piezo maintaining the tunneling gap, and an image display system, preferentially computer based. A bias supply is necessary since applying a voltage to one electrode shifts the Fermi level energy relative to the counterelectrode. This increases the number of empty states for tunneling and controls the tunneling direction. There exist many methods for creating a tunneling gap. This work uses piezos and electrical signals for sample approach, and electronic controls are needed in this case. Many variations of these basic requirements exist, and the control system can become very sophisticated. Complexity is not a necessity for obtaining good images. While the system used in these studies is reasonably complex, it is the product of several years of revision and design improvement. The design is described in detail in Part III, and provides many features which allow imaging to occur quickly and reproducibly.

It is very important to isolate an STM system from external disturbances. These disturbances are usually laboratory building vibrations, acoustic noise, high frequency video monitor noise, and electronic noise inherent in the control circuitry. The effect on the experiment is manifested as excitation of the instrument's mechanical resonances, capacitive coupling of noise into the probe tip, and subsequent instability in the tunneling gap. Designing mechanical rigidity into an STM instrument, and isolating it from the environment by a combination of elastomeric, pneumatic

and/or metallic suspension will generally overcome building and acoustic vibrations. Operation in Ultra-High Vacuum (UHV) also aids damping of acoustic noise, but transmission via the UHV chamber structure itself will occur. Therefore, it is usually necessary to isolate an entire UHV-STM system from the laboratory building. Further noise reduction is obtained when the STM electrical cables and preamp circuitry are electrically isolated, and the feedback control bandwidth is adjusted to discriminate external noise. Many solutions exist for noise reduction by electronic means, and can be engineered into the control system. A combination of methods is generally used for vibration isolation and noise reduction in STM, and some experimentation is usually required until an effective system is found for the instrument.

STM is capable of operating in many imaging modes. These range from vibrational and electronic spectroscopy to the commonly used topographic and current modes. The review articles referenced in this manuscript discuss most of these in detail. This work made use of the topographic and current imaging modes. In topographic mode, the tunneling current is held constant by the feedback loop during an STM scan. The piezo controlling the tip motion perpendicular to the surface expands and contracts as needed when the electronics sense corrugation changes transmitted through the probe tip. The changes in perpendicular tip motion are recorded to create an STM image. This mode can provide a precise measure in distance units of the surface corrugations. For high resolution, scanning rates must be low when using this mode. It is necessary to correlate tip velocity with the response time of the feedback loop. This mode is also very sensitive to noise since the feedback loop must compensate for any changes in gap separation whether created by corrugation differences or vibrations. In current mode a constant gap separation is maintained, and changes in tunneling current during a scan form the STM image. This mode allows more rapid scanning of the surface as compared to topographic mode, and results in better signal-to-noise ratios. This mode does not provide an effective measure of corrugation distances since it is difficult to relate current units to spatial dimensions. Also, current mode is not as useful for scanning surfaces with large corrugations since, on these surfaces, tip contact is highly likely during a scan. Using the STM in these modes can provide a large amount

of information on surface topography. Performing other types of STM measurements on the systems studied here would certainly be desirable, and is an area of current interest.

Chapter 2

Scanning Tunneling Microscopy Theory

2.1 Introduction

Some theoretical goals for explaining the STM imaging process are:

- Describing the tunneling current in three dimensions.
- Predicting the X, Y and Z resolution limits.
- Determining the relation between the observed STM image corrugations and the surface electronic structure.
- Determining the effect of adsorbates on the system.

An attempt has been made in this chapter to describe theory for tunneling as it applies to STM. Some theoretical details are presented for clarity, and references are provided should a rigorous description be needed. A review of STM theory[1] prior to 1987 is available. Experimentally, it is found that the STM tunneling current is exponentially dependent on the gap separation and the STM produces images from which atomic dimensions are measurable. It is important for theory to address these observations, and it is necessary to keep this in mind when theory is formulated.

[1] T. E. Feuchtwang and P. H. Cutler, *Physica Scripta*, vol. 35, p. 132, 1987.

2.2 Square Potential Barrier

A simple model describing tunneling, the square barrier, can be solved exactly for the transmission probability of a particle. Following Gasiorowicz[2] by defining a potential (Figure 2.1), $V(x)$, such that

$$\begin{aligned} V(x) &= 0 & x < -a \\ &= V_0 & -a < x < a \\ &= 0 & a < x \end{aligned} \tag{2.1}$$

and considering energies less than V_0, the Schrödinger equation inside the barrier can be written

$$\frac{d^2u(x)}{dx^2} + \frac{2m}{\hbar^2}(E - V_0)u(x) = 0 \tag{2.2}$$

For a particle at $x > a$ the solution of (2.2) is

$$u(x) = Te^{ikx} \tag{2.3}$$

Solving for the transmission probability, T, yields

$$|\,T\,|^2 = \frac{(2k\kappa)^2}{(k^2+\kappa^2)^2\sinh^2 2\kappa a + (2k\kappa)^2} \tag{2.4}$$

Where

$$k^2 = \frac{2mE}{\hbar^2} \tag{2.5}$$

and

$$\kappa^2 = \frac{2m\,|\,E\,|}{\hbar^2} \tag{2.6}$$

This result indicates that transmission or tunneling occurs although the energy is below the barrier. The square barrier is a reasonable starting point for discussing tunneling, but this model can not provide an adequate representation of the experimental STM system. In the next section, tunneling theory in solids will be introduced for a metal-vacuum-metal junction.

2.3 Metal-Vacuum-Metal Junction

A simple model describing this system is illustrated in Fig. 2.2. The goal is to calculate the tunneling current through the junction. A transfer Hamiltonian formalism[3] has

[2] S. Gasiorowicz, *Quantum Physics*, John Wiley & Sons, Inc., p. 84, 1974.
[3] J. Bardeen, *Physical Review Letters*, vol. 6, p. 66, 1961.

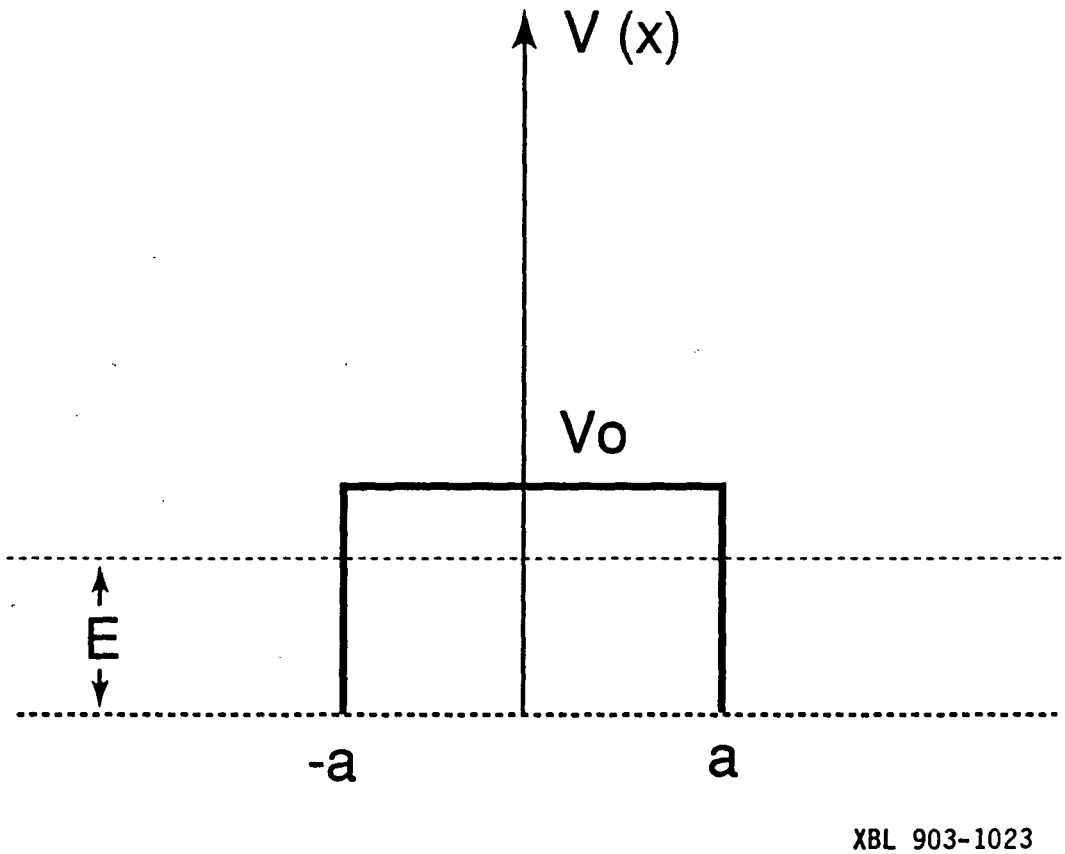

Figure 2.1: Square potential barrier. A classical particle with energy less than V_0 would be totally reflected by the barrier.

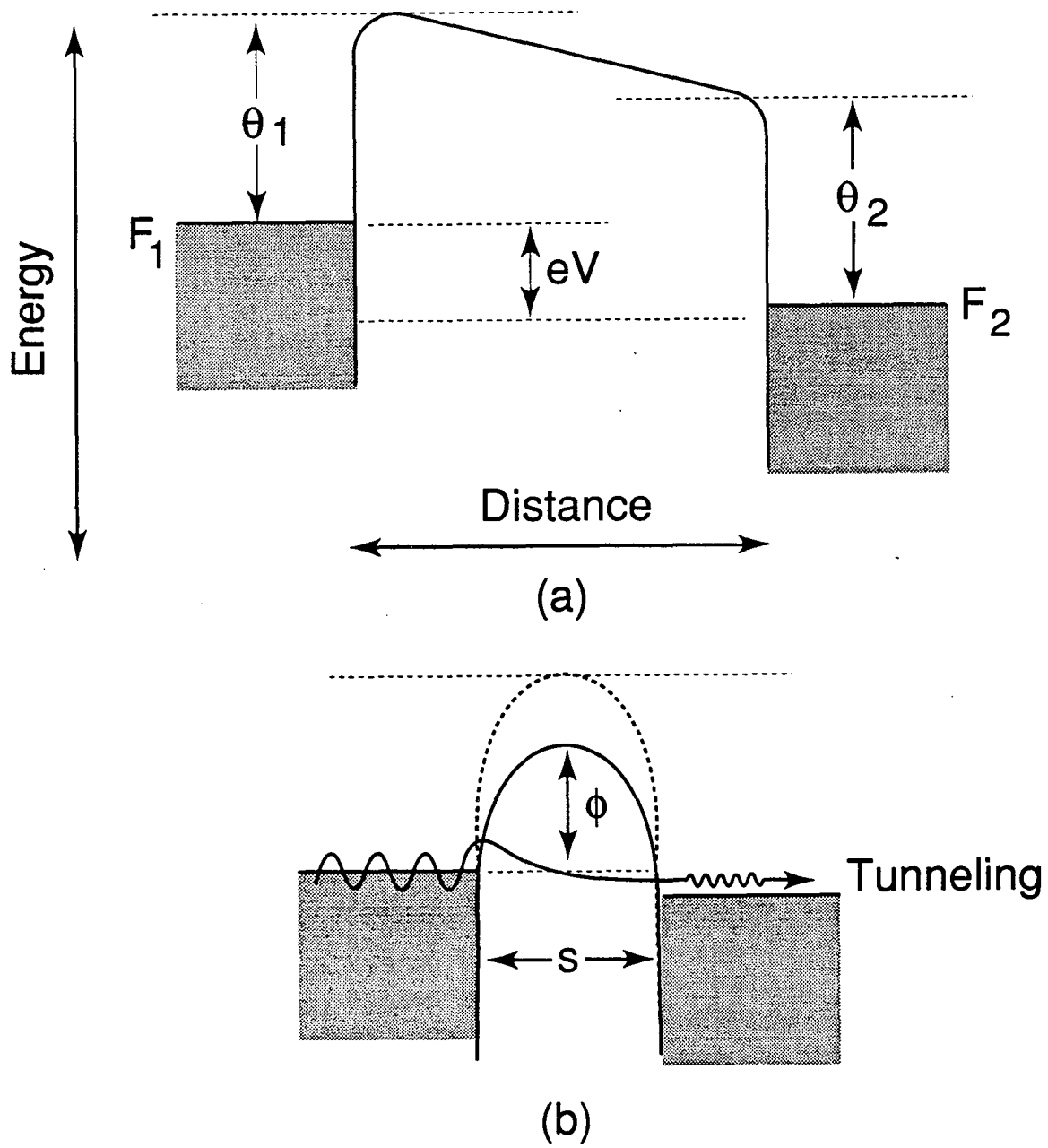

Figure 2.2: (a) Trapezoidal barrier. F_1 and F_2 define the Fermi levels of the electrodes, Θ_1 and Θ_2 are the work functions defined as the energy difference between the Fermi level and the vacuum level (dashed line), and eV is the applied voltage. This voltage establishes empty states in one electrode which increase the potential for tunneling. (b) During an STM experiment, the separation, s, is small (5 - 10 Å). The barrier does not maximize at the system vacuum level. It is useful then, to define a local barrier height, ϕ. An electron, depicted as a wave, is shown tunneling from left to right through the barrier.

been used which consists of writing the matrix element for the tunneling system as

$$M_{LR} = \left\{ \begin{array}{c} \mathcal{H}_L \\ \mathcal{H}_R \end{array} \right\} \tag{2.7}$$

$\mathcal{H}_L$ and $\mathcal{H}_R$ are the Hamiltonians of the left and right electrodes. Both Hamiltonians encompass the vacuum barrier, and M_{LR} represents this generalization. In terms of electrode wave functions, ψ_L and ψ_R,

$$M_{LR} = \frac{\hbar^2}{2m_e} \int d\vec{S} \cdot \left(\psi_L^* \vec{\nabla} \psi_R - \psi_R \vec{\nabla} \psi_L^* \right) \tag{2.8}$$

The integral is calculated over the vacuum region between the electrodes. Solving the Schrödinger equation via first-order perturbation theory[4] for the system leads to an expression for the tunneling current,

$$I = \frac{2\pi e}{\hbar} \sum_{L,R} f(E_L) \left[1 - f(E_R + eV) \right] \mid \mathcal{H}_{LR} \mid^2 \delta(E_L - E_R) \tag{2.9}$$

where $f(E)$, referred to as the Fermi factor, has the form

$$f(E) = \frac{1}{1 + \exp\left[\frac{(E - E_F)}{kT} \right]} \tag{2.10}$$

V is the applied voltage, E_L and E_R are the energies of states ψ_L and ψ_R, and E_F is the Fermi energy. This general form is the analog of the transmission probability presented in the previous section.

2.4 STM Imaging Theory

Since Binnig and Rohrer[5] introduced the STM, theoretical interest in predicting STM images has increased dramatically. In parallel, agreement between theory and experiment has increased. Having introduced tunneling theory in Sections 2.2 and 2.3, a brief review of the theoretical work done on STM will be presented.

Idealized Tip/Sample

Tersoff and Hamann[6] have expanded Bardeen's work by formulating wave functions for the surface electrode, ψ_s, and the STM probe or tip, ψ_t. The general expression

[4] S. Gasiorowicz, *Quantum Physics*, John Wiley & Sons, Inc., p. 341, 1974.
[5] G. Binnig and H. Rohrer, *Helvetica Physica Acta*, vol. 55, p. 726, 1982.
[6] J. Tersoff and D. R. Hamann, *Physical Review B*, vol. 31, p. 805, 1985.

for the surface is

$$\psi_s = \Omega_s^{-\frac{1}{2}} \sum_G a_G \exp\left[\left(\kappa^2 + |\vec{\kappa}_G|^2\right)^{\frac{1}{2}} z\right] \exp(i\vec{\kappa}_G \cdot \vec{x}) \tag{2.11}$$

Where Ω_s is the sample volume, $\kappa = \hbar^{-1}(2m\phi)^{1/2}$ is the inverse decay length for wave functions in the vacuum gap, and ϕ is the barrier height. $\vec{\kappa}_G = \vec{k}_{||} + \vec{G}$, where $\vec{k}_{||}$ is the surface wave vector of the state, and $\vec{G}$ is a surface reciprocal-lattice vector. z is the distance along the surface normal, and is related to the tip/surface separation, s, and the radius of the tip. Electron tunneling is treated as transmission to and from s-states. The tip is modeled as a spherical potential, and its wave function is written

$$\psi_t = \Omega_t^{-\frac{1}{2}} c_t \kappa R e^{\kappa R} (\kappa |\vec{r} - \vec{r}_0|)^{-1} e^{-\kappa|\vec{r}-\vec{r}_0|} \tag{2.12}$$

Ω_t is the probe volume, c_t parameterizes the function, and for this system is of order unity. R is the radius of curvature for the sphere centered at $\vec{r}_0$. For the limits of low temperature and applied voltage, an expression for the tunneling current is obtained using Bardeen's formalism (2.13).

$$I = 32\pi^3\hbar^{-1}e^2 V \phi^2 D_t(E_F) R^2 \kappa^{-4} e^{2kR} \sum_s |\psi_s(\vec{r}_0)|^2 \, \delta(E_s - E_F) \tag{2.13}$$

$D_s(E_F)$ is the density of states per unit volume at the Fermi level of the probe tip.

Tersoff and Hamann's results indicate the STM provides a map of the sample Fermi level local density of states (LDOS) at the spherical tip center. This model can predict results of some experimental systems, but for structures with surface periodicity less than ~ 6Å, such as unreconstructed clean metals and most metal/adsorbate systems, the experimental resolution is not predicted.[7] For the (2x1) and (3x1) reconstructions of the Au(110) surface,[8] a numerical calculation of the tunneling current contour using this model agrees well with experiment.

Lang[9] has performed calculations based on Tersoff and Hamann's approach. The surface is represented by the jellium model,[10] and the tip is represented as an adsorbed atom (Na) on jellium. Na, Ca, and S atoms adsorbed on the surface are found to

[7] C. Julian Chen, submitted to *Physical Review Letters*.

[8] G. Binnig, H. Rohrer, Ch. Gerber, and E. Weibel, *Surface Science*, vol. 131, p. L379, 1983.

[9] N. D. Lang, *Physical Review Letters*, vol. 56, p. 1164, 1986; *IBM Journal of Research and Development*, vol. 30, p. 374, 1986.

[10] C. B. Duke, *Tunneling in Solids*, Academic Press, Inc., p. 15, 1969.

produce an increase in the current at the adsorption site, while adsorbed He creates a slight decrease. This model provides reasonable agreement with experiment[11] but it has been shown[12] that the uniform positive charge density of the jellium model overestimates the extension of the surface wave function in the gap. This would then underestimate the height of the corrugations observed in STM images.

Several authors have developed improvements to these methods. Image potential effects[13] which serve to modify the trapezoidal barrier discussed in Section 2.3 (see Fig. 2.2(b)) have been included in calculations. [14–16] Tersoff and Hamann's approach has been expanded into three dimensions,[17] and Noguera has developed a voltage dependent tunneling current expression.[18] In the next section, theory and calculations which attempt to model the STM junction in a more physically relevant manner will be briefly reviewed.

Towards a Physically Relevant Model

To model the STM tip, Chen[19] has modified Bardeen's theory by writing the tunneling matrix element (2.14) in terms of parabolic coordinates.[20]

$$M_{st} = -\frac{\hbar^2}{2m}\int_{\eta=0}\left[\psi_s^*\frac{\partial\chi_t}{\partial\eta} - \chi_t\frac{\partial\psi_s^*}{\partial\eta}\right]\frac{h_\xi h_\phi}{h_\eta}d\xi d\phi \tag{2.14}$$

The transformation from the parabolic system (ξ, η, ϕ) to cartesian coordinates is $x = \sqrt{\xi\eta}\cos\phi$, $y = \sqrt{\xi\eta}\sin\phi$, and $z = (\xi - \eta)/2$. h_ξ, h_ϕ, and h_η act as scaling factors. The tip and surface wave functions are expanded to include spherical harmonics. From the tunneling current expression obtained, current images are calculated. Considering the permutations of tunneling via single s, p_x, and p_y states on the tip and sample, remarkably different image features are predicted. It seems then, the atomic resolution

[11] G. Doyen, D. Drakova, E. Kopatzki, and R. J. Behm, *Journal of Vacuum Science and Technology A*, vol. 6, p. 327, 1988.
[12] A. J. Bennett and C. B. Duke, *Physical Review*, vol. 188, p. 1060, 1968.
[13] N. M. Miskovsky, P. H. Cutler, and T. E. Feuchtwang, *Applied Physics*, vol. A27, p. 139, 1982.
[14] N. Garcia, C. Ocal, and F. Flores, *Physical Review Letters*, vol. 50, p. 2002, 1983.
[15] J. Bono and R. H. Good, Jr., *Surface Science*, vol. 151, p. 543, 1985.
[16] H. Morawitz, I. P. Batra, R. Reinisch, G. R. Henry, *Surface Science*, vol. 180, p. 333, 1987.
[17] I. P. Batra and H. Morawitz, submitted to *Physical Review B*.
[18] C. Noguera, *Journal of Microscopy*, vol. 152, p. 3, 1988.
[19] C. Julian Chen, *Journal of Vacuum Science and Technology A*, vol. 6, p. 319, 1988.
[20] E. Schrödinger, *Annales de Physique*, vol. 4-80, p. 438, 1926.

obtained by STM can result from tunneling via p states or sp hybrid states on the sample or the tip.

Doyen *et. al.*[11] have calculated tunnel current contours for the (2x1) oxygen induced reconstruction of the Ni(110) surface.[21] The tungsten tip was modeled using $6s$ orbitals. $5d$ orbitals were found to contribute to the LDOS but were not included in the calculation. For the sample system, delocalized sp hybrids represented the nickel surface, and the $3s$ oxygen orbital described the adsorbate. Their calculation predicts a change in the constant tunnel current contour at the adsorption site, as observed experimentally.

Recently, it has been argued that the forces between the sample and impurities present on the tip during imaging are responsible for the atomic resolution imaging of close-packed metal surfaces.[22] This approach has produced results in excellent agreement with the experimental data reported for the Al(111) surface.[23] In contrast, Chen[7] has expanded s surface states in terms of their second-order Fourier components, and has modeled the tungsten tip as a d_{z^2} state. This approach also shows good agreement with the Al(111) results. Integration of these efforts appears to be necessary. Ciraci *et. al.*[24] have proposed a theory which includes *ab initio* calculations of electronic structure, total energy and forces. Chen[25] is approaching the problem along similiar lines. For STM, a critical need is theoretical understanding and prediction of experimental results. Interest in this aspect of the technique has increased, and experimental results are frequently predicted by the new theories.

[21] A. M. Baro, G. Binnig, H. Rohrer, Ch. Gerber, E. Stoll, A. Baratoff, and F. Salvan, *Physical Review Letters*, vol. 52, p. 1304, 1984.

[22] N. J. Zheng and I. S. T. Tsong, *Physical Review B*, vol. 41, p. 2671, 1990.

[23] J. Wintterlin, J. Wiechers, H. Brune, T. Gritsch, H. Hofer, and R. J. Behm, *Physical Review Letters*, vol. 62, p. 2879, 1989.

[24] S. Ciraci, A. Baratoff, and I. P. Batra, *Physical Review B*, vol. 41, p. 2763, 1990.

[25] C. Julian Chen, IBM T. J. Watson Research Center, Yorktown Heights, NY, *private communication.*

Part II

Scanning Tunneling Microscopy Studies of Overlayer/Metal Systems and Clean Metal Surfaces

Chapter 3

Overlayer Formation on Metal Substrates

3.1 Introduction

One of the goals of surface studies is to understand the surface chemical bond. Knowledge of bulk and adsorbate physics and chemistry is the usual beginning when one attempts to understand this problem.[1] In this chapter, only the adsorbate-substrate interaction will be discussed, but it is very important to remember that this specific interaction is an integral part of the entire substrate and overlayer system. Surface bonding is traditionally divided into two types: (i) Physical adsorption or colloquially, physisorption; (ii) Chemical adsorption (chemisorption). The boundary between the two is diffuse at best. Generalizations can be used to distiguish the two phenomena, but care must be taken here. Surface bonding is very complex and not well understood. Therefore, it may be best to avoid generalizations altogether when discussing surface bonding. The bonding interaction between adsorbate and surface is one part of the problem. The geometry of the overlayer is also very important since knowledge of the spatial arrangement gives clues to the surface-adsorbate and adsorbate-adsorbate interactions. It has been found that on single crystal surfaces, adsorbates tend to order spatially, and it is generally believed that the adsorbate-adsorbate interaction is the driving force in ordered overlayer formation.

[1]This is used for modeling the adsorbate-substrate geometry in Part IV.

3.2 Bonding to Surfaces

Physical Adsorption

The physisorption interaction is essentially a van der Waals attraction on the order of 0.5 eV. In studies on the Pd(100)/Xe system,[2] and the Nb(100)/Ar system[3], xenon and argon form a hexagonal close-packed arrangement. This is considered to be the general overlayer geometry in physisorption, but some exceptions exist.[4] It is assumed that since the adsorption energy is small, the surface periodicity does not produce epitaxial overlayers. The substrate structure may influence the overlayer orientation, but the superlattice configuration is mainly due to adsorbate-adsorbate interactions.

Chemical Adsorption

Chemisorption is the actual formation of a chemical bond; either an ionic or covalent interaction. Adsorption energies fall over a wide range. This strong interaction plays a critical role in overlayer structure. Adsorption sites become important and adsorbate concentration affects bonding in many cases. Rather than continuing with an extensive discussion of previous work on chemisorption systems, the experimental results presented in Part IV are used as an example.

Adsorbate Interactions and Ordering

Surface species interactions can be categorized as adsorbate-adsorbate or adsorbate-substrate. These interactions are complex, and provide the driving force for adsorbate ordering and chemical reactions occuring at surfaces. For physisorbed systems, the adsorbate-substrate interaction is van der Waals, and generally weak. Chemisorbed systems possess strong covalent, and/or ionic interactions. Adsorbate ordering can be correlated with three-dimensional crystal growth, *i.e.* the preferred adsorbate-substrate interaction site on a crystal surface often represents the bulk lattice continuation. This implies barriers exist for diffusion of the adsorbate across the surface.

[2] P. W. Palmberg, *Surface Science*, vol. 25, p. 598, (1971).

[3] J. M. Dickey, H. H. Farrell, and M. Strongin, *Surface Science*, vol. 23, p. 448, (1970).

[4] *c.f.* H. Ohtani, C.-T. Kao, M. A. Van Hove, and G. A. Somorjai, *Progress in Surface Science*, vol. 23, p. 155, 1986, and references therein.

It has been shown that adsorbate-substrate interactions modify or reconstruct the crystal surface layer, and may play an important role in catalytic and other surface reactivities.[5] Generally, adsorbate-adsorbate interactions are weak compared to adsorbate-substrate binding forces. Covalent bonding, orbital-overlap, electrostatic forces, and van der Waals forces are important in adsorbate-adsorbate interactions. These forces are known to influence long-range order in an overlayer system. At low adsorbate concentration, interaction between overlayer species is minimal. As coverage increases, adsorbate-adsorbate repulsion can prevent chemical bond formation between individual species. For some species, direct chemical interaction occurs resulting in clustering, or as seen in Part IV, an adsorbate existing atomically at low concentration can form ordered arrays of molecules at high concentration. This interaction is surprising, but with further STM studies of high coverage overlayers, the phenomenon may represent a general trend.

[5] G. A. Somorjai and M. A. Van Hove, *Progress in Surface Science*, vol. 30, p. 201, 1989.

Chapter 4

Metal Surfaces: Previous Scanning Tunneling Microscopy Studies

4.1 Introduction

Since the invention of scanning tunneling microscopy (STM),[1] much work has been done on graphite[2] and semiconductor[3] surfaces in vacuum. Only recently have images of metal surfaces been taken with resolution comparable to that obtained on the non-metallic surfaces. Initially, adsorbate covered metals were imaged. Some studies were done on clean metal surfaces, but atomic resolution was not achieved. As research groups' skills increased, atomic resolution images of clean metal surfaces were obtained. At present, it seems easier to image an adsorbate/metal system. This may be due to a combination of electronic effects introduced by the adsorbate, and tip/sample interactions. The theoretical evidence for this will be mentioned in Part II. The next two sections will detail some results in which atomic resolution was obtained from metal substrates in ultra-high vacuum (UHV).

[1] G. Binning, H. Rohrer, Ch. Gerber, and E. Weibel, *Applied Physics Letters*, vol. 40, p. 178, 1982; *Physical Review Letters*, vol. 49, p. 57, 1982; *Physica*, vol. 109/110b, p. 2075, 1982.

[2] *c.f.* E. Ganz, K. Sattler, and J. Clarke, *Journal of Vacuum Science and Technology A*, vol. 6, p. 419, 1988.

[3] *c.f.* H. Tokumoto, K. Miki, H. Murakami, H. Bando, M. Ono, and K. Kajimura, *Journal of Vacuum Science and Technology A*, vol. 8, p. 255, 1990.

4.2 STM Studies of Metal Surfaces in UHV

Adsorbate Covered Metal Surfaces

Baró *et. al.* obtained the first STM image of an non-metallic adsorbate on a metal surface in UHV. Their study of the O/Ni(100) system produced somewhat crude images from which the 2x1 reconstruction could be discerned.[4] The p(2×2)2H overlayer on Ni(111) has been imaged by van de Walle *et. al.*[5] Since the Ni(111) surface is not known to reconstruct, the observed graphite-like superlattice was attributed to two hydrogen atoms per unit cell adsorbed in different surface sites, *i.e.* one atom in the bABC or hcp site and one atom in the cABC or fcc site. Benzene and CO coadsorbed on the Rh(111) surface as a c($2\sqrt{3}\times4$)rect overlayer has been studied with STM.[6] The atomic resolution images obtained were found to agree well with dynamical LEED analysis done previously.[7] Adsorbed oxygen on the Al(111) surface[8] was found to create atomic scale depressions at -40 mV sample bias and 16 nA tunnel current in agreement with several theoretical studies[9,10] discussed in Part II. A p(2×2) and c(4×2) sulfur superlattice has been imaged on two stepped (Cu(11,1,1) and Cu(8,1,0)) surfaces,[11] and the Cu(110)/O-(2×1) structure has been well studied by Kuk *et. al.*[12] While the number of studies performed on these systems is not as great as those done on non-metallic surfaces, their importance in surface processes is well known, and should provide sufficient incentive for further adsorbate/metal substrate system imaging.

---

[4] A.M. Baró, G. Binnig, H. Rohrer, Ch. Gerber, E. Stoll, A. Baratoff, and F. Salvan, *Physical Review Letters*, vol. 52, p. 1304, 1984.

[5] G.F.A. van de Walle, H. van Kempen, P. Wyder, and C.J. Flipse, *Surface Science*, vol. 181, p. 27, 1987.

[6] S. Chiang, R.J. Wilson, C.M. Mate, and H. Ohtani, *Journal of Microscopy*, vol. 152, p. 567, 1988.

[7] M.A. Van Hove, R.F. Lin, and G.A. Somorjai, *Journal of the American Chemical Society*, vol. 108, p. 2532.

[8] J. Wintterlin, H. Brune, H. Höfer, and R.J. Behm, *Applied Physics A*, vol. A47, p. 99, 1988.

[9] N.D. Lang, *Physical Review Letters*, vol. 56, p. 1164, 1986; *IBM Journal of Research and Development*, vol. 30, p. 374, 1986.

[10] G. Doyen, D. Drakova, E. Kopatzki, and R.J. Behm, *Journal of Vacuum Science and Technology A*, vol. 6, p. 327, 1988.

[11] S. Rousset, S. Gauthier, O. Siboulet, W. Sacks, M. Belin, and J. Klein, *Journal of Vacuum Science and Technology A*, vol. 8, p. 302, 1990.

[12] F.M. Chua, Y. Kuk, and P.J. Silverman, *Physical Review Letters*, vol. 63, p. 386, 1989.

Clean Metal Surfaces

Some workers have obtained atomic resolution images of reconstructed metal surfaces[13] where the corrugations are generally large (*i.e.* larger than those on a close-packed surface). Since the corrugation on close-packed, single crystal, metal surfaces is generally small ($\sim$0.2 Å), obtaining atomic resolution images of these surfaces usually requires more effort. Also, some theoretical results[14] may have inadvertantly discouraged attempts[15] to image these surfaces on an atomic scale. Through results obtained on close-packed metal surfaces, the resolution capabilities of STM have been demonstrated. Atomic resolution has been obtained on the Au(111),[16] Al(111),[17] and Cu(111) surfaces.[18] Atomic resolution of the substrate has not been attempted in this study, but from these results it certainly seems possible, and is an area to which some effort could be devoted.

[13] *c.f.* R. J. Behm, W. Hösler, E. Ritter, and G. Binnig, *Physical Review Letters*, vol. 56, p. 228, 1986.

[14] J. Tersoff and D. R. Hamann, *Physical Review B*, vol. 31, p. 805, 1985.

[15] C. Julian Chen, IBM T.J. Watson Research Center, Yorktown Heights, NY, *private communication.*

[16] V. M. Hallmark, S. Chiang, J. F. Rabolt, J. D. Swalen, and R. J. Wilson, *Physical Review Letters*, vol. 59, p. 2879, 1987.

[17] J. Wintterlin, J. Wiechers, Th. Gritsch, H. Höfer, and R. J. Behm, *Journal of Microscopy*, vol. 152, p. 423, 1988.

[18] D. D. Chambliss and R. J. Wilson, *Bulletin of the American Physical Society*, vol. 35, p. 579, 1990.

Part III

Scanning Tunneling Microscopy Studies in Ultra-High Vacuum: Instrumentation

Chapter 5

Design and Construction of a Scanning Tunneling Microscope for Ultra-High Vacuum

5.1 Introduction

Typically, STM designs[1-6] are system specific,[7-9] and in general, adapting these instruments for surface science studies in commercial UHV chambers is difficult. The studies performed here require the preparation and characterization of ordered surface structures. This necessitates performing the experiments in UHV so that the traditional surface science techniques, Auger Electron Spectroscopy (AES) and Low Energy Electron Diffraction (LEED), can be used to provide information on surface chemical composition and long range order. An STM instrument must then permit transfer of samples from the microscope to the AES and LEED equipment. Sur-

[1] R.M. Feenstra, W.A. Thompson, and A.P. Fein, *Physical Review Letters*, vol. 56, p. 608, 1986; *Journal of Vacuum Science and Technology A*, vol. 4, p. 1315, 1986.

[2] J.A. Golovchenko, *Science*, vol. 232, p. 48, 1986.

[3] S. Chiang, R.J. Wilson, Ch. Gerber, and V.M. Hallmark, *Journal of Vacuum Science and Technology A*, vol. 6, p. 386, 1987.

[4] D.W. Abraham, H.J. Mamin, E. Gantz, and J. Clarke, *IBM Journal of Research and Development*, vol. 30, p. 493, 1986.

[5] J.E. Demuth, R.J. Hamers, R.M. Tromp, and M.E. Welland, *IBM Journal of Research and Development*, vol. 30, p. 397, 1986.

[6] M. Salmeron, B. Marchon, S. Ferrer, and D.S. Kaufman, *Physical Review B*, vol. 35, p. 3036, 1987.

[7] B. Drake, R. Sonnenfeld, J. Schneir, P.K. Hansma, G. Slough, and R.V. Coleman, *Review of Scientific Instruments*, vol. 57, p. 441, 1986.

[8] S.A. Elrod, A.L. de Lozanne, and C.F. Quate, *Applied Physics Letters*, vol. 45, p. 1240, 1984.

[9] A.P. Fein, J.R. Kirtley, and R.M. Feenstra, *Review of Scientific Instruments*, vol. 58, p. 1806, 1987.

face preparation requires the ability to heat samples to approximately 2000 °C. For practical considerations, tip replacement and sample transfer from air to the vacuum chamber are needed without exposing the entire chamber to air. The instrument described here will mount into a standard vacuum chamber with an off-axis manipulator. The sample can be disconnected electrically from the STM *in situ* so that the manipulator can perform the transfer motions. The Appendix contains the original sketches for the microscope and related components.

The scanning portion of the instrument is depicted conceptually in Figure 5.1. The microscope design uses two concentric piezo tubes.[10] This geometry has been used previously for temperature dependent studies in air.[11] The tubes' outer electrodes are sectored into four equal quadrants in order to provide X-Y motion. The inner electrodes provide Z-displacement. The tip is held and scanned by the inner tube. The outer tube serves two functions: approach of the sample to the tip and large-scale sample displacement (2.5 μm for X and Y; 1.5 μm for Z). For both tubes, gain can range from 15 to 25 Å/V. Due to variations in piezo manufacture and sectoring, each tube must be individually calibrated for maximum accuracy. A graphite sample is imaged in UHV to calibrate the STM. The microscope is mounted on an eight inch conflat flange, and operates in conjunction with a vertical off-axis sample manipulator, a front view LEED screen, and a single-pass cylindrical mirror analyzer (CMA) for Auger electron analysis. LEED and AES will be discussed in more detail in the next chapter. Sample transfer from air to UHV is done through a turbopumped airlock, and *in vacuo* replacement of up to six tips is possible.

In the following sections, a brief review of other instrument designs will be presented. The microscope head, vibration isolation system, sample and tip transfer, sample manipulator, and electronics/software package will be discussed in detail, and STM operation will be described.

[10] G. Binnig and D. P. E. Smith, *Review of Scientific Instruments*, vol. 58, p. 1688, 1986.

[11] J. W. Lyding, S. Skala, R. Brockenbrough, J. S. Hubacek, and G. Gammie, *Journal of Microscopy*, vol. 152, p. 371, 1988.

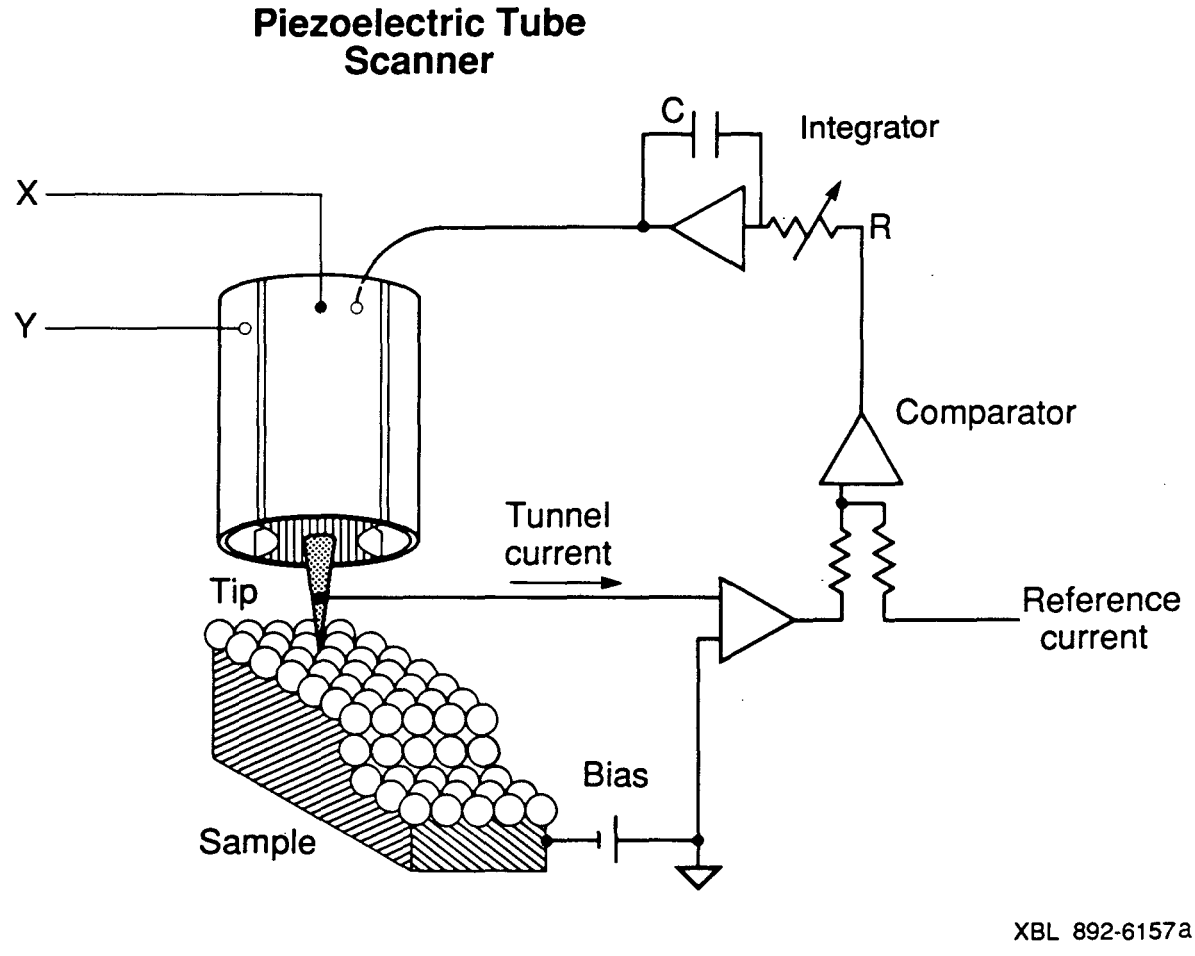

Figure 5.1: Conceptual depiction of the STM scanning system.

5.2 Instrument Design Types

Several authors[12–17] have provided extensive reviews of STM as a technique. This section concentrates on the instrument geometries used by most STM groups. Some design considerations for scanning tunneling microscopes are: high mechanical resonance frequency, a vibration isolation system[18–22] capable of substantially reducing external disturbances (> -100 dB acceleration at $\geq$ 10 Hz is desirable), an X-Y scanning range of $\sim 1\mu$m with a sensitivity of at least 1 Å, a Z scanning range of 1μm with resolution 0.1 Å or better, and a reliable sample approach system.

The original design by Binnig *et. al.*[23] consisted of three orthogonal piezo bars mounted to a plate assembly vibrationally isolated by pneumatic tubes and magnetic levitation. Sample approach was accomplished by an electrostatic walker.[24] Piezo tubes have been used instead of bars,[25,26] and the entire tripod arrangement can be replaced by a single piezo tube.[10] Other methods of sample approach are: a differential micrometer system acting on a reduction lever;[6] a micrometer pressing a differential spring.[9] Variations of these designs have been used in the laboratory, but the instrument[27] described in the next section has performed best in the UHV chamber.

---

[12]G. Binnig and H. Rohrer, *IBM Journal of Research and Development*, vol. 30, p. 355, 1986.
[13]J. A. Golovchenko, *Science*, vol. 232, p. 48, 1986.
[14]P. K. Hansma and J. Tersoff, *Journal of Applied Physics*, vol. 61, p. R1, 1986.
[15]J. E. Demuth, U. K. Koehler, and R. J. Hamers, *Journal of Microscopy*, vol. 152, p. 299, 1988.
[16]Y. Kuk and P. J. Silverman,*Review of Scientific Instruments*, vol. 60, p. 165, 1989.
[17]F. Ogletree and M. Salmeron, *Progress in Solid State Chemistry*, Pergamon Press, in press.
[18]*Shock and Vibration Handbook*, Edited by C. M. Harris and C. E. Crede, McGraw-Hill Inc., 1976.
[19]R. W. Little, *Elasticity*, Prentice-Hall Inc., 1973.
[20]S.-I. Park and C. F. Quate, *Review of Scientific Instruments*, vol. 58, p. 2004, 1987.
[21]D. W. Pohl, *IBM Journal of Research and Development*, vol. 30, p. 417, 1986.
[22]G. Binnig, N. Garcia, and H. Rohrer, *Physical Review B*, vol. 32, p. 1336, 1985.
[23] G. Binnig, H. Rohrer, Ch. Gerber, and E. Weibel, *Applied Physics Letters*, vol. 40, p. 178, 1982; *Physical Review Letters*, vol. 49, p. 57, 1982; *Physica*, vol. 109/110b, p. 2075, 1982.
[24]G. Binnig and Ch. Gerber, *IBM Technical Disclosure Bulletin*, vol. 22, p. 2897, 1979.
[25]Y. Kuk and P. J. Silverman, *Applied Physics Letters*, vol. 48, p. 1597, 1986.
[26]S. Chiang and R. J. Wilson, *IBM Journal of Research and Development*, vol. 30, p. 515, 1986.
[27]D. M. Zeglinski, D. F. Ogletree, T. P. Beebe, Jr., R. Q. Hwang, G. A. Somorjai, and M. B. Salmeron, submitted to *Review of Scientific Instruments*.

5.3 A UHV STM for Surface Science Studies

Microscope Head

The STM head consists of piezoelectric tubes[28] and a quartz sample holder (Fig. 5.2). The assembly is supported by a stainless steel plate. The head is fastened by machine screws to the plate through a Vespel[29] ring. Of the various ultra-high vacuum compatible polyimides available, Vespel was found to perform best due to its excellent machinability, high melting point (300 °C), and negligible outgassing at lower temperatures. Both piezo tubes are mounted to the Vespel ring with Torr-Seal[30] epoxy. The ring is designed so that the scan and approach/offset tubes are separable. This facilitates repair should only one tube require it. Tip wires are held by an aluminum collar which mates with a Vespel holder epoxied to the scan tube. The Vespel holder contains a 0.015 inch diameter, "M" shaped Cu-Be wire spring[31] that serves to retain the aluminum collar and provides electrical contact for the tip (Fig. 5.3). The tubular quartz sample support is joined with Torr-Seal to the offset/approach tube by a Vespel ring. A 0.0005 inch thick gold foil strip is epoxied to the top of the quartz tube. The foil hangs inside the quartz tube (see Fig. 5.2) making electrical contact with the tantalum sample holder. The light-weight foil does not interfere with the sample approach motion, and is not physically attached to the sample holder, allowing sample transfer.

Electrical contact to all piezo sectors, the Cu-Be tip retainer and the gold foil bias contact is provided by 0.006 inch diameter Kapton coated copper wire[31] soldered[32] to each electrode. This method is preferred since it is UHV compatible, bakeable, and provides a durable electrical contact. Electrical shielding for the wires is provided by passing the wires through a silver-coated, copper shield braid,[33] which is electri-

[28] Channel Industries, Inc., Santa Barbara, CA. Channel 5500, 0.875 inch outside diameter × 0.500 inch long × 0.040 inch wall (approach/offset tube). Channel 5500, 0.500 inch outside diameter × 0.500 inch long × 0.040 inch wall (scan tube).

[29] E.I. DuPont de Nemours & Co., Wilmington, DE. Vespel SP1 rod.

[30] Varian Associates, Vacuum Products Division, Lexington, MA.

[31] California Fine Wire Co., Grover City, CA.

[32] Eutectic Co., Flushing, NY. EutecRod 157. This is UHV compatible solder consisting of ~98% Ag, and contains no Cd, Zn or low melting point metals. Acid flux must be used during soldering, and a conventional soldering iron is sufficient for attaching the 0.006 inch wire to the piezos.

[33] Alpha Wire Co., Elizabeth, NJ. $\frac{1}{16}$ inch inside diameter. This method is preferred since it eliminates virtual leaks which could occur from tightly wound coaxial cable.

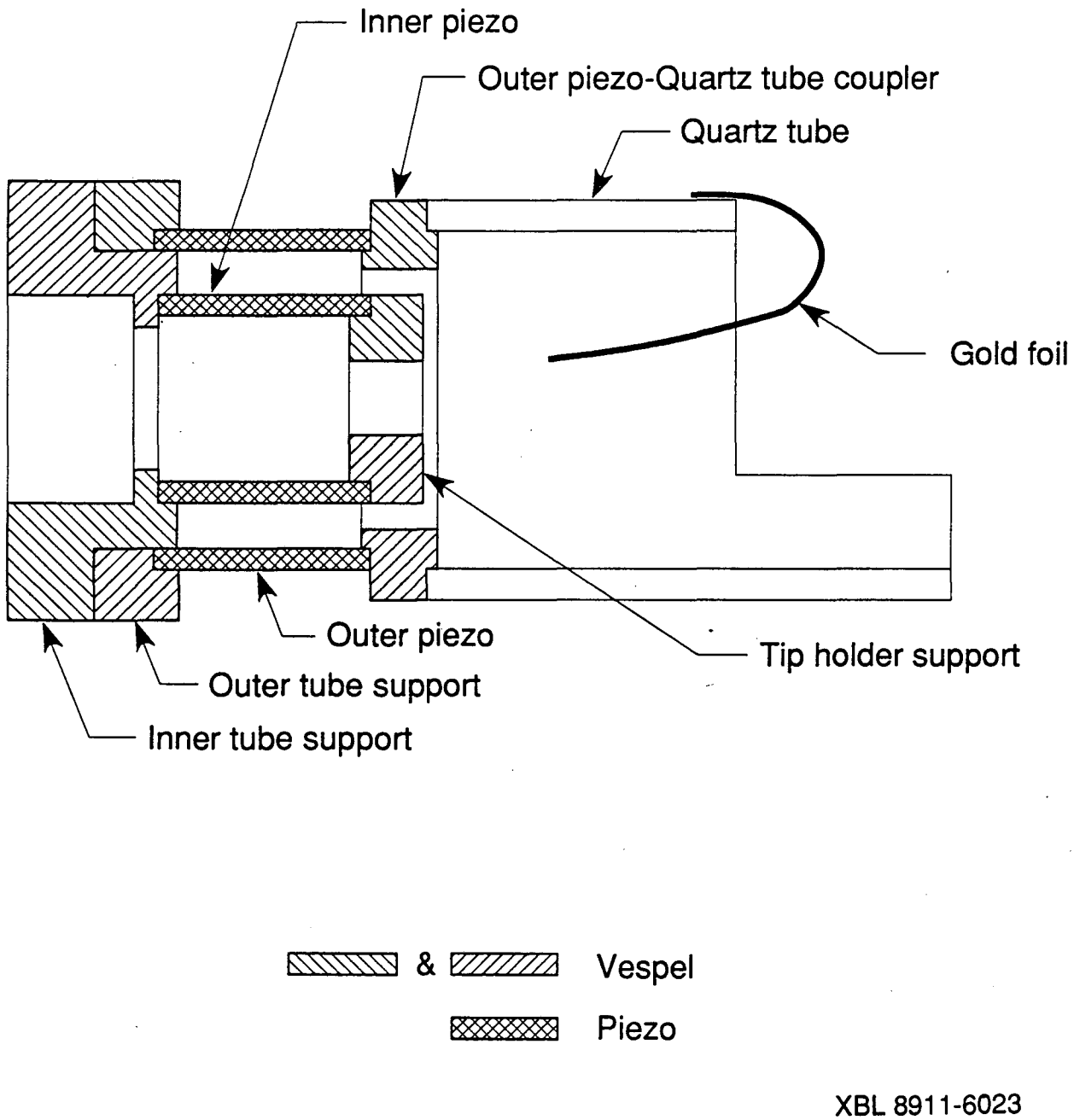

Figure 5.2: (a) Cross-section of the STM head. Tips can be exchanged by inserting a "wobble-stick" (see Fig. 5.4) into the inner piezo from the left side. A sample holder (see Fig. 5.7) rests in the quartz tube, and is provided bias voltage by contact with a hanging gold foil strip.

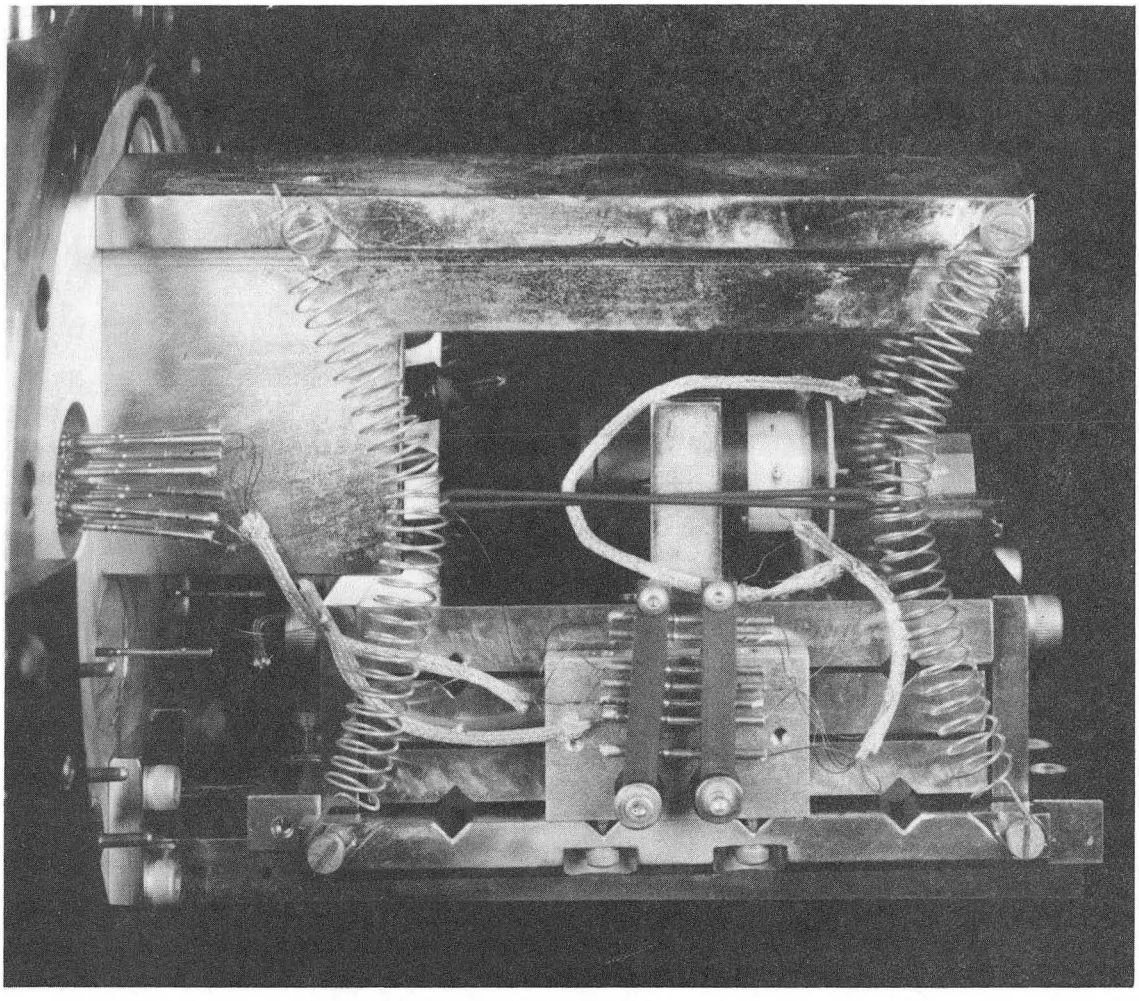

Figure 5.2: (b) Side view photograph of the STM. This closeup shows the STM head mounted on the stainless steel support plate.

BBC 890-10846

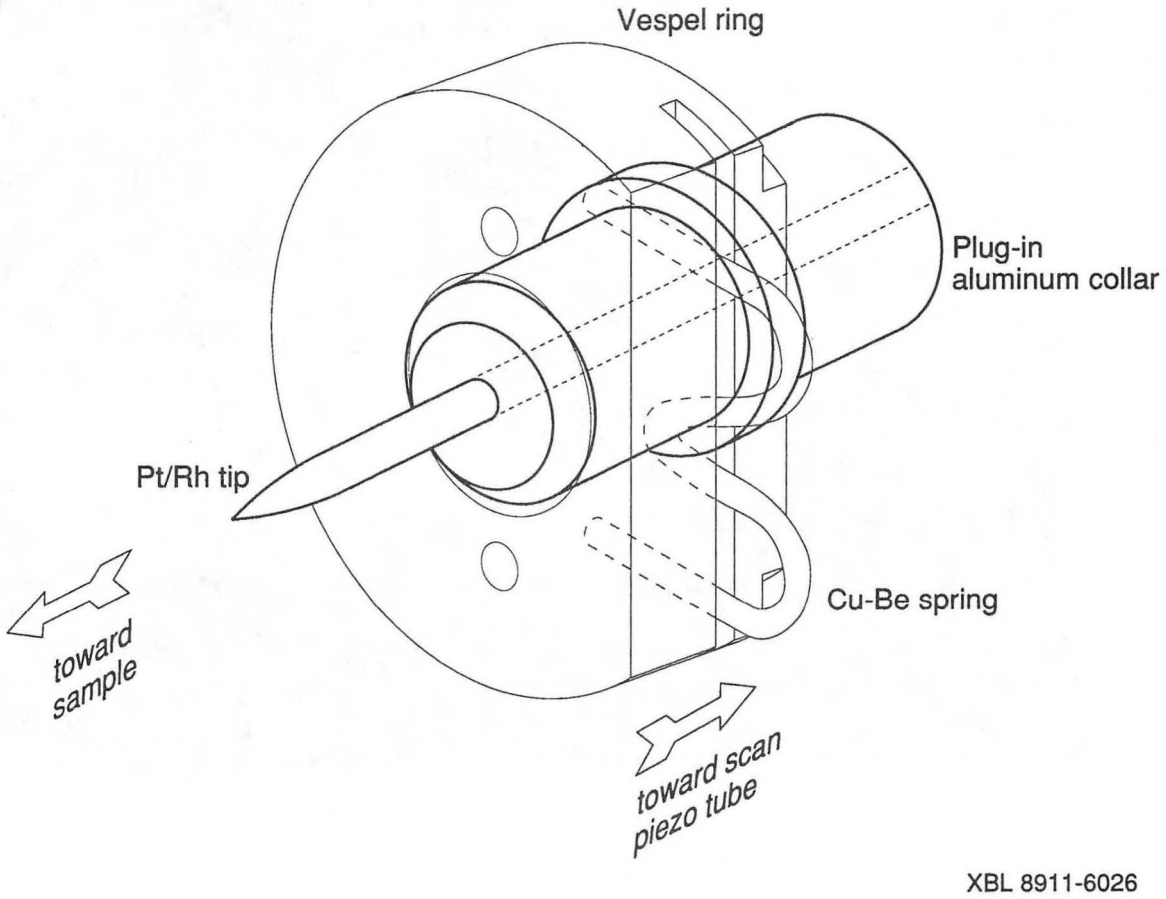

Figure 5.3: Detailed view of the Vespel tip holder, tip retaining Cu-Be spring, and Pt/Rh tip held in an aluminum collar.

cally grounded. Four separate shield braids contain the conductors for the scanning tube, the offset/approach tube, the tip and the sample. Connection to the electrical feedthroughs is made by soldering to each wire a gold-coated, copper contact pin.[34] The connections then allow easy removal of the entire head from the support/vibration isolation system.

Vibration Isolation

Microscope Head The instrument uses three stages of vibration isolation.[35] Two stages are used for the in-vacuum instrument assembly (Fig. 5.4). The STM head is mounted to a stainless steel baseplate which rests on three layers of alternating silicone cord[36] and stainless steel plate. The bottom plate is suspended from a stainless steel cantilever by Cu-Be springs.[37] Viton o-rings, connecting the springs on each side of the microscope, are used to increase the effective spring length, and to provide high frequency damping. The cantilever is fastened to an eight inch conflat flange. The combination of stacked plates and metal springs filters out high frequency vibrations and reduces the amplitude of low frequency mechanical vibrations transmitted through the flange.

Ultra-High Vacuum Chamber The STM is mounted in a standard stainless steel Varian bell jar attached to a Multi-VacIon pumping well by a 12 inch Wheeler flange (Fig. 5.5). The background pressure after a 16 hour bakeout at 100 °C is typically 5.0×10^{-10} torr. The third isolation stage uses three air table legs[38] to raise the entire chamber from the floor. The three isolation stages function well together, allowing imaging of lateral features one to two angstroms apart and corrugations less than 0.1 Å. In this system, the lowest resonance detected in the tunneling current occurs at 3 Hz. The effectiveness of the isolation system is represented by Figure 5.6.

[34] These are 17 Series pins used in Amphenol D-shell electronic connectors.

[35] M. Okano, K. Kajimura, S. Wakiyama, F. Sakai, W. Mizutani, and M. Ono, *Journal of Vacuum Science and Technology A*, vol. 5, p. 3313, 1987.

[36] Parker Seal Group, Lexington, KY. Part 2-395 S604-70, $\frac{3}{16}$ inch cross section.

[37] The springs are wound on a mandrel chucked into a lathe. Spring parameters are: $\frac{1}{32}$ inch wire diameter, 0.302 inch diameter mandrel, 30 turns. The springs are encapsulated in a helium atmosphere (460 torr) then tempered for 1 hour at 300 °C.

[38] Newport Co., Fountain Valley, CA. Model XJ-A.

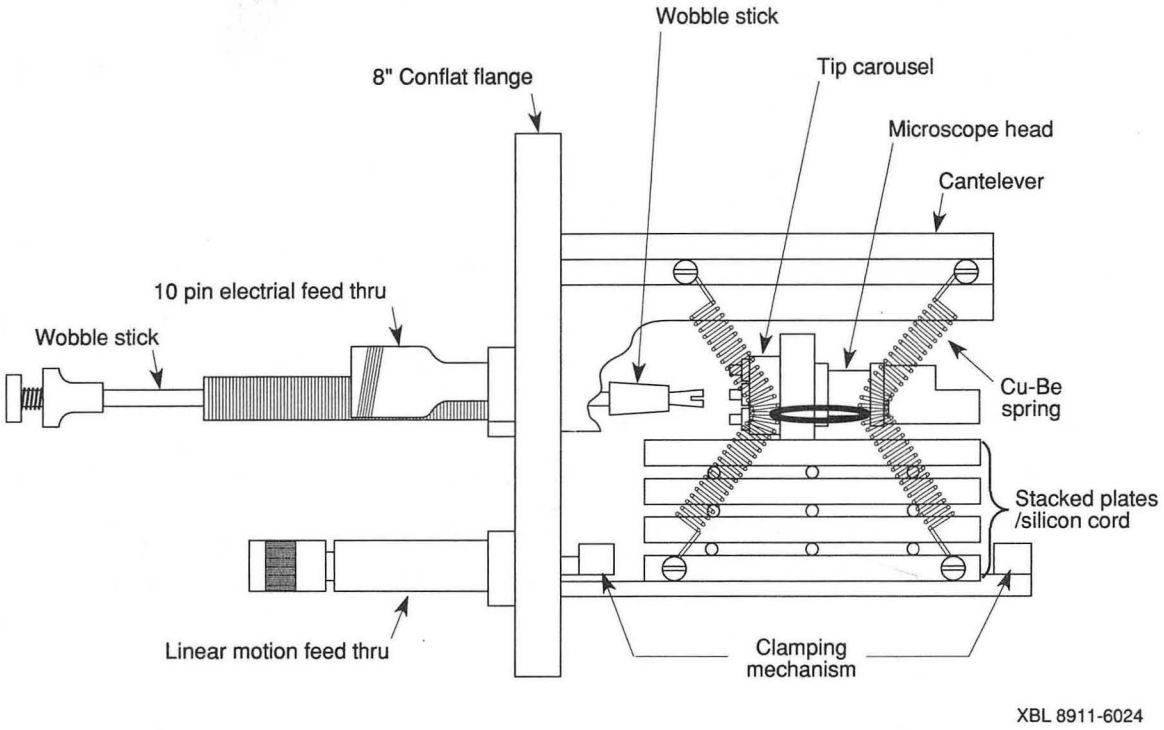

Figure 5.4: (a) Schematic of the STM head and its support structure mounted to an eight inch conflat flange. Two vibration isolation stages are shown consisting of Cu-Be springs and a stack of stainless steel plates separated by silicone cord. The wobble-stick transfers tips from the carousel opposite the microscope head. Electrical contact is provided by two ten-pin feedthroughs, and a linear motion feedthrough is used to clamp the microscope baseplate for tip and sample transfers.

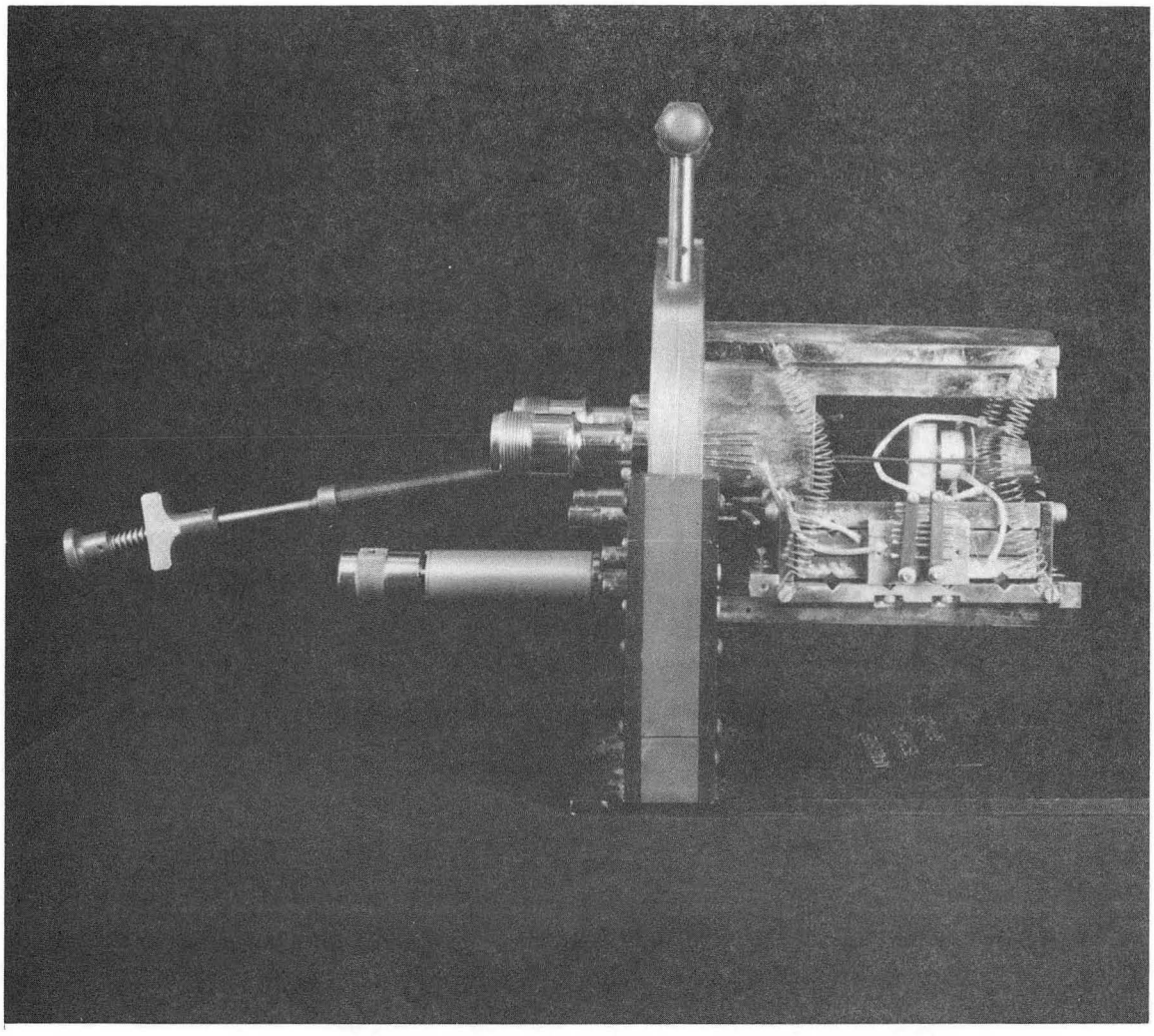

Figure 5.4: (b) Side view photograph of the STM.

BBC 890-10844

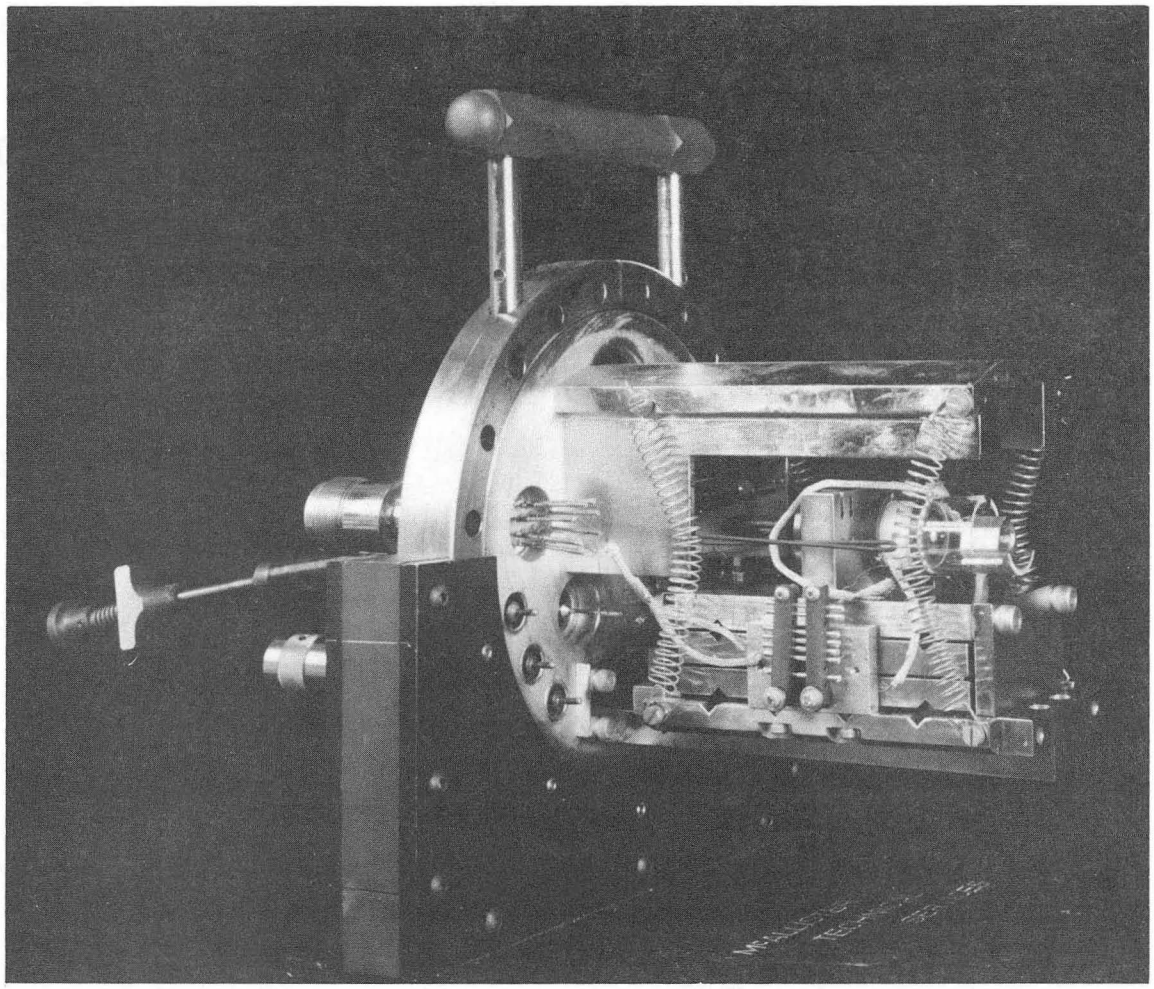

Figure 5.4: (c) Perspective view photograph of the STM.

BBC 890-10842

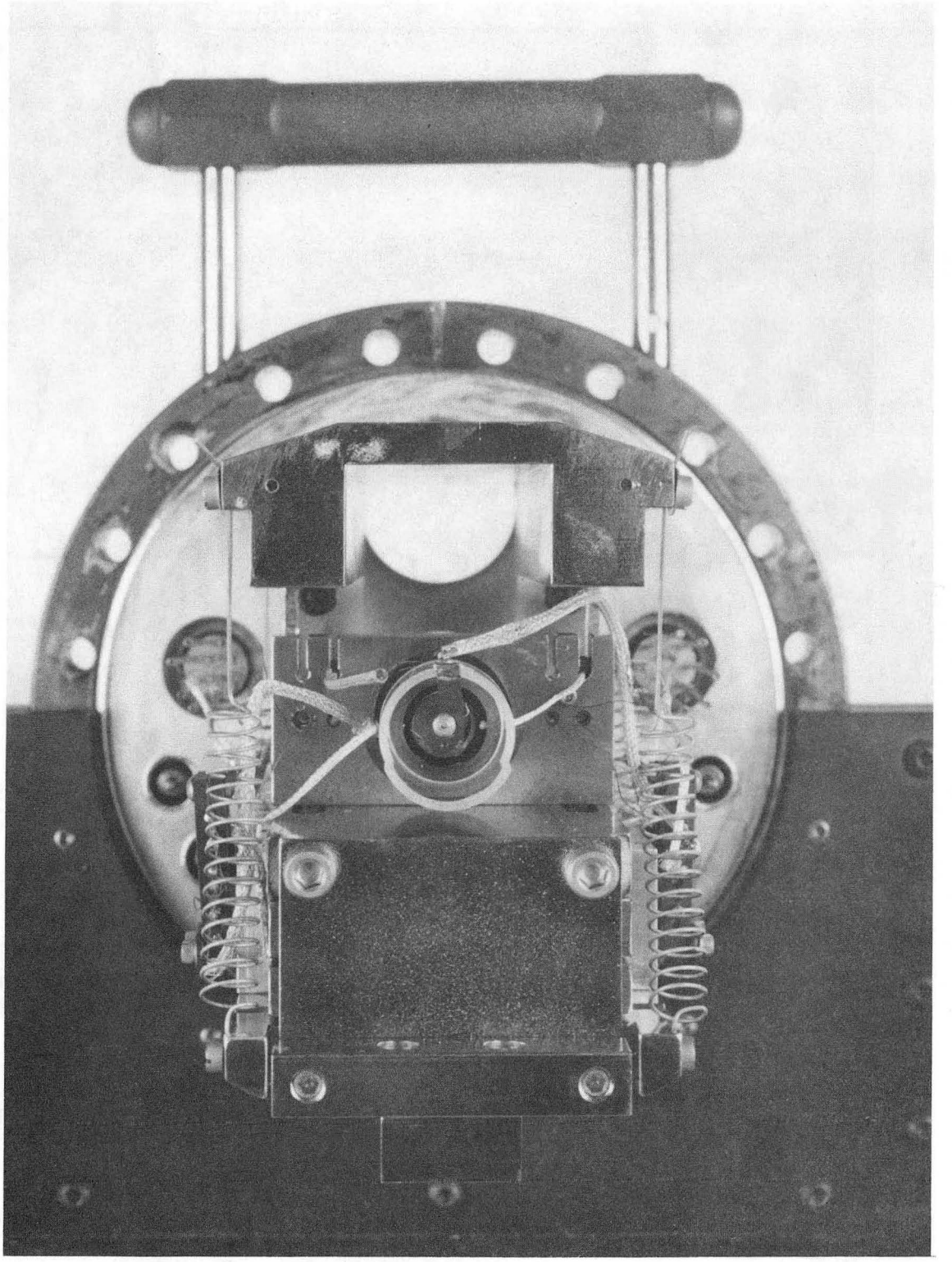

Figure 5.4: (d) Coaxial view photograph from the instrument's vacuum side. Notice the tip, tip collar, and Vespel holder (see Fig. 5.3).

BBC 890-9292

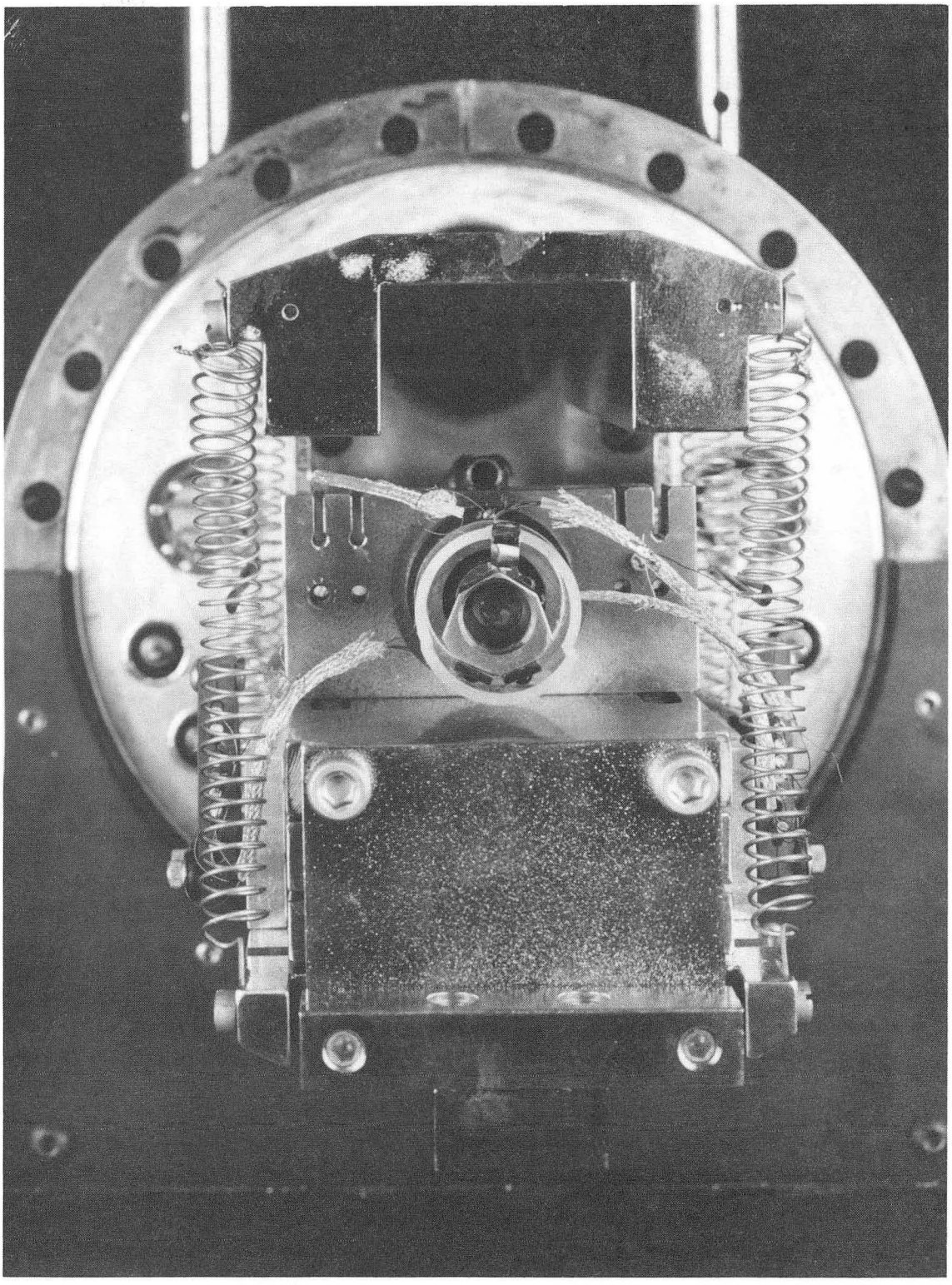

Figure 5.4: (e) Coaxial view photograph from the instrument's vacuum side. The sample holder (see Fig. 5.7) is resting in the quartz tube.

BBC 890-10848

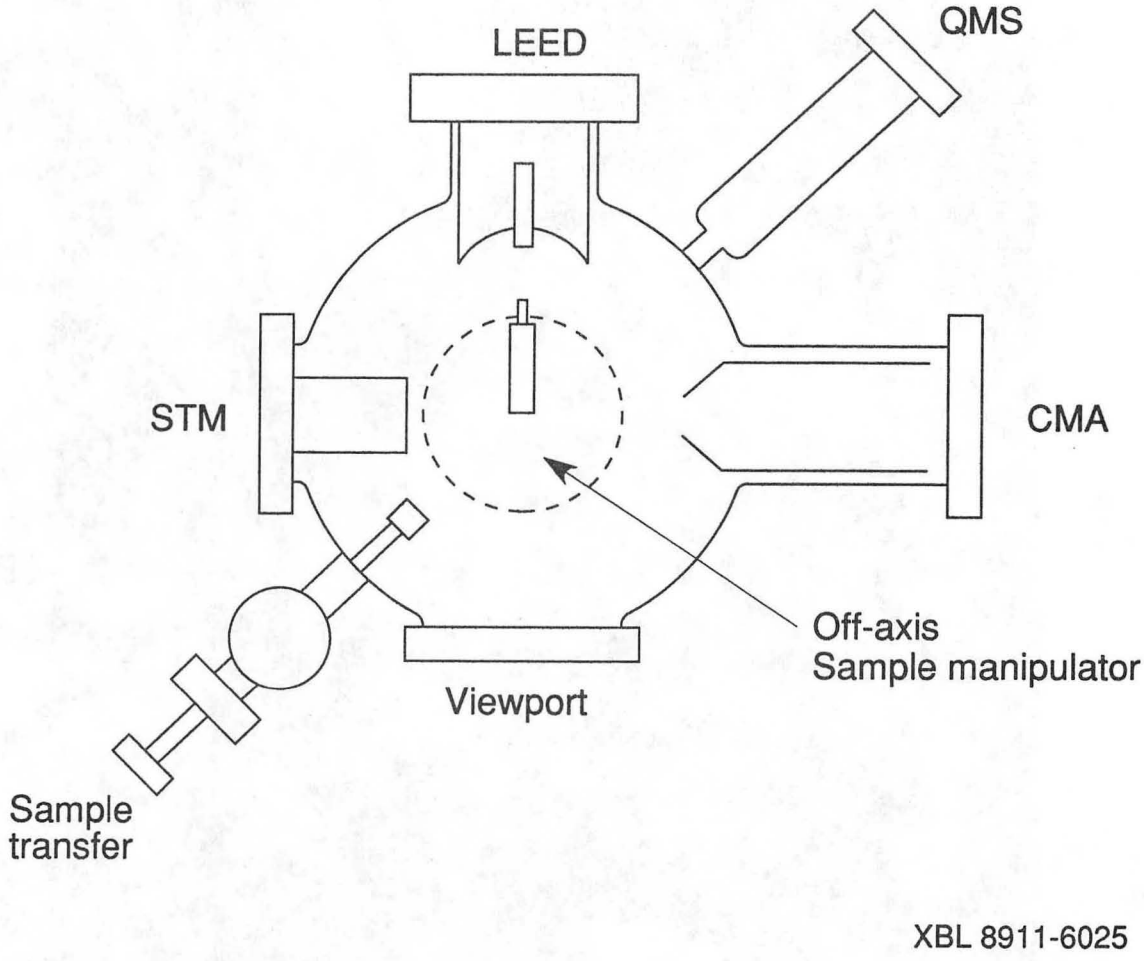

Figure 5.5: (a) Equatorial cross-section of the UHV chamber indicating instrument positions. Sample transfer from air to UHV is accomplished through a $2\frac{3}{4}$ inch flange between the STM and viewport.

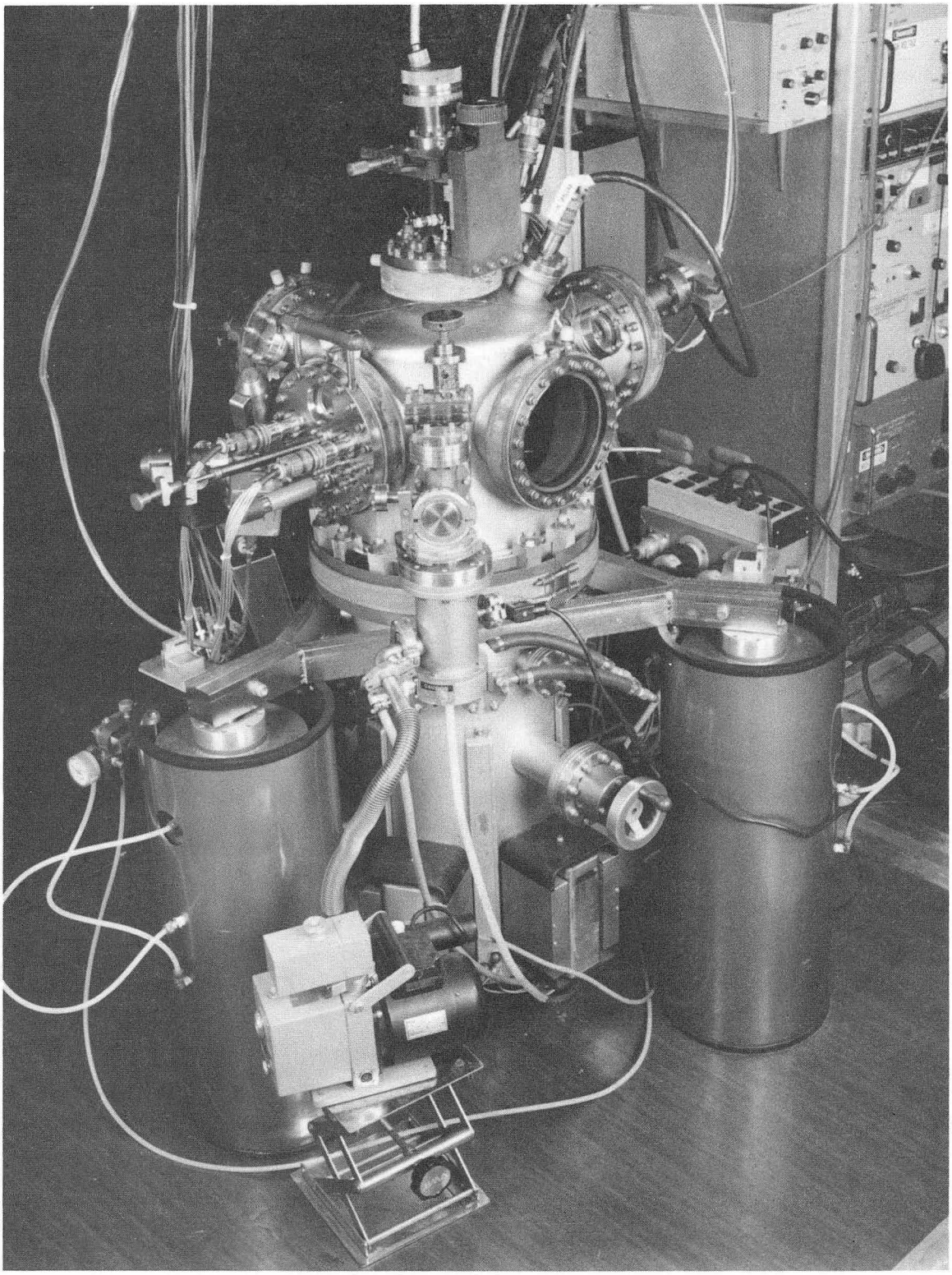

Figure 5.5: (b) Photograph of the chamber along the transfer system axis.

BBC 890-9300

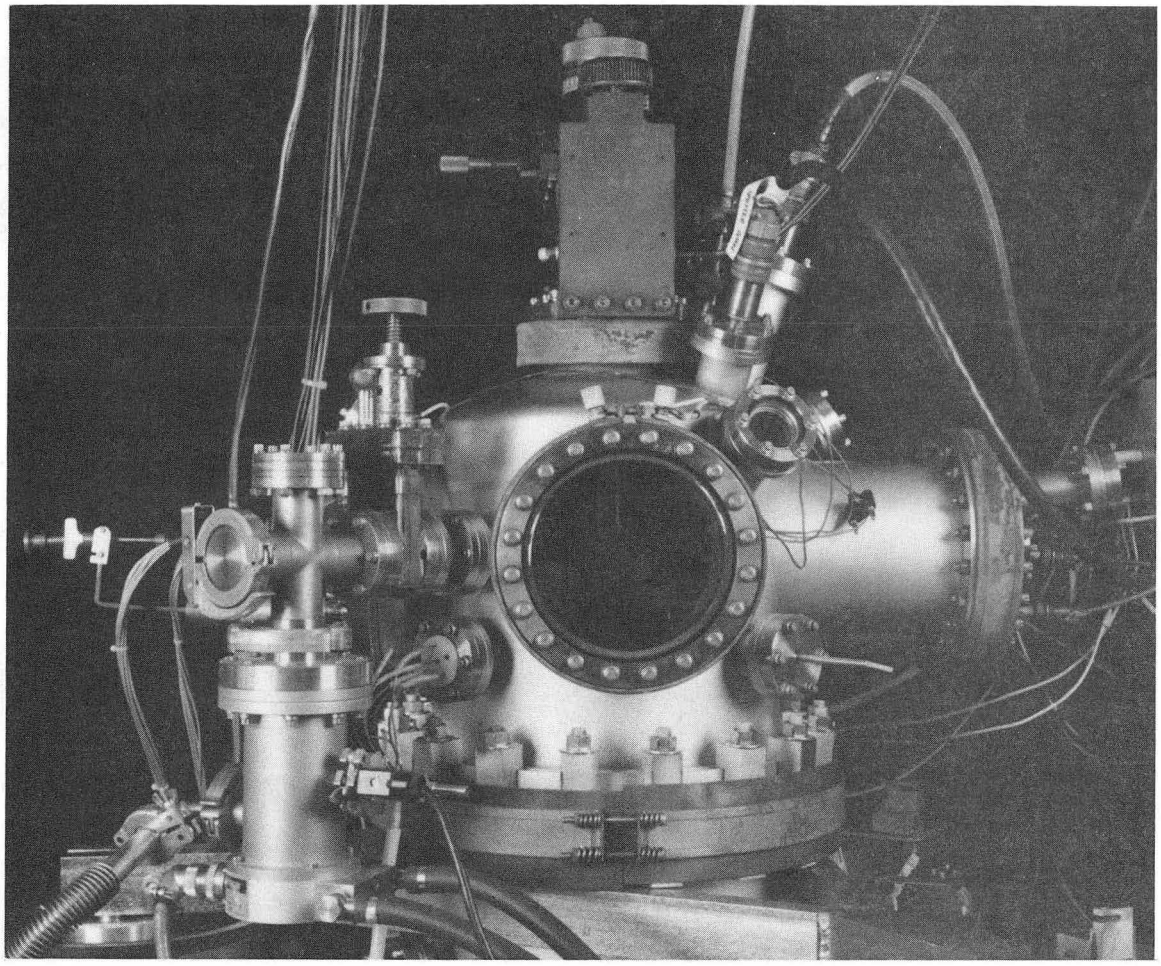

Figure 5.5: (c) Photograph of the upper chamber section along the viewport axis.

BBC 890-9294

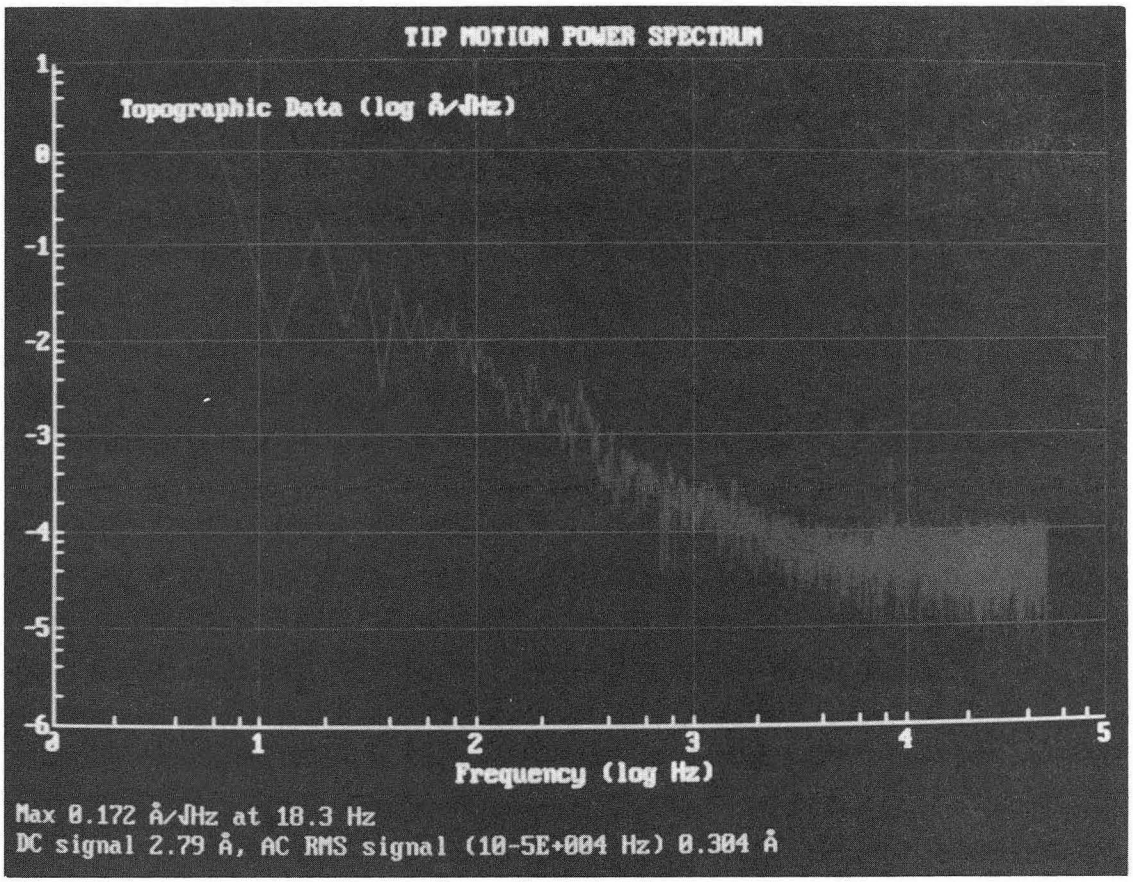

Figure 5.6: Fourier transform of the in-range Z piezo response prior to scanning. The microscope is in UHV, and the sample is the Re(0001)/S-p(2×2) surface. Tunneling parameters are: -0.1 V sample bias, 2 nA current setpoint, and 50 MΩ gap resistance. This measurement indicates an RMS noise level of 0.3 Å over a bandwidth of 50 kHz.

BBC 904-2747

Tips and Tip Transfer

Much effort has been directed towards characterizing, preparing and understanding STM tips.[39–43] Both etched tungsten, and mechanically cut Pt/40% Rh tips have been used. The mechanically cut tips have worked as well as the etched tips, but are easier to prepare. In addition, the platinum/rhodium alloy is extremely resistant to oxidation. The geometry obtained by mechanical cutting provides a sufficiently sharp tip structure. The 0.040 inch diameter tip wire is held by spring tension in an aluminum collar (see Fig. 5.3). The collar fits into the Vespel holder epoxied to the front of the scanning tube.

Tips are tranferred by a "wobble-stick"[44] from a Vespel carousel (see Fig. 5.4). The carousel is secured to the tube support plate opposite the scanning tube. A tip is transferred by removing it from the carousel, and then directing it along the center-line of the concentric piezos. The wobble-stick and tip pass through the carousel, the tube support plate, and the inside of the scanning tube. The collar is then pushed into the Vespel tip holder. The Vespel parts serve to guide the wobble-stick to the tip holder. A clamping mechanism, using a linear motion feedthrough to push the microscope assembly into a positioner, secures the STM during tip transfer.

Sample Holder and Tip-Sample Approach

The sample holder consists of a 0.500 inch diameter tantalum rod to which four 0.125 inch diameter sapphire ball bearings[45] are mechanically attached (Fig. 5.7). Stainless steel has been used previously, but tantalum is found to cool after sample heating roughly three times faster. Also, tantalum is twice as dense as stainless steel. This mass increase seems to improve sample approach/retract performance. Sapphire is used since it is hard, thus resisting damage from repeated sample holder motions. A hole is bored in the rod to accommodate the manipulator. The approach

[39] Y. Kuk and P.J. Silverman, *Applied Physics Letters*, vol. 48, p. 1597, 1986.
[40] B.N.J. Persson and J.E. Demuth, *Solid State Communications*, vol. 57, p. 769, 1986.
[41] H.W. Fink, *IBM Journal of Research and Development*, vol. 30, p. 460, 1986.
[42] T. Hashizume, I. Kamiya, Y. Hasegawa, N. Sano, T. Sakurai, and H.W. Pickering, *Journal of Microscopy*, vol. 152, p. 347, 1988.
[43] V.T. Binh, *Journal of Microscopy*, vol. 152, p. 355, 1988.
[44] McAllister Technical Services, Berkeley, CA.
[45] Industrial Tectonics, Dexter, MI. Part 1451001.

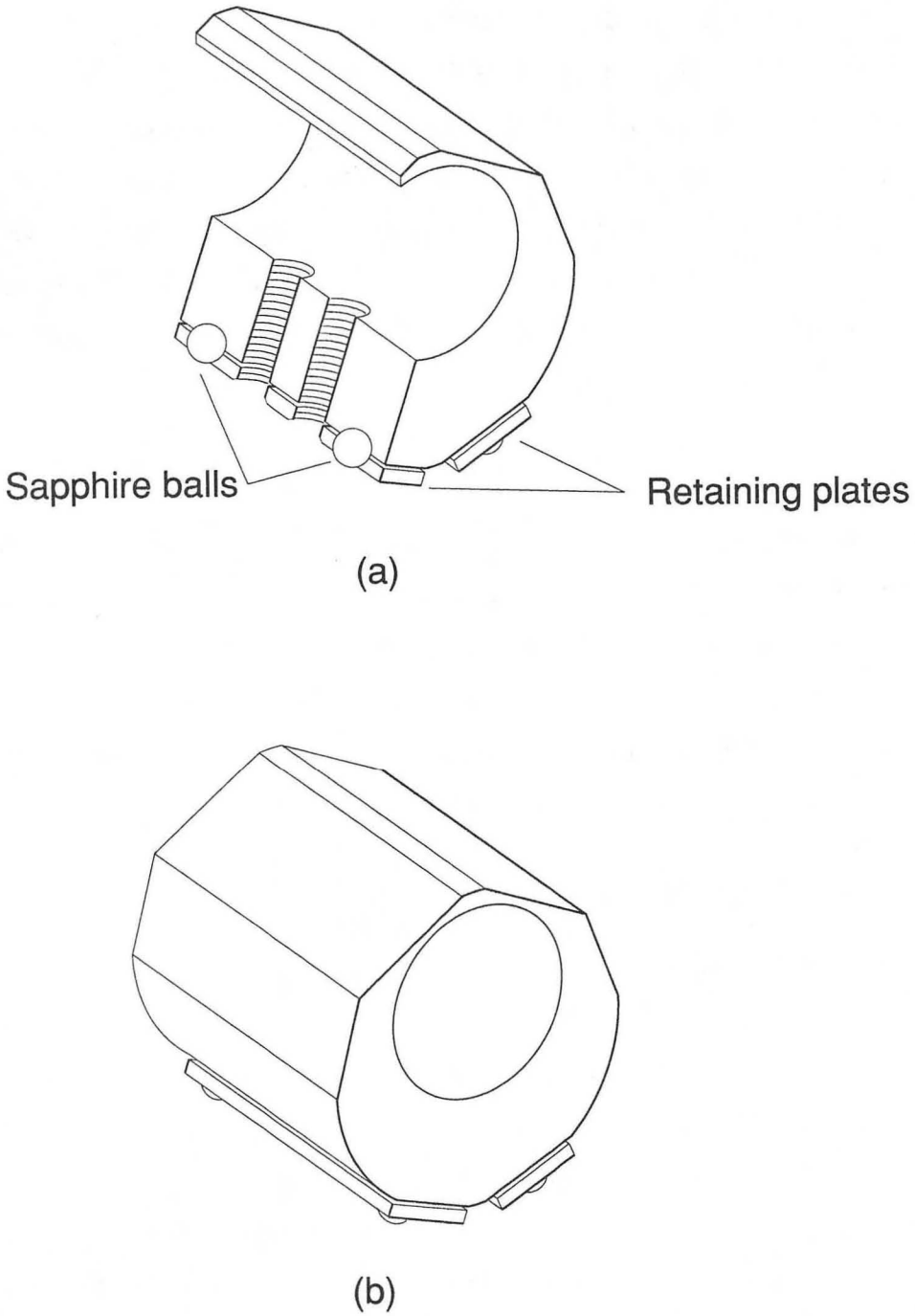

Figure 5.7: (a) Sectional view of the sample holder. The sapphire balls are mechanically fastened to the holder. The balls are secured by two stainless steel retaining plates. (b) Perspective view of the sample holder.

mechanism requires a low center-of-gravity sample holder, so the top is machined flat. To mount a sample, 0.006 inch thick Ta foil is spot welded to one face of the holder. A hole smaller than the sample is punched in the foil for effective heating. The sample is centered over the punched hole. To clamp the sample to the holder, 0.003 inch thick Ta foil strips are spot welded around the sample edges. This method provides secure fastening of the sample by contact pressure instead of spot welding. Direct spot welding to a single crystal can severely damage it. This is apparent from visual examination of a sample subjected to this treatment. The spot welds pit the crystal, and the local heating can warp the metal wafer. The sample holder rests on the quartz tube extending from the outer piezo. Quartz is preferred over other materials since it is transparent, allowing visual assessment of tip-sample approach, and possesses a low thermal expansion coefficient.

A sample is brought into tunneling range via a stick-slip mechanism.[11,46] An approach waveform, as illustrated in Figure 5.8, is applied to the inner electrode of the approach piezo. The outer sectors are held at ground. The digital waveform consists of two parts. A linear ramp extends or contracts the piezo, depending on polarity. A sharp step returns the piezo to its original length. During the first part, the sample holder maintains static friction and retracts from or approaches towards the tip. The second part of the waveform breaks static friction, but the sample holder's inertia allows it to remain stationary while the piezo is in motion. Tunnel current is monitored before each digital increase of the ramp and after each sharp step. Variable parameters are overall ramp height, step size and delay before tunnel current detection. Current sensing cannot be continuous since the voltage change induces current spikes. After a delay that allows the spike to decay, the tunnel current is read and checked against a limit before waveform generation continues. The curvature in the waveform results from the response time of the high voltage power supply. The waveform is repeated until a pre-determined tunnel current is detected by the electronics. Once tunnel current is detected, control is turned over to the offset supply and feedback electronics. With this mechanism, a sample can be brought rapidly (2 mm/min) and

[46] Ch. Renner, Ph. Niedermann, A. D. Kent, Ø. Fisher, *Journal of Vacuum Science and Technology A*, vol. 8, p. 330, 1990.

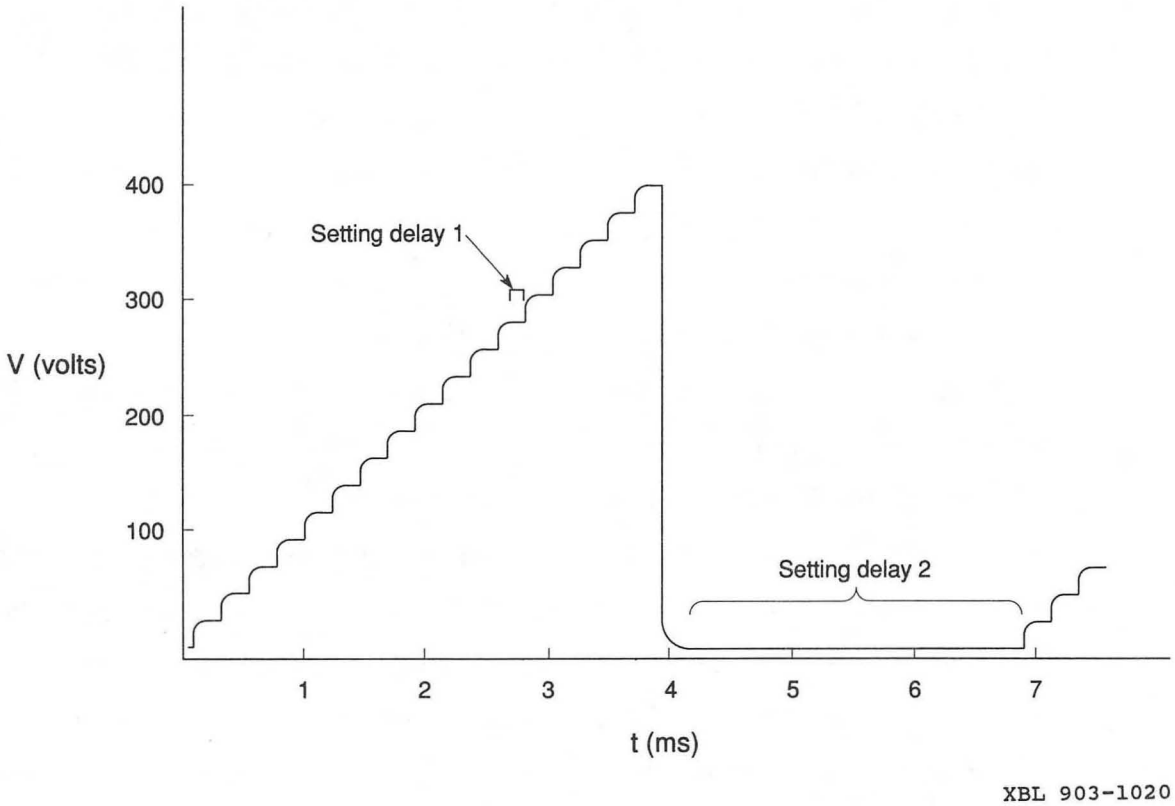

Figure 5.8: The approach/retract voltage waveform is digitally generated, and is basically a sawtooth. The ramp contracts (for sample approach) or expands (for sample retract) the outer piezo tube.

reliably into tunneling range without mechanical linkages, and is easily transferrable to the sample manipulator for other surface studies.

Sample Manipulator

The sample manipulator is a modified Varian Model 981-2523 providing X-Y-Z translation, 360° rotation, and sample tilt capability. A 90° arm assembly was designed to fit the rotary motion feedthrough, and is pictured in Figure 5.9. To reach 2000 °C typical heating parameters are 40 mA emission current and -2000 V filament bias. The filament is wound from 0.020 inch diameter tungsten wire, and is isolated from the stainless steel assembly by an alumina "two-bore" tube. The sample holder is held in contact with the nozzle by a spring-loaded lever to prevent accidental detachment during transfer motions. The manipulator linear motion feedthrough is used to depress the lever allowing release of the sample holder. Electrical contact for the filament and ground are provided through the manipulator flange. An optical pyrometer is used to measure sample temperature, while a thermocouple spot-welded to the sample clamp monitors sample holder temperature.

Since the tantalum sample holder is in contact with the stainless steel manipulator arm, cooling in vacuum occurs very slowly. The microscope is sensitive to thermal drift, therefore large temperature gradients between sample and tip make imaging difficult at low scan rates. Quick cooling of the sample to minimize surface contamination, and to prevent large thermal drift is necessary. After heating, the sample holder is put in contact with a liquid nitrogen cooled copper block (see Fig. 5.9). The block is V-shaped, and the cylindrical sample holder makes line contact in the "V". Cooling from 2000 °C to ambient temperature is done in about twenty minutes.

Sample Transfer

Samples can be introduced into the vacuum chamber from air through a turbopumped[47] airlock (Figs. 5.5 and 5.10). A fixture that accepts the sample holder is mounted to a 32 μin surface finish stainless steel rod. A teflon thrust ring applies pressure to a Viton piston seal[48] contacting the rod. The rod can then be extended and retracted

[47] Pfeiffer Balzers, Hudson, NH. Model TPU050. 50 l/s.
[48] Parker Seal Group, Salt Lake City, UT. Part 8504-0050 4180.

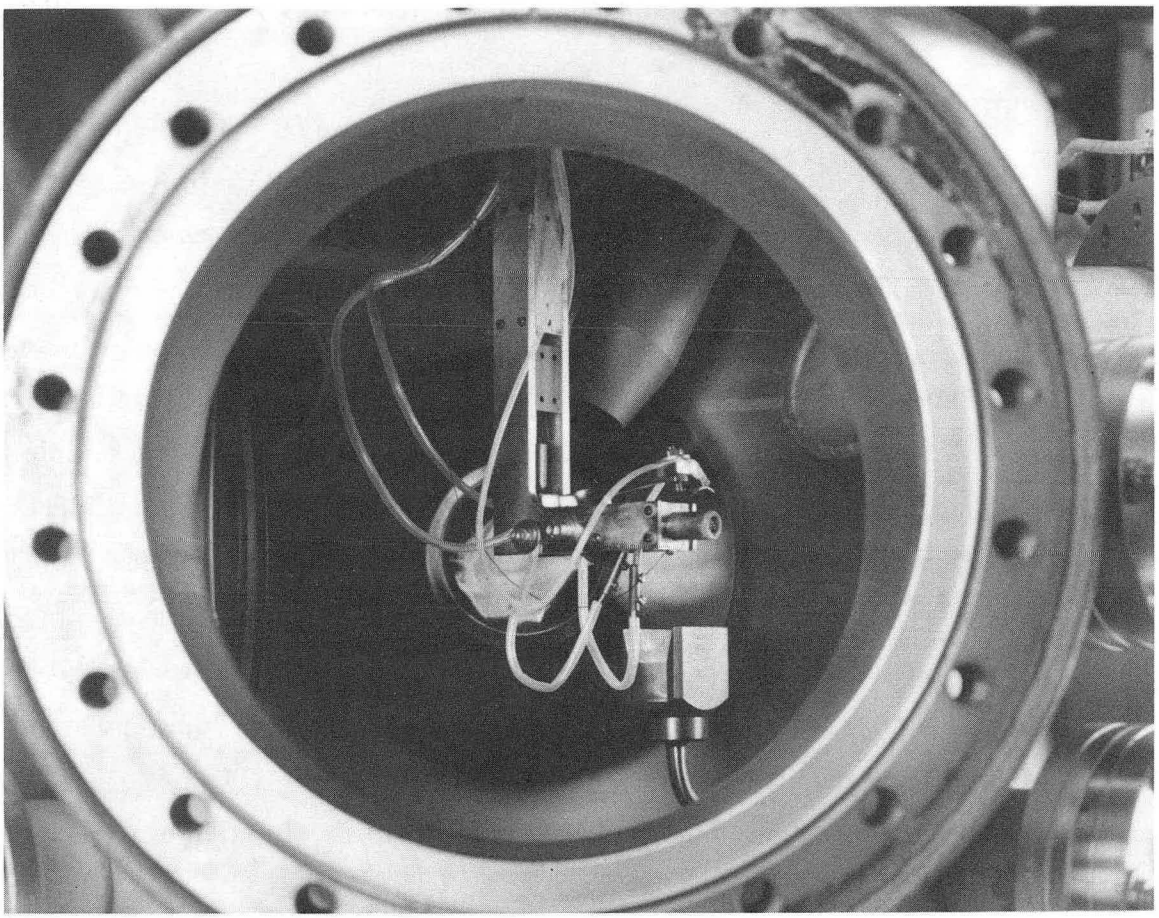

Figure 5.9: A photograph of the manipulator arm through the STM flange. Visible are the electron bombardment heater filament, and sample clamping lever. The copper V-block used for sample holder cooling is also visible at lower right. The nozzle protruding from the arm supports the sample holder through its bored hole. For sample heating, an electron bombardment heating filament exists in the nozzle, and is controlled by an emission regulated power supply.

BBC 890-9296

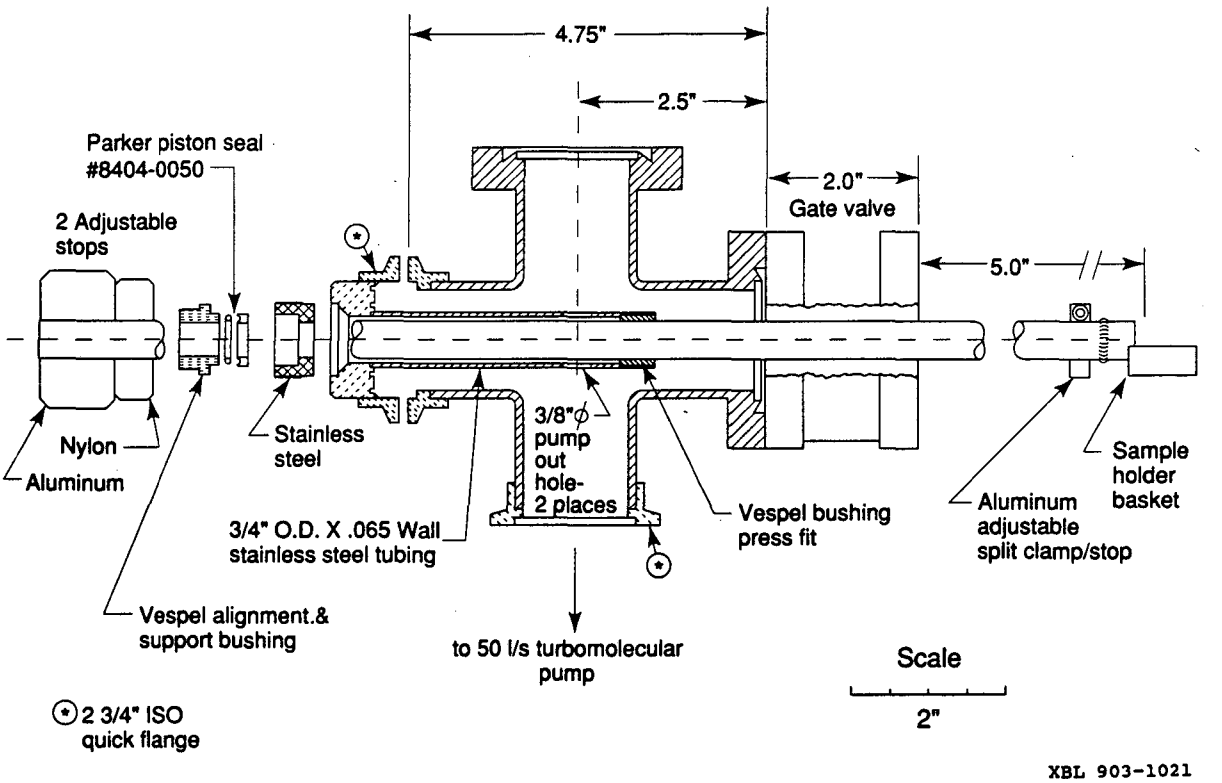

Figure 5.10: Assembly drawing of the sample transfer system. The right flange of the gate valve is mounted to the UHV chamber. The sample holder rests in the basket shown at the end of the transfer rod.

through a gate valve without significant vacuum loss. The rod is extended into the chamber, then the sample manipulator accepts the sample holder from the fixture. If the vacuum chamber is at a base pressure of 10^{-10} torr, the pressure will rise to 10^{-8} torr during sample transfer. Base pressure is easily recovered upon closing the gate valve, and the process takes approximately fifteen minutes, including evacuation of the airlock.

5.4 Electronics and Software

The STM electronics have been designed and built in collaboration with the Electronics Engineering Division of the Lawrence Berkeley Laboratory. To minimize input capacitance, bias is applied to the sample holder, and the tip is connected to an external current-voltage preamp[49] held at virtual ground. The pre-amp circuit bandwidth is 50 kHz and provides a first stage gain of 10^6 V/A. An integral clock-driven digital ramp generator produces X-Y scan waveforms. All piezos are driven by high voltage op-amps.[50] An analog proportional/integrator feedback loop controls the tip/sample separation. The electronic noise measured with the sample out of range is 0.2 pA/$\sqrt{\text{Hz}}$ for this configuration. Current and topographic data is collected by a 12-bit analog/digital I/O card[51] residing in an IBM-PC compatible 80386/7 computer. Data can be aquired at a maximum scan rate of 250 Hz, but typical operating parameters are: 1-4 Hz (topographic mode) and 60 Hz (current mode). The data is displayed by an enhanced VGA card[52] (640×480 pixels, 256 colors) on a color monitor. The software[53] has been written in the laboratory, and allows real time data analysis and display. The integration of this instrument with traditional surface science techniques to perform studies of overlayer/metal substrate systems in real space

[49] Burr-Brown OPA128LM.
[50] Scan tube: Apex PA83, ±130 V. Approach/offset tube: Apex PA88, ±220 V.
[51] Data Translation, Marlboro, MA. Model DT2821-F.
[52] Orchid Technology, Fremont, CA. Prodesigner Plus VGA for AT bus.
[53] Software is written and supported by D. Frank Ogletree. This package, and the electronics are available commercially through RHK Technology, Rochester Hills, MI.

has produced atomic resolution images of those surfaces. These studies are discussed in Part IV.

Chapter 6

Auger Electron Spectroscopy and Low Energy Electron Diffraction

6.1 Introduction

AES and LEED, as they have been used in this work, are presented briefly. Both techniques can provide a large amount of information on surface systems. These studies did not require, though, the full exploitation of the techniques' capabilities. Emphasis, in this chapter, is on a description of the instrumentation used for the UHV studies, and on which aspects of the techniques were used to assist the STM studies. Several authors have provided extensive reviews of AES[1,2] and LEED[3,4] that can be consulted if further details are desired.

6.2 Auger Electron Spectroscopy

AES makes use of the phenomenon in which electrons undergoing a radiationless transition after excitation by a photon or another electron are emitted from a solid surface. A core electron is ionized by the incoming radiation. The core vacancy is then filled by a valence electron. The available energy is released as an X-ray photon or transferred to another valence electron which escapes the solid with a characteristic kinetic energy. For optimum creation of an Auger electron, the exciting particle or

[1] G. Ertl and J. Küppers, *Low Energy Electrons and Surface Chemistry*, Verlag Chemie, 1974.

[2] C. L. Briant and R. P. Messmer, *Auger Electron Spectroscopy*, Academic Press, Inc., 1988.

[3] L. J. Clarke, *Surface Crystallography: An Introduction to Low Energy Electron Diffraction*, John Wiley & Sons, Inc., 1985.

[4] M. A. Van Hove, *Low Energy Electron Diffraction: Experiment, Theory and Surface Structure Determination*, Springer-Verlag, 1986.

photon should have an energy of ~3 keV. If the energy is less than this value, the primary process will not ionize the sample. If the energy is much greater than this value, appreciable interaction with the sample cannot occur. Since Auger emission is a three electron process, hydrogen and helium are not detectable by this technique. Auger electrons have energies roughly three times less than the primary radiation. This low energy and correspondingly small escape depth determine the detected sample volume. Therefore, AES provides chemical information on the surface layer of a sample, and is sensitive to concentrations as low as one percent of a monolayer. While STM is microscopic, AES is not, and can only provide information on the average conditions of the surface. The resolution limits for AES are related to the electron beam spot size and beam current. Typically, 1 μm lateral resolution is easily obtainable from commercial systems.

The AES experiment was performed using a glancing incidence electron gun and a CMA[5] for energy analysis. The CMA acts as a band pass filter for analyzing electron energies, and significantly improves the signal-to-noise ratio over that obtained through the use of high pass detection methods. The AES data was used to provide a measure of surface cleanliness before overlayer adsorption. After overlayer preparation, it provided a quantitative measure of adsorbate concentration. Although a calibration was not performed, peak height ratios compared to previous studies provided sufficient information. The AES results are presented in the final chapters.

6.3 Low Energy Electron Diffraction

The diffraction of low energy electrons was first observed by Davisson and Germer.[6] They found angular dependent maxima in the distribution of backscattered electrons from a polycrystalline Ni sample which had undergone repeated annealing. The effect is based on the wave properties of matter, and is represented by de Broglie's equation, $\lambda = \frac{h}{mv}$. This states that a flux of particles with velocity v and mass m will possess a wavelength λ. This wave nature suggests interference will occur from interactions between the particles and periodic lattices. Since low electron energies are used (10 to

[5] P. W. Palmberg, G. K. Bohn and J. C. Tracy, *Applied Physics Letters*, vol. 15, p. 254, 1969.
[6] C. J. Davisson and L. H. Germer, *Physical Review*, vol. 30, p. 705, 1927.

500 eV), LEED, like AES, samples only the first few atomic layers of a solid.

The LEED diffraction pattern displays the surface lattice geometrical structure. From analysis of diffraction spot intensities as a function of incident beam voltage (I-V curves), information on the surface unit cell can be gained. Typical commercial LEED instrumentation permits periodic features on the order of 50–100 Å to be studied. Unfortunately, since the diffraction pattern represents a two-dimensional reciprocal space lattice, and is the result of multiple scattering effects, it can be difficult to model this process. Since LEED theory[4] has been under development for approximately 25 years, sophisticated methods which lead to real space solutions of surface structures exist. LEED results provide an accurate (± 0.1 Å) measure of surface bond distances. For gaining information on the actual surface, inherent difficulties remain since LEED is not microscopic, and is a reciprocal space technique. New methods have enabled surfaces without long-range order to be examined by LEED,[7,8] and have relaxed the constraint that periodic structures are necessary for diffraction studies. Therefore, using LEED with STM can be very effective for obtaining information on surface chemical bonds.

Most LEED instrumentation, from a design standpoint, is fairly simple. The apparatus used in these studies consists of an incident electron gun, and a hemispherical grid arrangement. The grid furthest from the sample is coated with phosphor to enable visual indentification of diffraction spots. The LEED experiments performed in this work provided a measure of the long range surface order. LEED was used before and, on occasion, after an STM experiment for identification of the surface structure and to ensure the surface structure was intact after lengthy STM imaging sessions. The LEED patterns are shown and discussed in the remaining chapters.

[7]G. S. Blackman, M.-L. Xu, D. F. Ogletree, M. A. Van Hove, and G. A. Somorjai, *Physical Review Letters*, vol. 61, p. 2352, 1988.

[8]R. Q. Hwang, A. Wander, G. S. Blackman, M.-L. Xu, P. de Andres, M. A. Van Hove, and G. A. Somorjai, Department of Chemistry, University of California, Berkeley, and Materials and Chemical Sciences Division, Lawrence Berkeley Laboratory, Berkeley, CA, to be published.

Part IV

Scanning Tunneling Microscopy Studies in Ultra-High Vacuum: Experimental Results

Chapter 7

Incommensurate Graphite on the Pt(111) Surface

7.1 Introduction

Carbonaceous layers are commonly found on metal surfaces in catalytic reactions, and are known to play an important role in lubrication.[1] Carbon is adsorbed in three basic forms: as part of a chemisorbed molecule, as carbidic or sp^3-like carbon, or as graphitic or sp^2-like carbon. Figure 7.1 depicts the formation of a graphitic layer on the Pt(111) surface as the end product of a catalytic thermal dehydrogenation reaction.[2–4]

Incommensurate graphitic carbon layers are known to form on several metal surfaces.[5–9] An incommensurate overlayer is formed when the adsorbed species occupies many different substrate binding sites. Some coincidence lattice usually exists, but long-range order is not common since the overlayer and substrate lattice mismatch produces several rotational and/or spatial domains.

A study using LEED and AES has been previously done for the Pt(111)/C(gr)

[1] G. A. Somorjai, *Chemistry in Two Dimensions: Surfaces*, Cornell University Press, p. 399, 1981.
[2] M. Salmeron and G. A. Somorjai, *Journal of Physical Chemistry*, vol. 86, p. 341, 1982.
[3] L. L. Kesmodel, L. H. Dubois, and G. A. Somorjai, *Chemical Physics Letters*, vol. 56, p. 267, 1978.
[4] B. E. Bent, C. M. Mate, J. E. Crowell, B. E. Koel, and G. A. Somorjai, *Journal of Physical Chemistry*, vol. 91, p. 1493, 1987.
[5] K. Baron, D. W. Blakeley, and G. A. Somorjai, *Surface Science*, vol. 41, p. 45, 1974.
[6] J. L. Gland and G. A. Somorjai, *Surface Science*, vol. 41, p. 387, 1974.
[7] B. Lang, *Surface Science*, vol. 53, p. 317, 1975.
[8] J. G. McCarty and R. J. Madix, *Journal of Catalysis*, vol. 38, p. 402, 1975.
[9] D. G. Castner, B. A. Sexton, and G. A. Somorjai, *Surface Science*, vol. 71, p. 519, 1978.

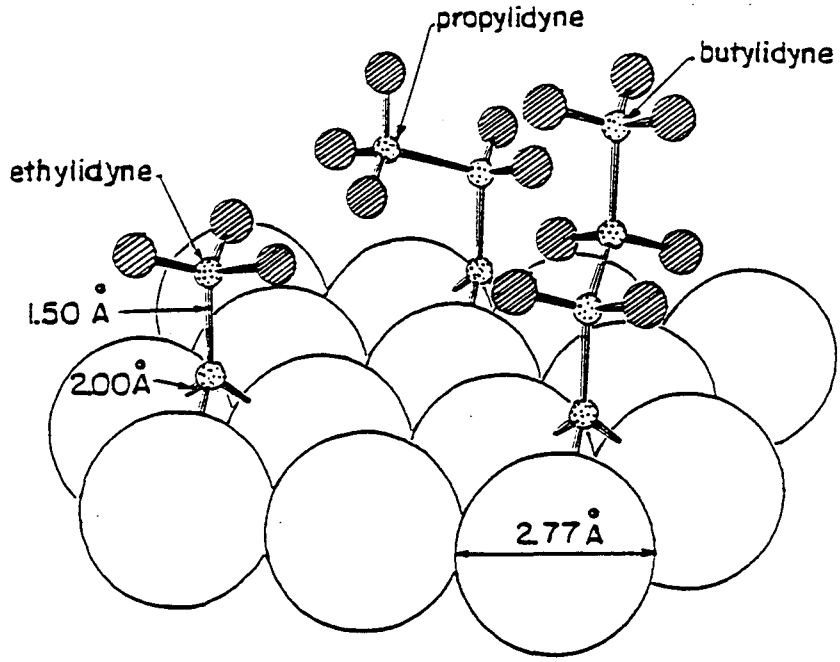

Pt(111) + ethylidyne, propylidyne and butylidyne

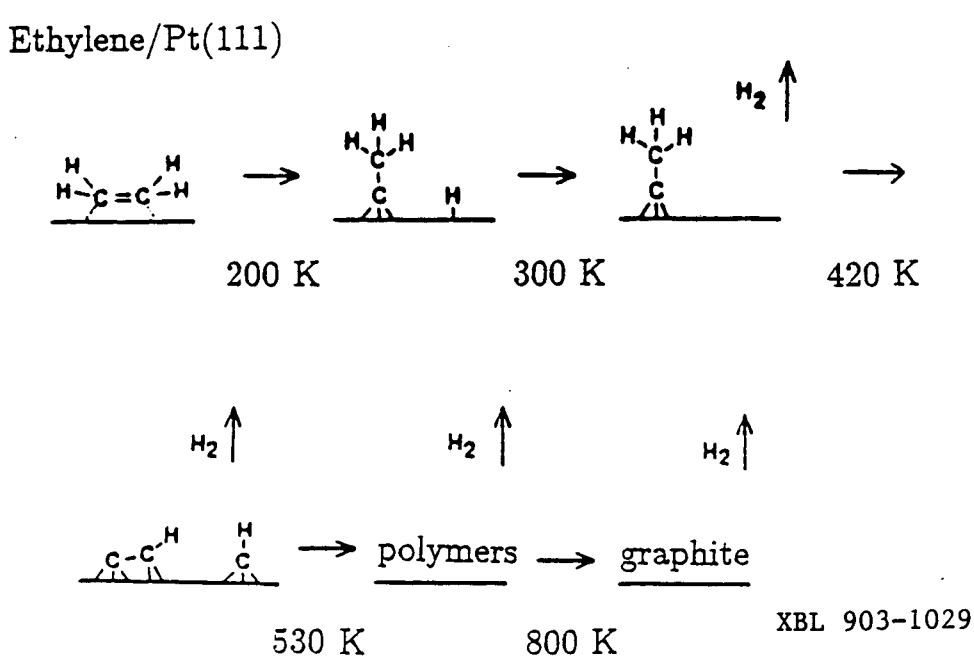

Figure 7.1: Model for the catalytic thermal dehydrogenation of an adsorbed organic molecule (in this case, ethylene). The alkylidyne species (upper schematic) formed when alkenes are adsorbed at room temperature sit in three-fold hollow sites with the carbon-carbon axis perpendicular to the surface. The final reaction product is a graphitic overlayer. (Figure courtesy of B. E. Bent and M. B. Salmeron.)

system.[10,11] The graphite-metal bond distance was measured as 3.70 ± 0.05 Å, which is larger than expected from a "hard-sphere" carbon-platinum bond distance of 2.95 Å. The model proposed to explain the large overlayer-substrate spacing suggests that carbidic carbon is intercalated between the graphite and substrate layers (Fig. 7.2). The carbidic carbon is assumed to sit in three-fold platinum sites at a C-Pt bond distance of 1.25 Å. The graphitic layer would then bond 2.45 Å above the carbidic intercalate.

Graphite is an important surface for STM since it is often used as a calibration standard, and it can provide atomic resolution images in air. Bulk graphite consists of hexagonal sp^2 carbon rings with two atoms per unit cell. The layers are weakly bound to each other allowing easy cleavage of graphite crystals. This material's bulk electronic structure, [12] and intercalation properties[13] have been widely studied. Some surface results have been obtained on bulk graphite,[14] but graphite layers supported on metal substrates have not been widely studied. Theoretical calculations[15,16] have indicated that the corrugation differences observed in graphite images are due to the small interaction between the first and second layers. This interaction serves to modify the charge density distribution at the site with a neighboring second layer atom (A site) relative to the adjacent atom without the second layer neighbor (B site) (Fig. 7.3). *Ab initio* calculations[16] have shown the second layer interaction at the A site creates a dispersive band with a 1.2 eV splitting around E_F (Fermi level energy). The lack of interaction at the B site gives rise to a doubly degenerate band at E_F. The band structure appears in STM images as corrugation asymmetry for sites A and B at all bias voltages. A sites appear lower in height relative to B sites. The center of each surface hexagon extends to the second layer and is imaged as a deep hole (C site). At low bias voltage ($\leq \pm 0.2$ V) the asymmetry is more pronounced. The calculations

[10] D. F. Ogletree, *Ph.D. Thesis*, University of California, Berkeley, p. 508, 1986.

[11] H. Zi-pu, D. F. Ogletree, M. A. Van Hove, and G. A. Somorjai, *Surface Science*, vol. 180, p. 433, 1987.

[12] R. C. Tatar and S. Rabii, *Physical Review B*, vol. 25, p. 4126, 1985.

[13] I. P. Batra and L. Samuelson, *Synthesis Metals*, vol. 1, p. 223, 1979/80.

[14] H. Ohtani, C.-T. Kao, M. A. Van Hove, and G. A. Somorjai, *Progress in Surface Science*, vol. 23, p. 155, 1986 provide tabulation of these results and author references.

[15] I. P. Batra, N. Garcia, H. Rohrer, H. Salemink, E. Stoll, and S. Ciraci, *Surface Science*, vol. 181, p. 126, 1987.

[16] D. Tomanek, S. G. Louie, H. J. Mamin, D. W. Abraham, R. E. Thomson, E. Gantz, and J. Clarke, *Physical Review B*, vol. 35, p. 7790, 1987.

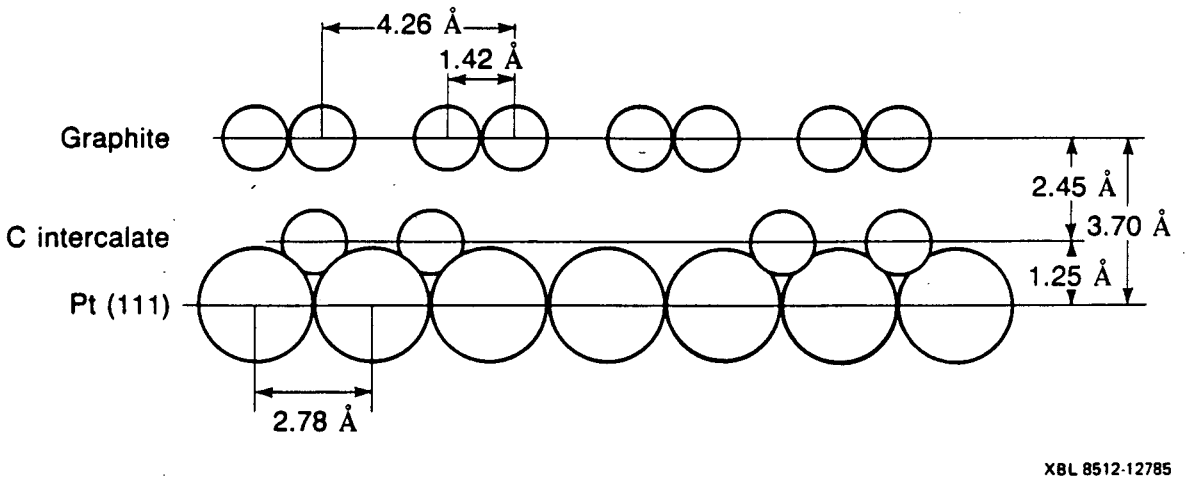

Figure 7.2: Surface side-view depicting carbidic carbon intercalated between a graphite overlayer and the platinum substrate. This model is used to explain the unusually large graphite-platinum bond distance measured by LEED. (Figure courtesy of D. F. Ogletree.)

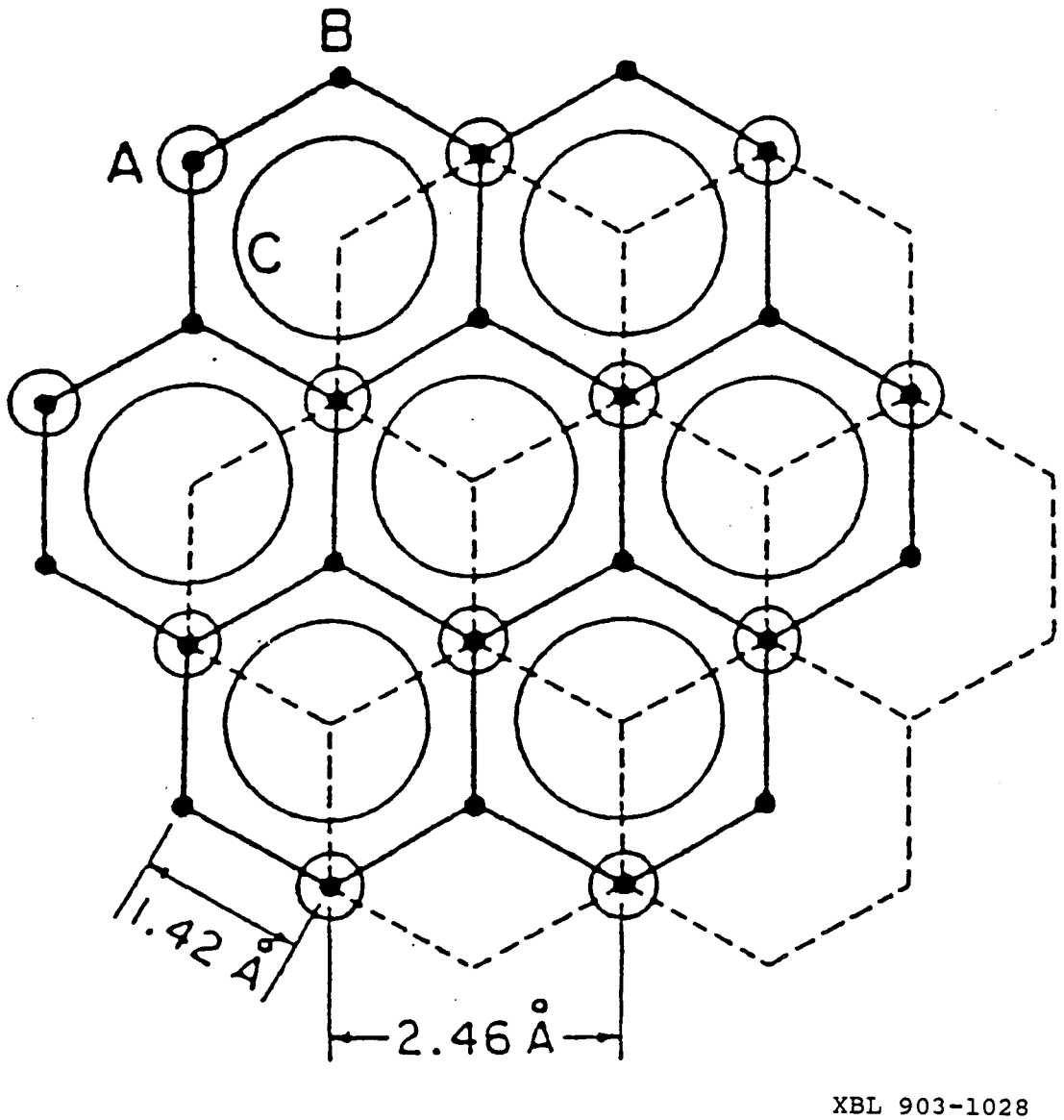

Figure 7.3: Graphite surface top view. The second layer is represented by dashed lines. A sites (circled dots) have second layer neighbors, B sites do not, and C sites are the holes in the center of the surface hexagon extending to the second layer.

show the bulk band structure of the imaged states collapses to a point on the surface Brillouin zone. As the bias voltage increases, the states' energy dispersion decreases, and the asymmetry is reduced. The goal was to to prepare a single graphitic layer on a metal surface to determine whether the corrugation enhancement was indeed a graphite second layer effect, and to provide further information on graphite layer growth.

7.2 Overlayer Preparation

The graphite surface was prepared by first exposing a Pt(111) single crystal to air. The crystal was transferred to the chamber and heated in UHV to $\sim$ 900 °C. Near this temperature carbon will dissolve into the bulk platinum. An AES spectrum indicated graphitic carbon was present on the surface (Fig. 7.4). The lineshape of the carbon *KVV* transition at 272 eV indicates a graphitic carbon overlayer.[17] The previous work indicates a single monolayer of graphite forms at a carbon 272 eV Auger peak to platinum 237 eV peak ratio of $\sim$ 3.7. The peak ratio from Figure 7.4 is 2.1, representing less than a monolayer average coverage. A LEED pattern (Fig. 7.5) shows the ring-like overlayer spots known to occur for an incommensurate graphitic overlayer on Pt(111) single crystals.[10]

7.3 STM Results and Discussion

The STM used to image the surface is a design slightly different from that described in Part III. Modifications were made to improve microscope performance and reliability. The differences were: piezo tripod instead of piezo tubes, differential micrometer driven spring instead of inertial approach, single-stage in-vacuum vibration isolation (viton cord) instead of Cu-Be springs and stacked plates, and pneumatic[18] chamber isolation instead of air table legs. An image of the surface taken in UHV is shown in Figure 7.6. The image is 15×15 Å taken at -0.3 V bias and 70 MΩ gap resistance. The maximum tunnel current is 5 nA. This image clearly depicts a surface that images like bulk graphite. The six graphite atoms in the surface hexagon are visible as well as the

[17] M. P. Hooker and G. T. Grant, *Surface Science*, vol. 62, p. 21, 1977.
[18] Barry Controls, Burbank, CA, Model SLM-3.

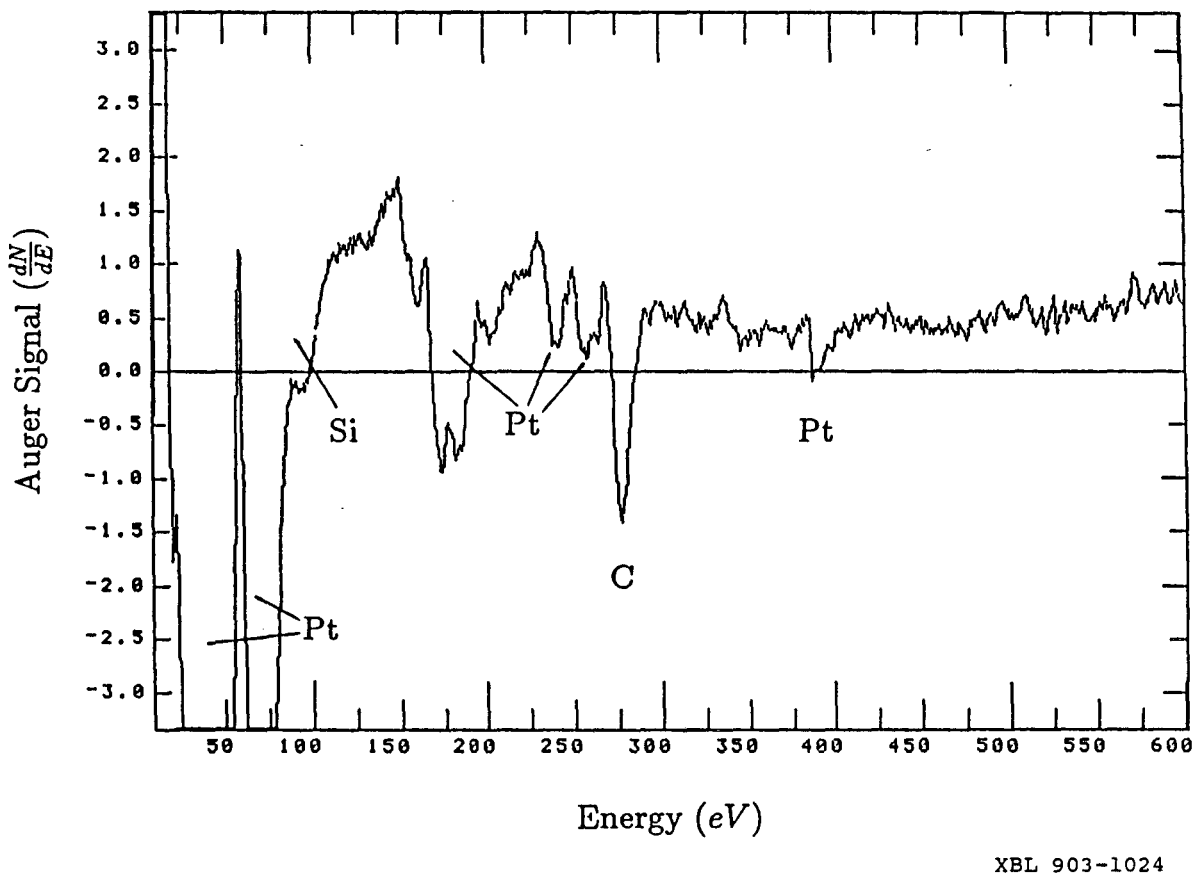

Figure 7.4: Auger electron spectrum of the graphitic carbon layer on the Pt(111) surface. The lineshape of the KVV carbon transition at 272 eV indicates graphitic surface carbon.

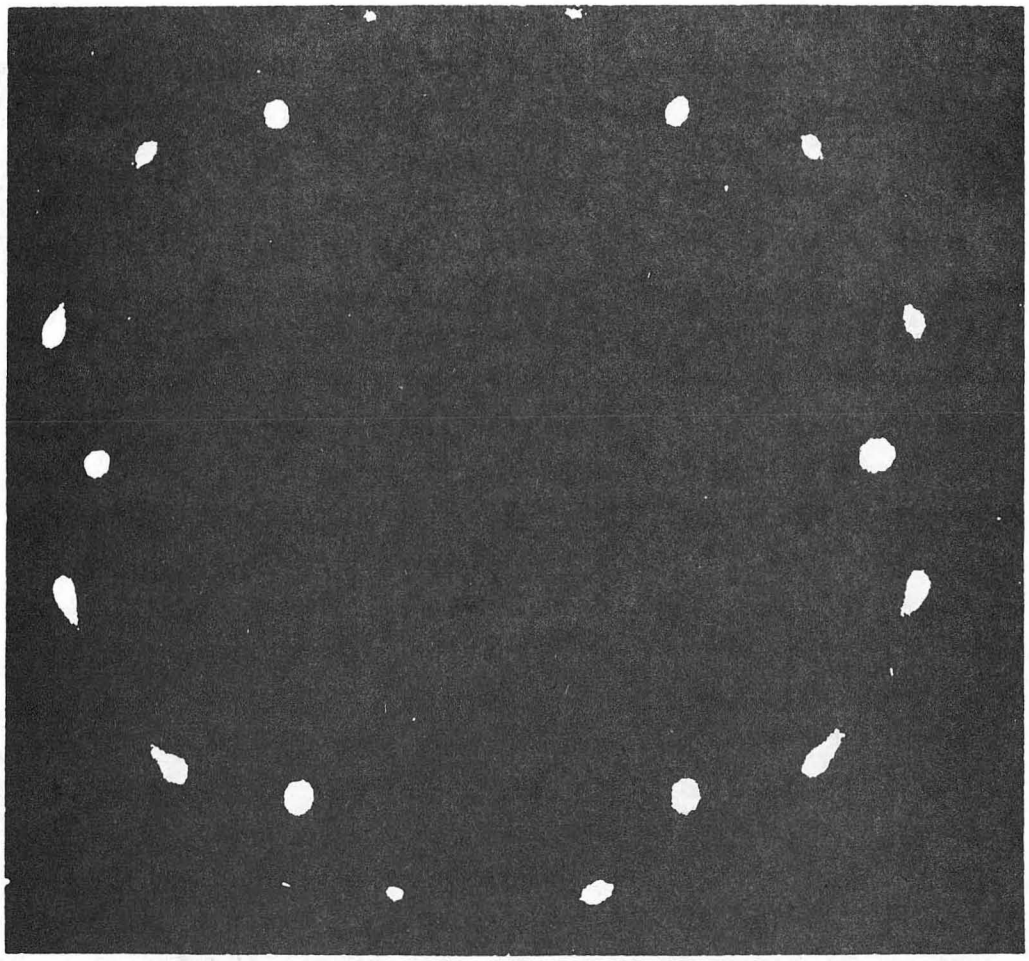

XBL 903-1027

Figure 7.5: Low energy electron diffraction pattern of the Pt(111)/C(gr) surface taken an 55 eV. The ring-like overlayer spots at long radius in the pattern indicate an incommensurate graphitic overlayer. The first-order substrate spots are visible inside the overlayer spots. This indicates the graphite unit cell (2.46 Å) is smaller than the Pt-Pt unit cell (2.78 Å).

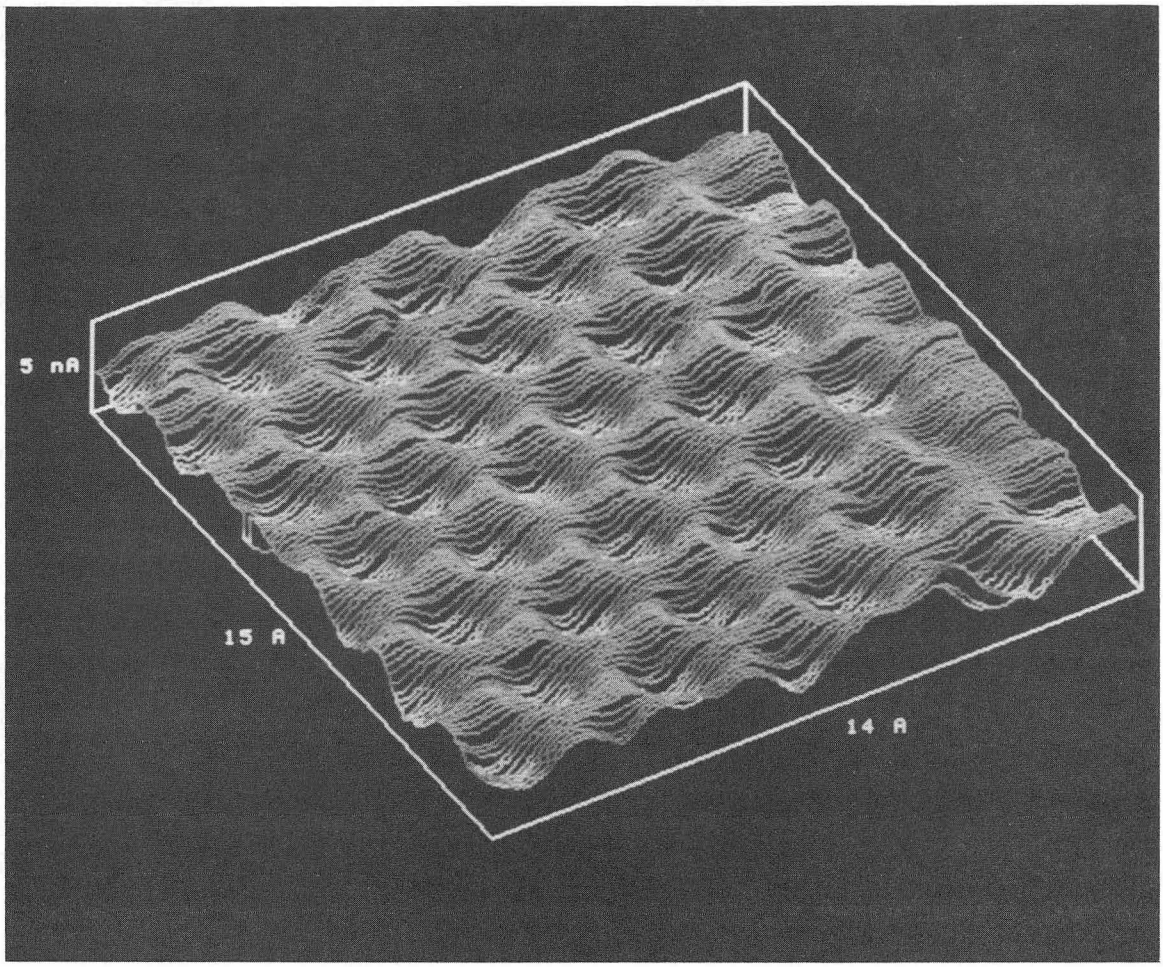

Figure 7.6: Current image of the Pt(111)/C(gr) surface. The image is 15×15 Å, and clearly indicates the three-fold symmetry observed on high-resolution bulk graphite images.

BBC 882-1484

A, B and C corrugation differences (See fig. 7.3). This image is representative of the various images taken in this study, and indicates the STM is sensitive to second-layer electronic effects. Image variation was found, and thought to be due to changes in instrument stability.

When this data was taken, the local surface coverage could not be determined with the STM. It appears that Figure 7.6 represents an area of the surface which resembles bulk graphite. It is unclear whether this area contains a single graphitic layer or multi-layers of graphite. This particular question is important, and requires an answer in order to compare this study to bulk graphite results. Experimental considerations deterred further STM work on this system. Currently, the laboratory is returning to STM studies on the Pt(111) surface. Imaging the disappearance of the surface asymmetry in a single graphitic overlayer for a range of bias voltages could provide experimental evidence supporting the theory.[15,16] Some experiments will involve adsorption of alkenes on the surface followed by systematic dehydrogenation of the surface species. The reaction mechanism shown in Figure 7.1 will be studied in more detail with STM to provide real space data on the surface species found in previous work.

Chapter 8

Sulfur on the Re(0001) Surface

8.1 Introduction

Sulfur is a major impurity in some metals, and is found as a contaminant in crude oil. Rhenium and platinum alloys are used in industry for hydrocarbon reforming.[1] Sulfur interaction with this catalyst is believed to decrease unwanted hydrogenolysis and increase catalyst lifetime.[2] Removal of sulfur, or controlling its effects occupies a substantial portion of industrial refining and metallurgical effort. Sulfur is known to enhance electrochemical dissolution, and possibly promotes localized corrosion. Its behavior in aqueous solution[3,4] and in metals[5–10] has been observed. Surface studies of catalyst poisoning have shown sulfur binds strongly to sites considered important for catalytic reactions, effectively blocking adsorption of reactant species, or weakening adsorbate metal bonds.[11,12] Without a thorough knowledge of surface processes in these systems, hypotheses explaining the role of sulfur lack some validity.

Sulfur chemisorption on metals has been widely studied. Models have been pro-

[1] J. H. Sinfelt, *Bimetallic Catalysts: Discoveries, Concepts, and Applications*, John Wiley & Sons, Inc., 1983.

[2] V. K. Shum, J. B. Butt, W. M. H. Sachtler, *Journal of Catalysis*, vol. 96, p. 371, 1985.

[3] Z. A. Iofa, *Electrochimica Acta*, vol. 9, p. 1645, 1964.

[4] M. Kesten, *Corrosion*, vol. 32, p. 94, 1976.

[5] W. Schatt and H. Worch, *Corrosion Science*, vol. 11, p. 623, 1971.

[6] G. W. Marshall and M. T. Jones, *Corrosion Science*, vol. 14, p. 15, 1974.

[7] G. A. Dibari and J. V. Petrocelli, *Journal of the Electrochemical Society*, vol. 112, p. 99, 1965.

[8] Z. Szklarska-Smialowska, *Corrosion*, vol. 28, p. 388, 1972.

[9] G. Wranglen, *Corrosion Science*, vol. 14, p. 331, 1974.

[10] G. S. Eklund, *Journal of the Electrochemical Society*, vol. 121, p. 467, 1974.

[11] *Deactivation and Poisoning of Catalysts*, Edited by J. Oudar and H. Wise, Marcel Dekker, Inc., 1985.

[12] *Catalyst Poisoning*, Edited by E. E. Peterson and A. T. Bell, Marcel Dekker, Inc., 1987.

posed for many sulfur structures.[13] Dynamical analysis of LEED data has predicted unit-cell contents and binding sites for systems having one or two atom basis superlattices.[14] It is found that sulfur prefers the three-fold or four-fold hollow sites. A summary of this work is given in Table 8.1. The structures studied are low coverage, and sulfur tends to form open surface lattices. LEED has been the primary technique for surface structure determination of these systems. At present, STM is the only technique which can provide real space, atomic resolution information for solving the complex higher coverage structures. High coverage sulfur structures have recently been studied with LEED and STM. Since atomic resolution has been obtained in air for sulfur on the Mo(100)[15] and Re(0001)[16] surfaces at saturation coverage, UHV studies of the sulfur structures on the Re(0001) surface were performed.

On the Mo(100) surface, sulfur forms a c(2×2) overlayer at $\Theta_S = 0.50$,[17,18] as shown in Table 8.1. The sulfur sits in four-fold hollow sites on the (100) face. Above one-half monolayer coverage, sulfur forms a $\begin{bmatrix} 2 & -1 \\ 1 & 1 \end{bmatrix}$ structure at $\Theta_S = 0.67$, a c(4×2) structure at $\Theta_S = 0.75$, and a p(2×1) structure at the saturation coverage, $\Theta_S = 1$.[19,20] An STM study in air of the Mo(001)/S-p(2×1) system imaged the bonding arrangement of the sulfur overlayer.[15] There is some disagreement among workers as to which bonding site the sulfur prefers in high coverage structures. The STM study provided evidence for sulfur bonding in asymmetric off-bridge sites, while total energy calculations for this structure indicate sulfur bonds in alternating rows at bridge and hollow sites.[21] Current and future studies on this system involve LEED intensity analysis and UHV-STM imaging. Possibly, these experiments can resolve

[13]H. Ohtani, C.-T. Kao, M.A. Van Hove, and G.A. Somorjai, *Progress in Surface Science*, vol. 23, p. 155, 1986 provide tabulation of these results and author references.

[14]J.M. MacLaren, J.B. Pendry, P.J. Rous, D.K. Saldin, G.A. Somorjai, M.A. Van Hove, and D.D. Vvedensky, *Surface Crystallographic Information Service: A Handbook of Surface Structures*, D. Reidel Publishing Co., 1988, and references therein.

[15]B. Marchon, P. Bernhardt, M.E. Bussell, G.A. Somorjai, M. Salmeron, and W. Siekhaus, *Physical Review Letters*, vol. 60, p. 1166, 1988.

[16]D.F. Ogletree, C. Ocal, B. Marchon, G.A. Somorjai, M. Salmeron, T. Beebe, and W. Siekhaus, *Journal of Vacuum Science and Technology A*, vol. 8, p. 297, 1990.

[17]D.G. Kelly, R.F. Lin, M.A. Van Hove, and G.A. Somorjai, *Surface Science*, vol. 224, p. 97, 1989.

[18]L.J. Clarke, *Surface Science*, vol. 102, p. 331, 1981.

[19] M. Salmeron, G.A. Somorjai, and R.R. Chianelli, *Surface Science*, vol. 127, p. 526, 1983.

[20] V. Maurice, L. Peralta, Y. Berthier, and J. Oudar, *Surface Science*, vol. 148, p. 623, 1984.

[21]X.W. Wang and S.G. Louie, Department of Physics, University of California, Berkeley, CA, to be published.

Crystal Face	Structure	Θ_S	Substrate
	fcc metals		
(100)	p(2×2)	0.25	Cu, Ni, Rh
	c(2×2)	0.50	Co, Mo, Ni, Pd
(110)	p(2×2)	0.25	Ni
	p(2×2)	0.50	Ir
	c(2×2)	0.50	Ni, Rh
(111)	p(2×2)	0.25	Ni
	$(\sqrt{3} \times \sqrt{3})$R30°	0.33	Ir, Pd, Pt, Rh
	bcc metals		
(100)	c(2×2)	0.50	Fe
(110)	p(2×2)	0.25	Fe

Table 8.1: Summary of some sulfur chemisorption studies on metal substrates. The superlattice basis consists of one or two atoms, and LEED intensity analysis has indicated sulfur binds in four-fold or three-fold hollow sites.

the binding site question and provide an accurate model for the $\begin{bmatrix} 2 & -1 \\ 1 & 1 \end{bmatrix}$ and c(4×2) structures.

Previous model catalytic studies of the Re(0001)/S system have found a variety of structures.[22] The AES and LEED results are shown in Table 8.2. The structures formed are: p(2×2) at $\Theta_S = 0.16-0.29$, $(3\sqrt{3}\times3\sqrt{3})$R30° at $\Theta_S = 0.32-0.39$, $\begin{bmatrix} 3 & 1 \\ 1 & 3 \end{bmatrix}$ at $\Theta_S = 0.39-0.44$, and $(2\sqrt{3}\times2\sqrt{3})$R30° at $\Theta_S = 0.44-0.59$ saturation coverage. The original study proposed several real space models for these structures. The LEED results have not undergone intensity analysis, making it difficult to accurately predict the contents of the surface unit cell. The $(3\sqrt{3}\times3\sqrt{3})$R30° structure was written in quotes since the LEED pattern contained missing diffraction spots at all energies along certain azimuthal directions. The STM results presented in the next sections provide real space information on these structures, and the origin of the missing spots is given.

Microscope calibration was previously done in air with a graphite sample. In order to reduce calibration error, the sample was transfered to the chamber after bakeout resulting in a background pressure of 5.0×10^{-10} torr. Using this calibration method, distances measured on STM images agreed well with those measured by LEED. Vertical calibration was done by scanning over atomic height steps on the Re(0001) surface. The Re(0001) layer spacing is 4.46 Å.

8.2 Overlayer Preparation

In order to prepare the sulfur structures, a Re(0001) single crystal was cleaned in UHV by repeated heating to 1000-1200 °C in 1.0×10^{-7} torr of oxygen until carbon could not be detected with AES. A quick temperature flash at 1.0×10^{-9} torr background pressure after oxygen treatment removed adsorbed oxygen. An optical pyrometer monitored the crystal temperature, and typically, heating and flashing to ~1800 °C was necessary to remove surface impurities. Sulfur was adsorbed as H_2S onto the crystal held at the temperatures indicated in Table 8.2. The H-S bonds break upon adsorption and sulfur can diffuse across the surface. The ordered structures were

[22] D. G. Kelly, A. J. Gellman, M. Salmeron, G. A. Somorjai, V. Maurice, M. Huber, and J. Oudar, *Surface Science*, vol. 204, p. 1, 1988.

θ_S	AES peak ratio S(152 eV)/Re(177 eV)	Structure	Annealing temperature (K)
0.0 –0.16	0.0–1.0	1×1	1650–1500
0.16–0.29	1.0–2.4	$p(2\times2)$	1450–1400
0.29–0.32	2.4–2.8	1×1	1380–1350
0.32–0.39	2.8–4.3	"$(3\sqrt{3}\times3\sqrt{3})R30°$"	1340–1220
0.39–0.44	4.3–5.3	$\begin{pmatrix}3&1\\1&3\end{pmatrix}$	1210–1100
0.44–0.59	5.3–7.1	$(2\sqrt{3}\times2\sqrt{3})R30°$	1090– 600

XBL 903-1026

Table 8.2: Sulfur chemisorption on the Re(0001) surface; overlayer structures, annealing temperatures, and coverage ranges from AES. (Table courtesy of D. G. Kelly.)

formed by repeated two minute H_2S dosing cycles at 2.0×10^{-8} torr until LEED indicated the desired overlayer. Figure 8.1 shows the LEED patterns obtained from the various structures, and Figure 8.2 diagrams the patterns. Along the [110]* direction (the asterisk represents a reciprocal lattice vector), the first, third, sixth and eighth spots are missing. The phenomenon giving zero intensity will be discussed when the data obtained on this structure is presented. The LEED pattern from the $\begin{bmatrix} 3 & 1 \\ 1 & 3 \end{bmatrix}$ structure shows that three rotationally-equivalent domains exist on the surface producing triangular arrays of spots. In addition to the structures observed with LEED, STM has imaged several structures formed in small domains which cannot be seen with LEED. The data for the Re(0001)/S structures will be presented beginning at low sulfur coverage.

8.3 STM Results and Discussion

c($\sqrt{3}\times5$) Structure

Figure 8.3 shows an STM topographic image of a structure not seen with LEED. The c($\sqrt{3}\times5$) structure (local $\Theta_S = 0.20$) exists as $\sim$100Å domains on a surface giving a p(2×2) LEED pattern. The image was taken at -0.2 V bias, 2 nA current setpoint, and 100 MΩ gap resistance. In this image, the substrate rhenium is imaged between the rows of sulfur atoms.

Figures 8.3(b) and (c) show that STM images the sulfur and rhenium atoms as 3.0 Å and 0.5 Å corrugations, respectively. Using the covalent radii for sulfur (1.02 Å) and rhenium (1.38 Å) and a platinum tip (covalent radius: 1.39 Å), a hard-sphere calculation gives a maximum measurable corrugation of 1.87 Å for sulfur and 0.37 Å for rhenium. Without a detailed calculation for the vacuum gap, it is difficult to identify the effects contributing to the corrugation enhancement. Tip/surface forces are believed to contribute, but clear experimental evidence of this does not exist. The sulfur also appears oblate, possibly due to the effect the surface asymmetry has on the LDOS. Figure 8.4 is a model of the c($\sqrt{3}\times5$) overlayer on the Re(0001) surface. From the STM image, sulfur is known to sit in three-fold sites (fcc) on the rhenium surface. The fcc site is chosen since it is found to be the adsorption site on other surfaces (see Table 8.1), and represents a continuation of the bulk lattice. The

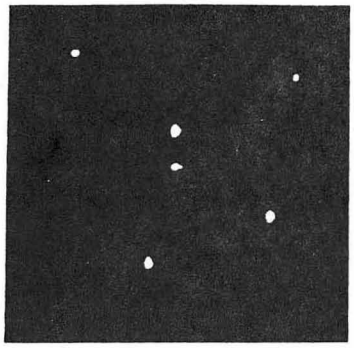

Clean Re(0001), 72 eV

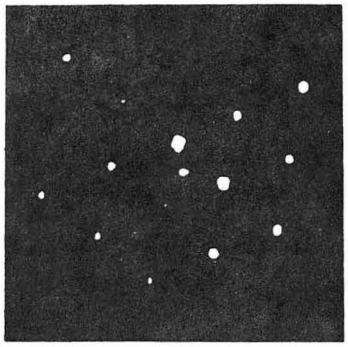

p(2×2), $\Theta_S = 0.25$, 69 eV

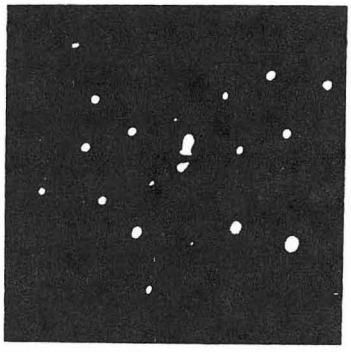

$\left(3\sqrt{3} \times 3\sqrt{3}\right)$ R30°, $\Theta_S = \sim 0.44$, 57 eV

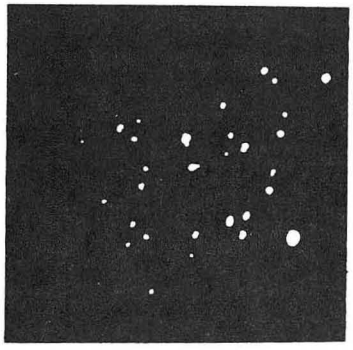

$\begin{bmatrix} 3 & 1 \\ 1 & 3 \end{bmatrix}$, $\Theta_S = \sim 0.47$, 53 eV

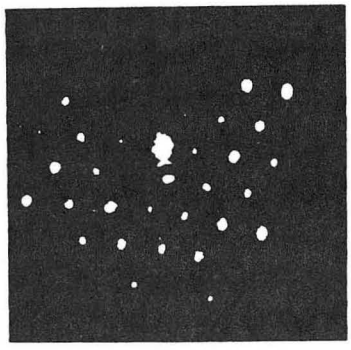

$\left(2\sqrt{3} \times 2\sqrt{3}\right)$ R30°, $\Theta_S = 0.50$, 73 eV

XBL 903-1030

Figure 8.1: LEED patterns for the Re(0001)/S overlayer structures. The clean Re(0001) pattern is also given.

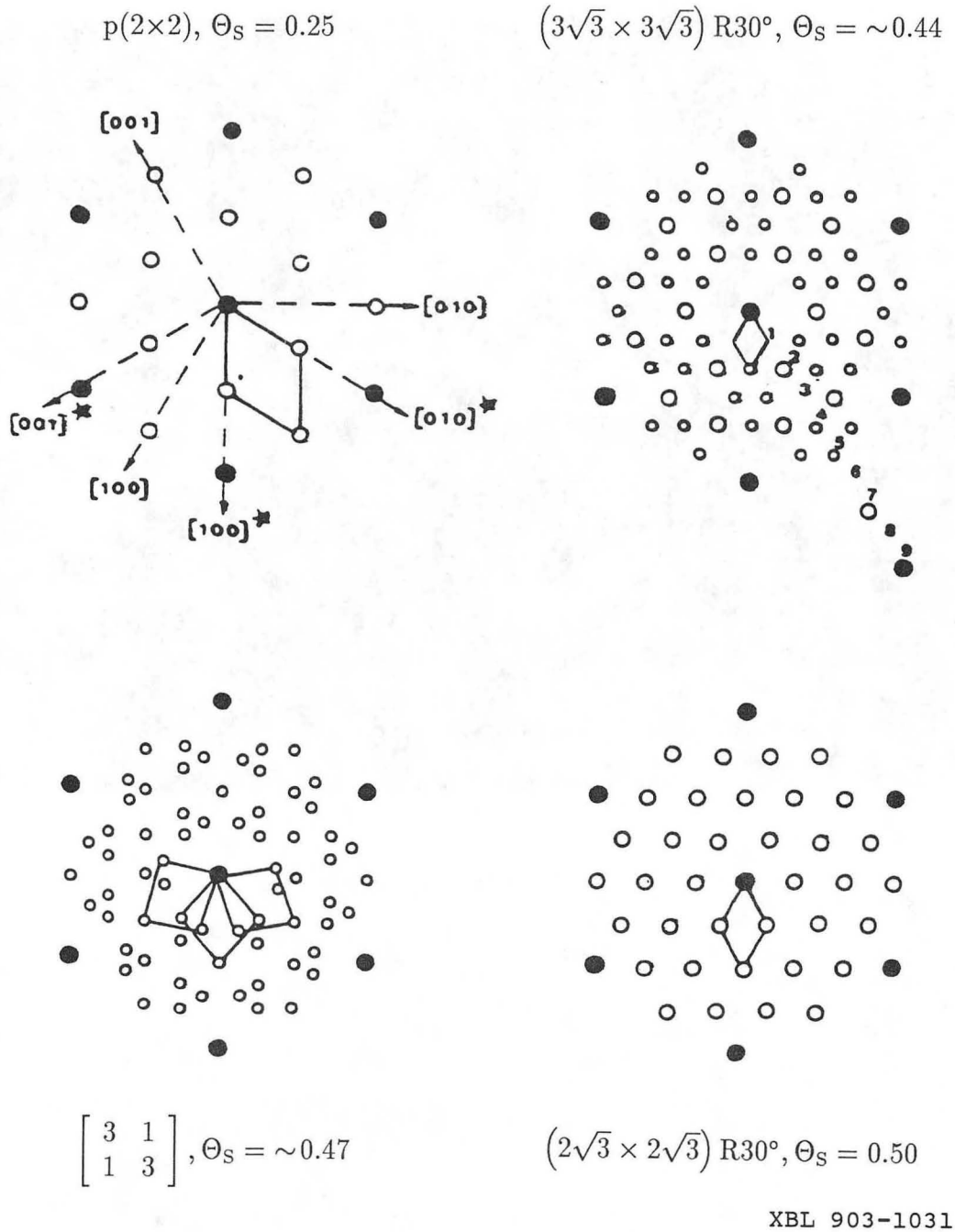

Figure 8.2: Diagrams for the diffraction patterns presented in Figure 8.1. The asterisk represents a reciprocal lattice vector. The $(3\sqrt{3}\times3\sqrt{3})$R30° pattern is discussed in detail in the text.

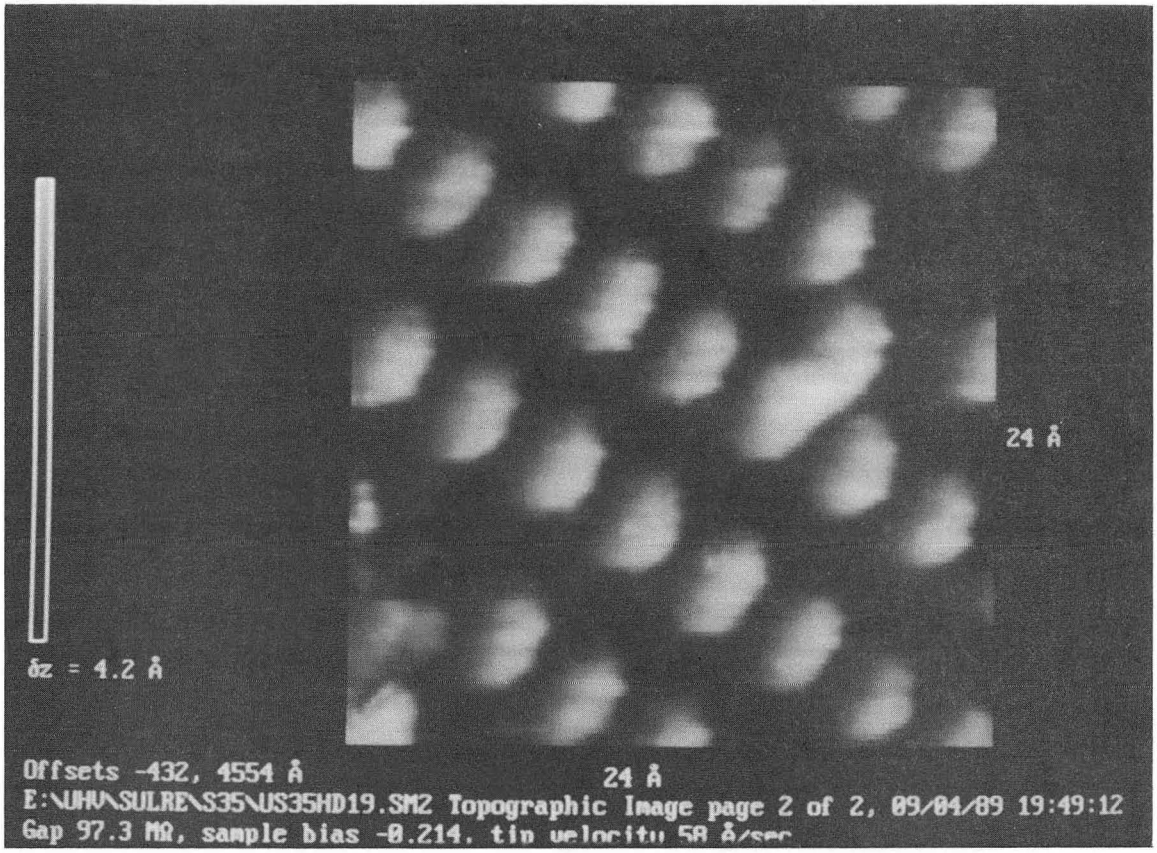

Figure 8.3: (a) Topographic image of the c($\sqrt{3}\times5$) overlayer. The substrate rhenium atoms are visible between the rows of sulfur. A defect in which a sulfur atom has shifted position can be seen in the upper right corner of the image.

BBC 903-2319

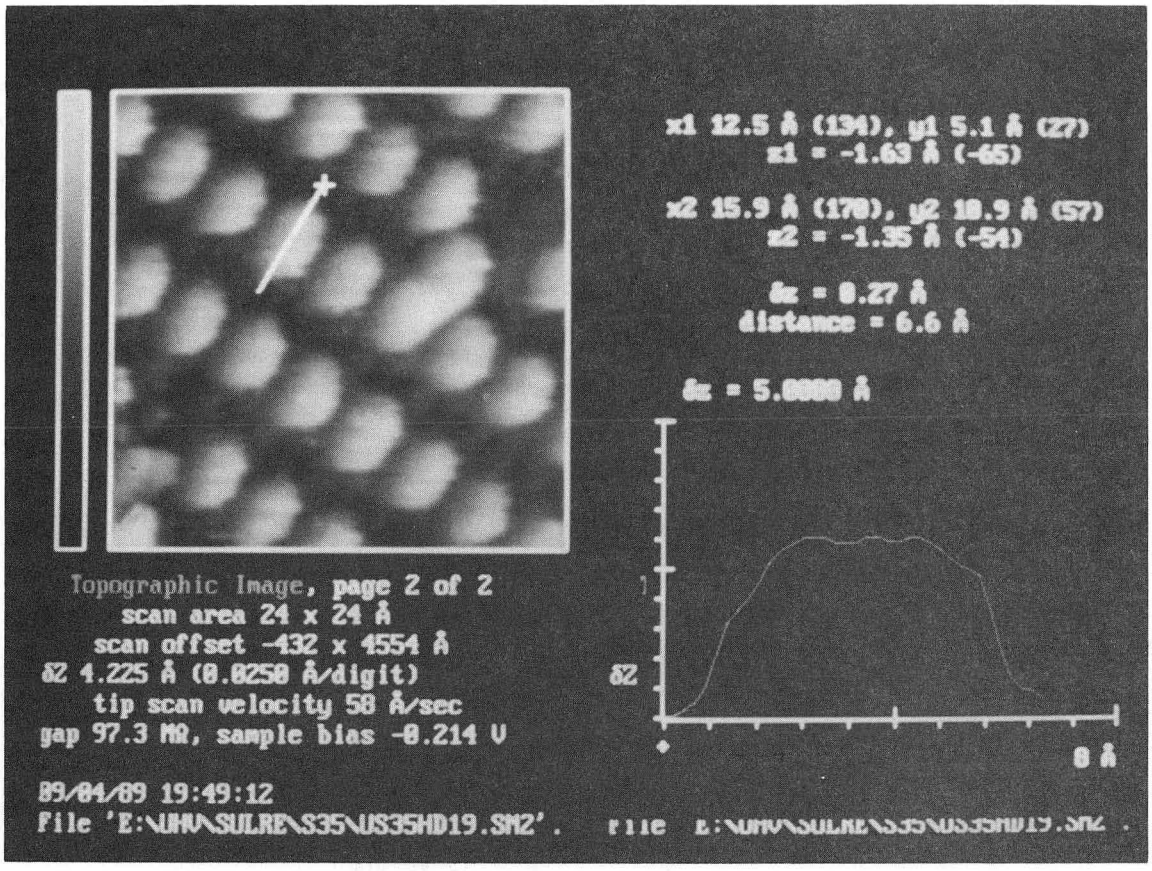

Figure 8.3: (b) A cursor cross section indicates the STM images the sulfur atoms with 3.0 Å corrugation, greater than expected from a hard-sphere model.

BBC 903-2331

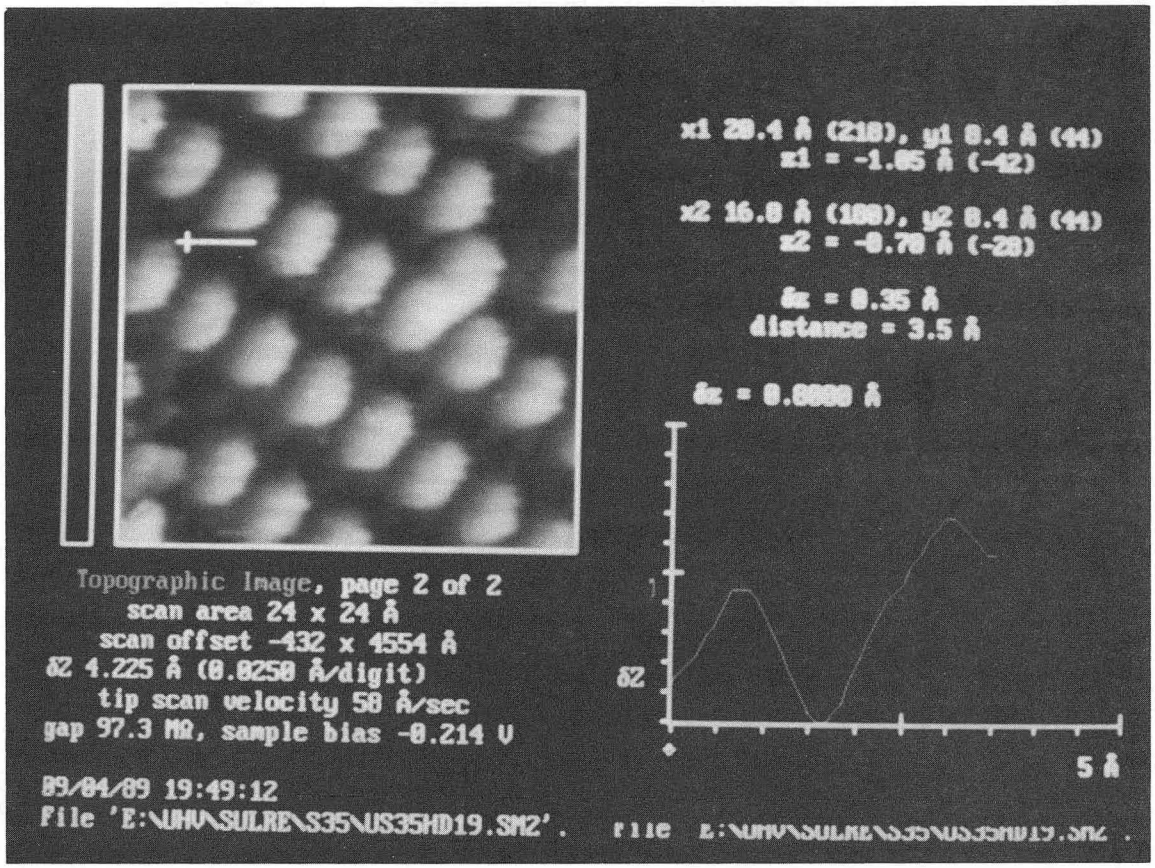

Figure 8.3: (c) This cursor cross section shows rhenium atoms are imaged as $\sim$0.5Å corrugations, greater than expected from a hard-sphere model.

BBC 903-2325

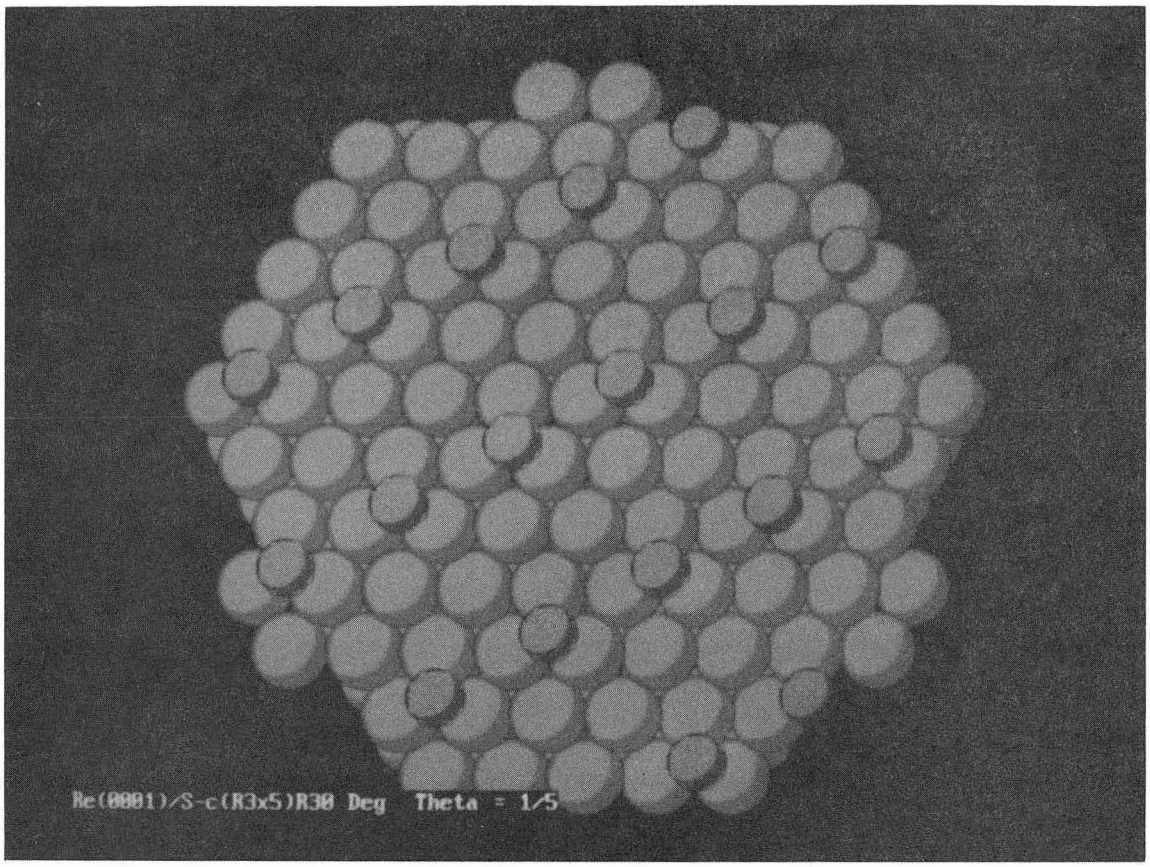

Figure 8.4: Real space model for the Re(0001)/S-c($\sqrt{3}\times5$) structure. The STM image shows sulfur sits in three-fold hollow sites. The substrate atoms imaged are those between the sulfur rows without sulfur neighbors.

BBC 903-2321

distances measured from the model correspond well with those measured from the data. It appears the rhenium atoms without sulfur neighbors are those imaged by STM. It is not clear whether an electronic enhancement is the origin of the substrate imaging, or the imaging is due to geometrical considerations (the tip must approach the substrate close enough to image the atoms). The next section will provide further evidence, from a different structure, that the microscope is imaging substrate atoms without sulfur nearest neighbors.

Figure 8.5 depicts a substrate lattice mesh overlaid onto the image. The unit cell which fits the data is 2.43×2.20 Å with an included angle of 57.1°. This agrees well with the bulk unit cell (2.76×2.76 Å, 60° included angle). The imaged rhenium atoms lie at the lattice points predicted in the model (Fig. 8.4). An interesting feature of this image is the overlayer defect seen in the upper right. Corrugation enhancements above the baseline are measured at the three lattice points where the exposed substrate atoms are expected.

p(2×2) Overlayer

The p(2×2) overlayer is presented as topographic images in Figure 8.6. Typical image parameters for the data in this section are: -0.2 V sample bias, 2 nA current setpoint, and 100 MΩ gap resistance. While the LEED pattern for the p(2×2) images is sharp, suggesting a well-ordered overlayer, many regions of p(2×2) are imaged adjacent to domains of sulfur clusters. Figures 8.6(a), (c), and (d) show ordered clusters of sulfur on the Re(0001) surface. This is unusual since for chemisorbed systems, surface ordering is believed to result from adsorbate-adsorbate repulsion. The evidence presented for coverages greater than $\Theta_S = 0.25$ indicates sulfur, adsorbed atomically, will form molecular overlayers above a certain concentration. The mixture of structures (c($\sqrt{3}$×5) and clusters) found on a p(2×2) surface could possibly explain the coverage range measured by AES (see Table 8.2), but until many images of different surface regions provide statistics, a detailed explanation is not available.

A model of the Re(0001)/S-p(2×2) system is shown in Figure 8.7. Following the reasoning used to explain the imaging of substrate atoms in a c($\sqrt{3}$×5) overlayer, this model indicates one substrate atom per unit cell lacks sulfur neighbors and should be

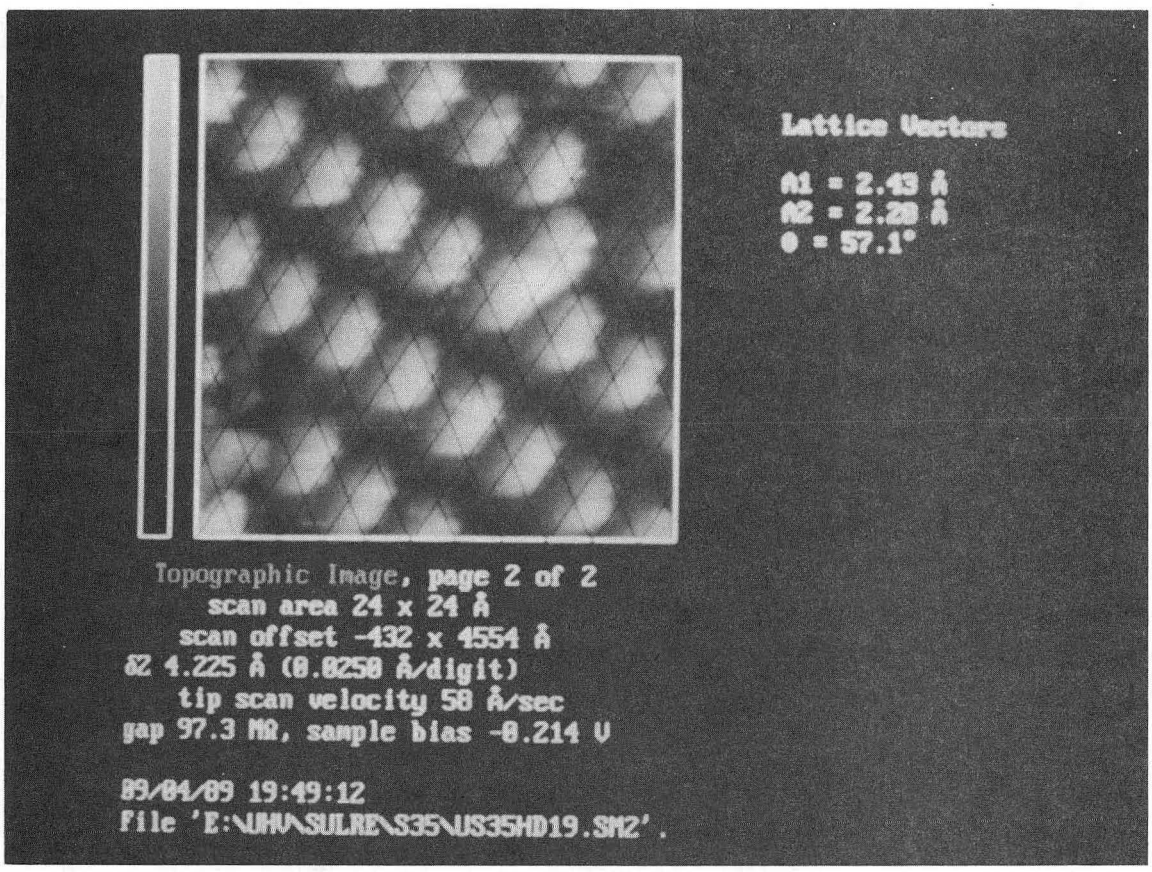

Figure 8.5: Substrate lattice mesh overlaid onto the image in Figure 8.3. The lattice points on the mesh agree well with the positions of the rhenium atoms in the image.

BBC 903-2323

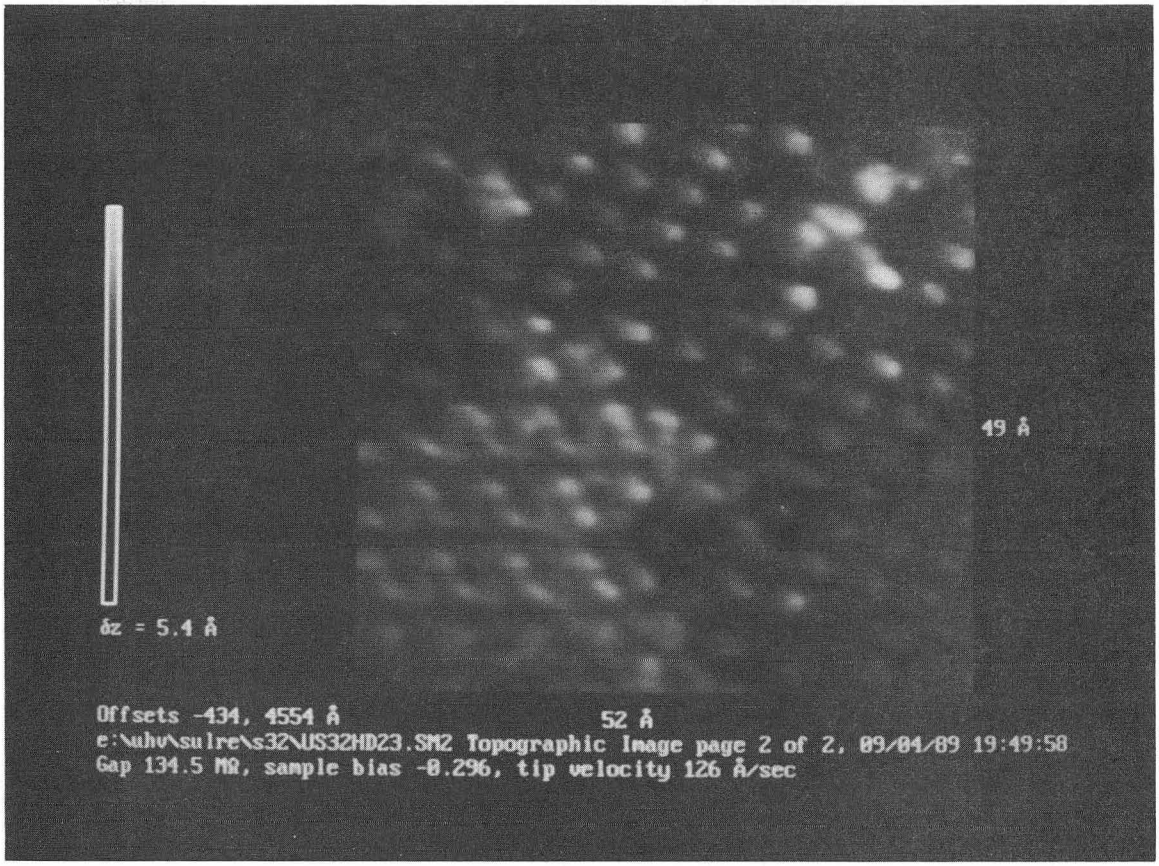

Figure 8.6: (a) p(2×2) overlayer imaged in topographic mode. Clusters of sulfur atoms are imaged at lower left.

BBC 903-2327

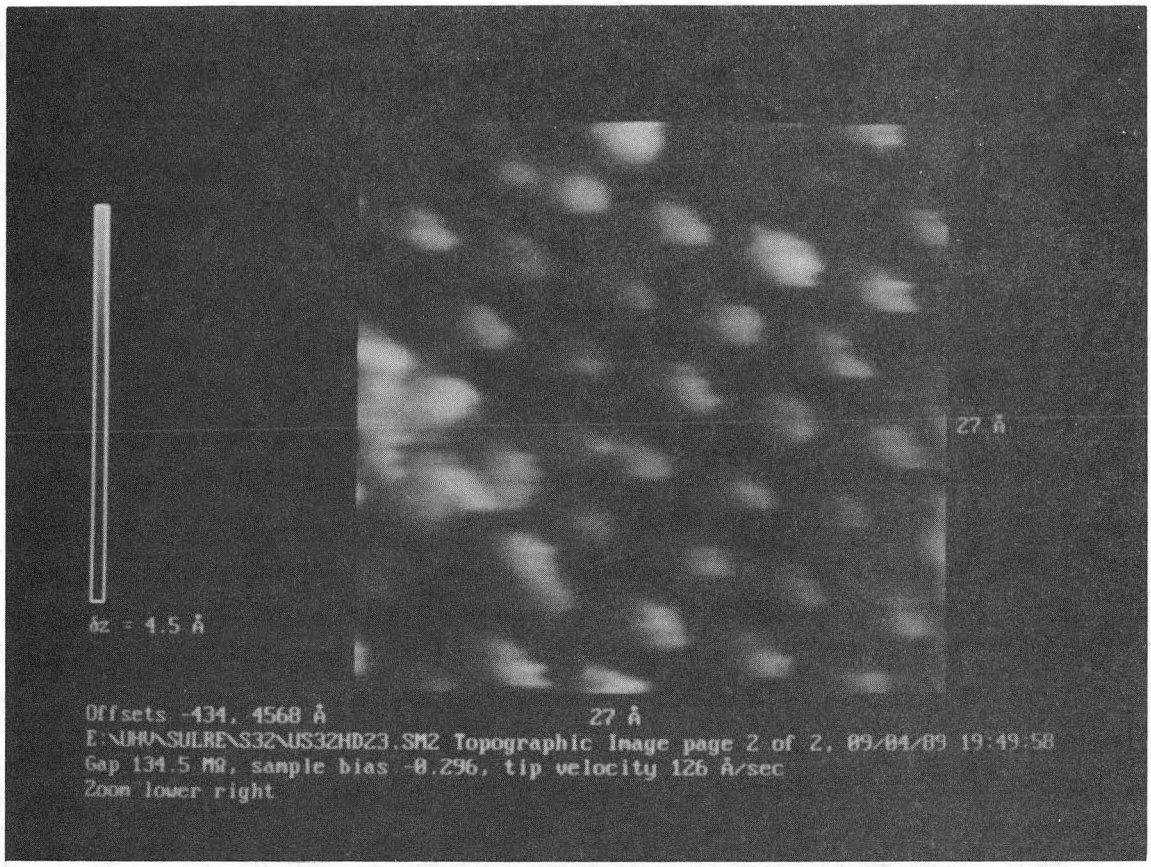

Figure 8.6: (b) Computer graphics magnification of an area at lower right of Figure 8.6(a) showing the p(2×2) structure in detail.

BBC 903-2297

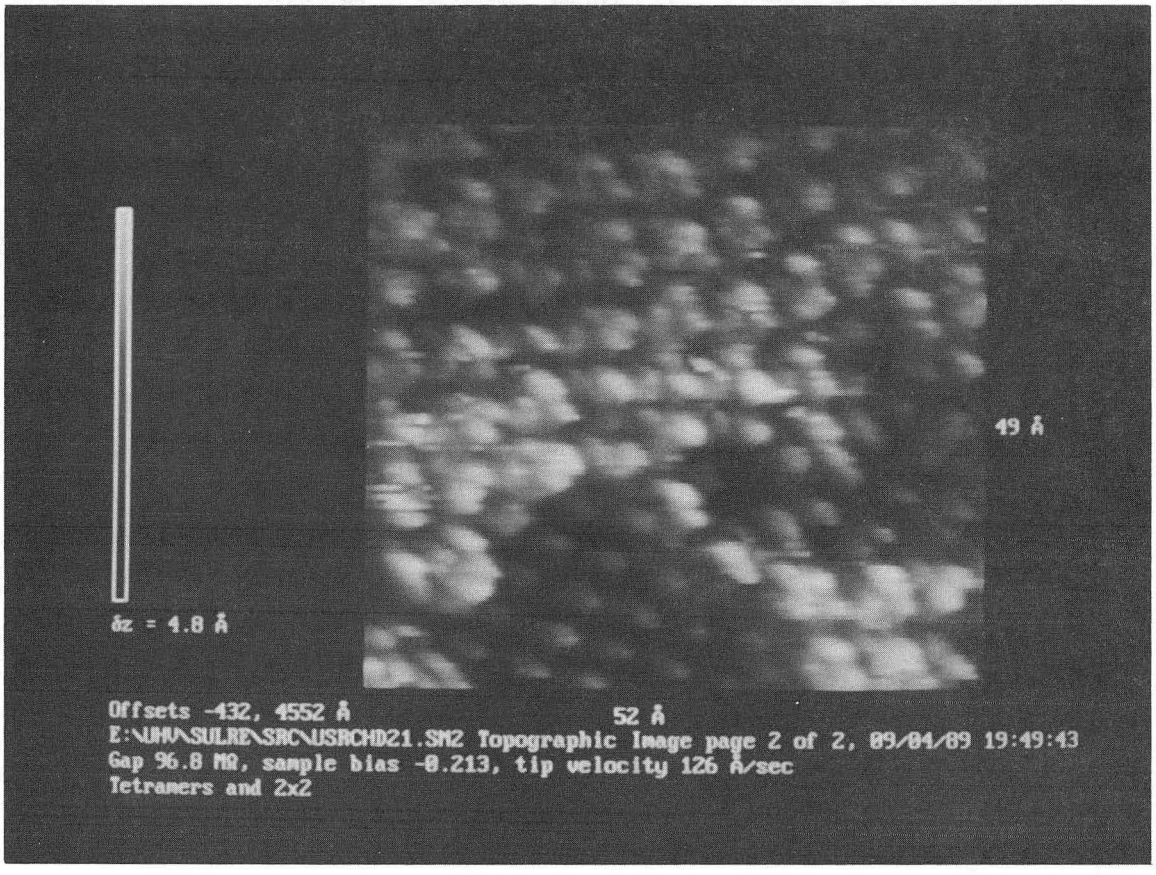

Figure 8.6: (c) Tetramers of sulfur near an atomically resolved p(2×2) region.

BBC 903-2311

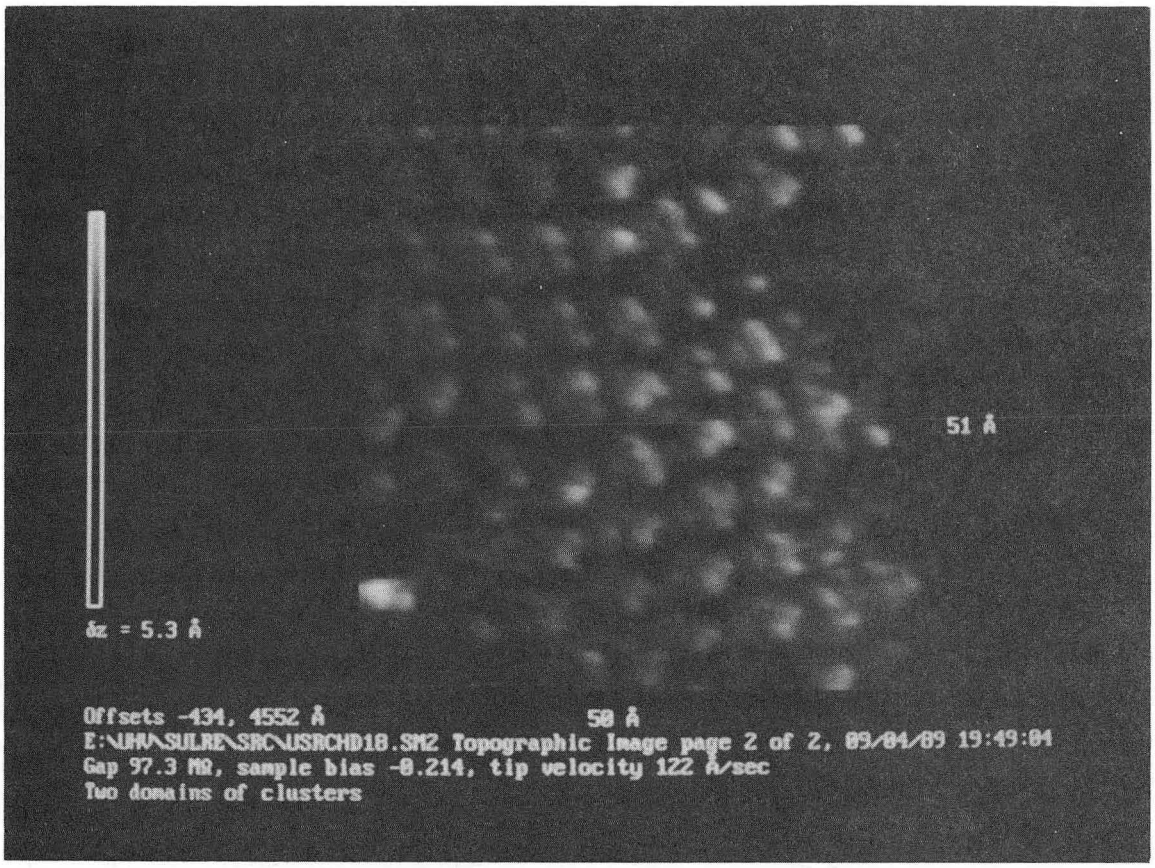

Figure 8.6: (d) Well ordered tetramers of sulfur coexisting with regions of p(2×2).

BBC 903-2329

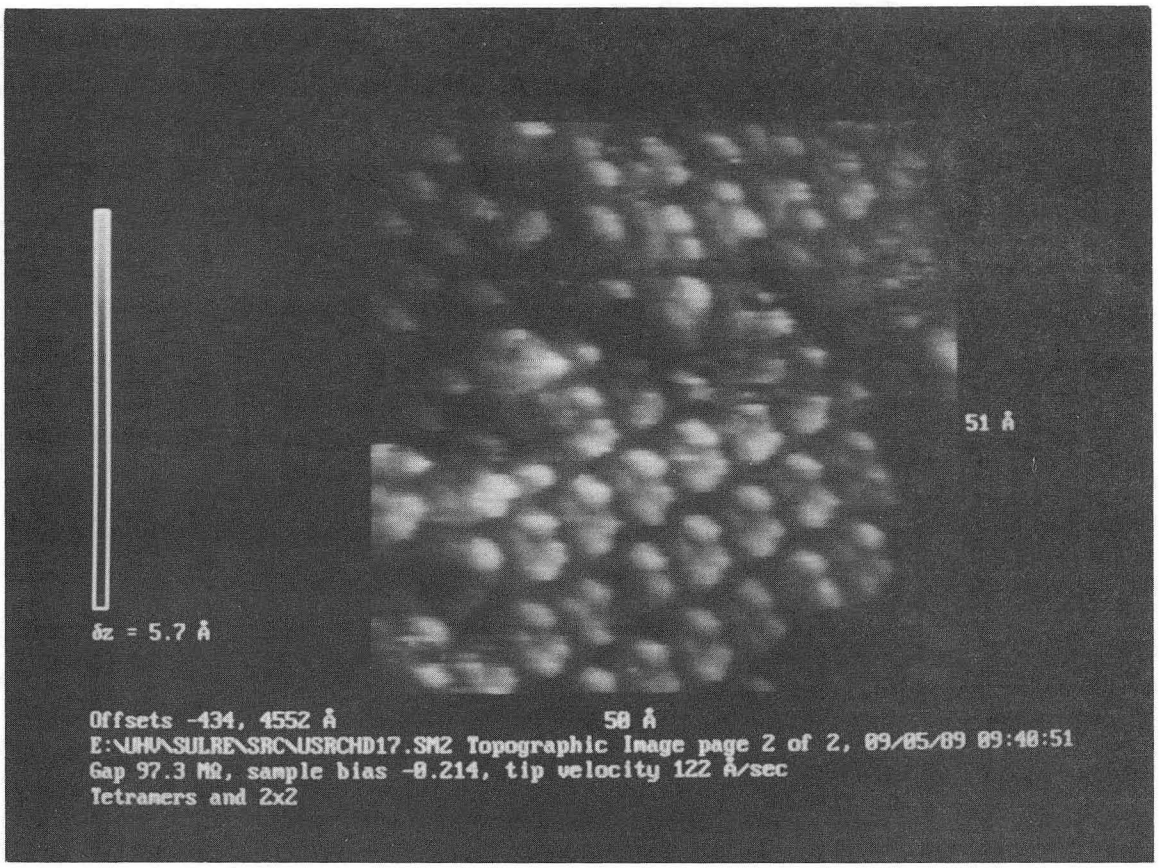

Figure 8.6: (e) Two rotational domains of tetramers. The domain orientation angle is approximately 60° suggesting substrate geometry influences overlayer formation.

BBC 903-2307

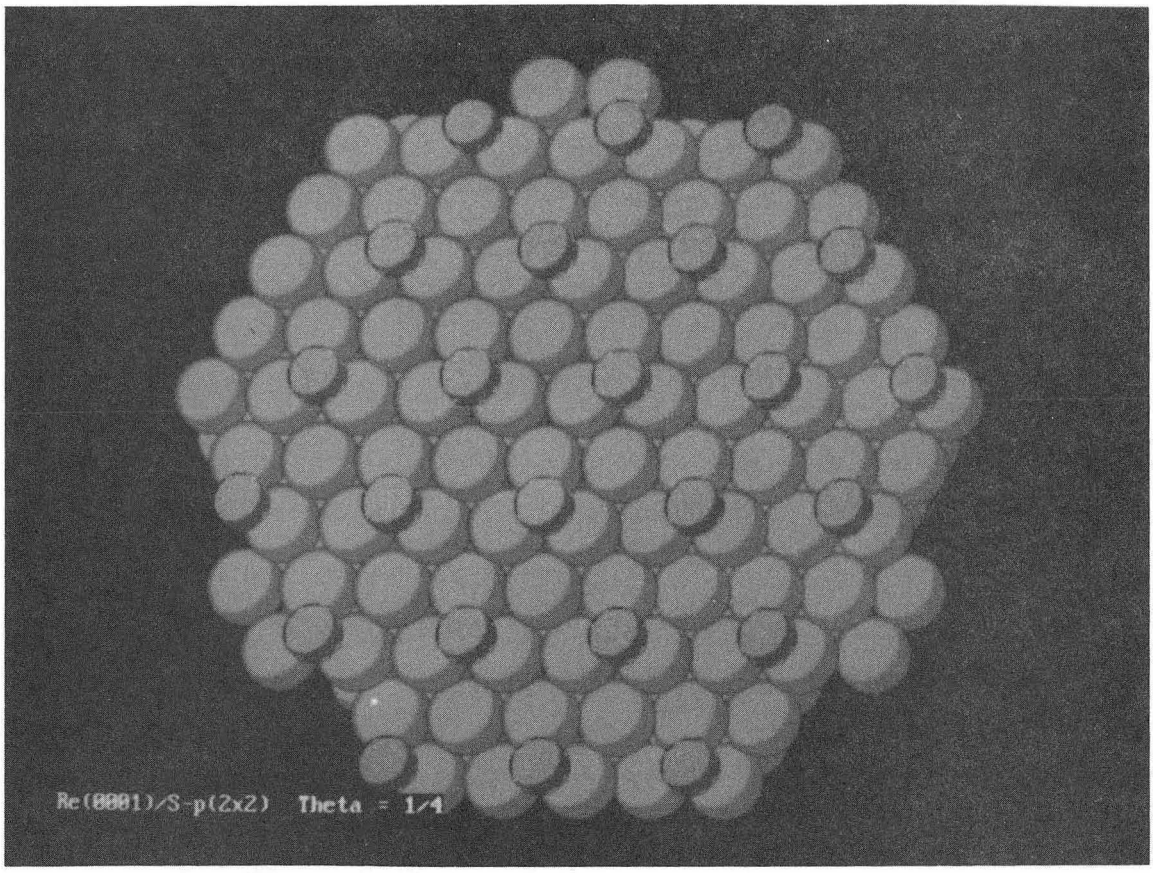

Figure 8.7: Real space model for the Re(0001)/S-p(2×2) system. One substrate atom per unit cell lacks sulfur neighbors, and is imaged by STM.

BBC 903-2317

imaged by the microscope. A computer graphics magnification of Figure 8.6(c), lower left (Fig. 8.8), shows corrugation enhancements in each corner of the p(2×2) unit cell. This position corresponds to that predicted by the model and may possibly be a general trend for high resolution STM images of open structures on metal surfaces.

$(3\sqrt{3}\times3\sqrt{3})$R30° Overlayer

The $(3\sqrt{3}\times3\sqrt{3})$R30° structure is shown in Figure 8.9. The structure consists of alternating trimeric rows. In one row, the trimers zig-zag keeping a constant rotational orientation. The adjacent row is formed by alternating pairs of tip-to-tip and back-to-back trimers. An anti-phase domain boundary (see Fig. 8.9) is made up of alternating sulfur tetramers and single sulfur atoms. This boundary serves to convert a zig-zag row to a tip-to-tip, back-to-back row. A model of this surface including the domain boundary is shown in Figure 8.10.

The fourier transform of Figure 8.10, neglecting multiple-atom basis effects, is shown in Figure 8.11. This diffraction pattern does not represent the experimental observations. Defining the origin as the specular beam (00) in Figure 8.11, and proceeding in the positive-X direction gives eight fractional-order overlayer beams between the integer-order beams. In the experimental LEED pattern (see Figures 8.1 and 8.2), fractional beams one, three, six and eight are missing at all energies. In addition, beams four and five appear with diminished intensity. Questions have arisen concerning the origin of the missing beams.[22] Using the basis seen with STM, a kinematic diffraction analysis[23] gives the missing spot LEED pattern (Fig. 8.12). Destructive interference extinguishes beams one, three, six and eight, and reduces the intensity of beams four and five. This calculation considers only single point scattering, and though not entirely accurate for LEED data, it provides a simple model predicting the experimental results.

This structure is also produced over a range of coverages measured by AES (Table 8.2). Figure 8.13 represents structures seen on several areas of a $(3\sqrt{3}\times3\sqrt{3})$R30° overlayer. Some ordering of single sulfur atoms exists, and some trimers have formed. These lower coverage areas may explain the measured range.

[23]M. A. Van Hove, W. H. Weinberg, and C.-M. Chan, *Low Energy Electron Diffraction: Experiment, Theory, and Surface Structure Determination*, Springer-Verlag, p. 91, 1986.

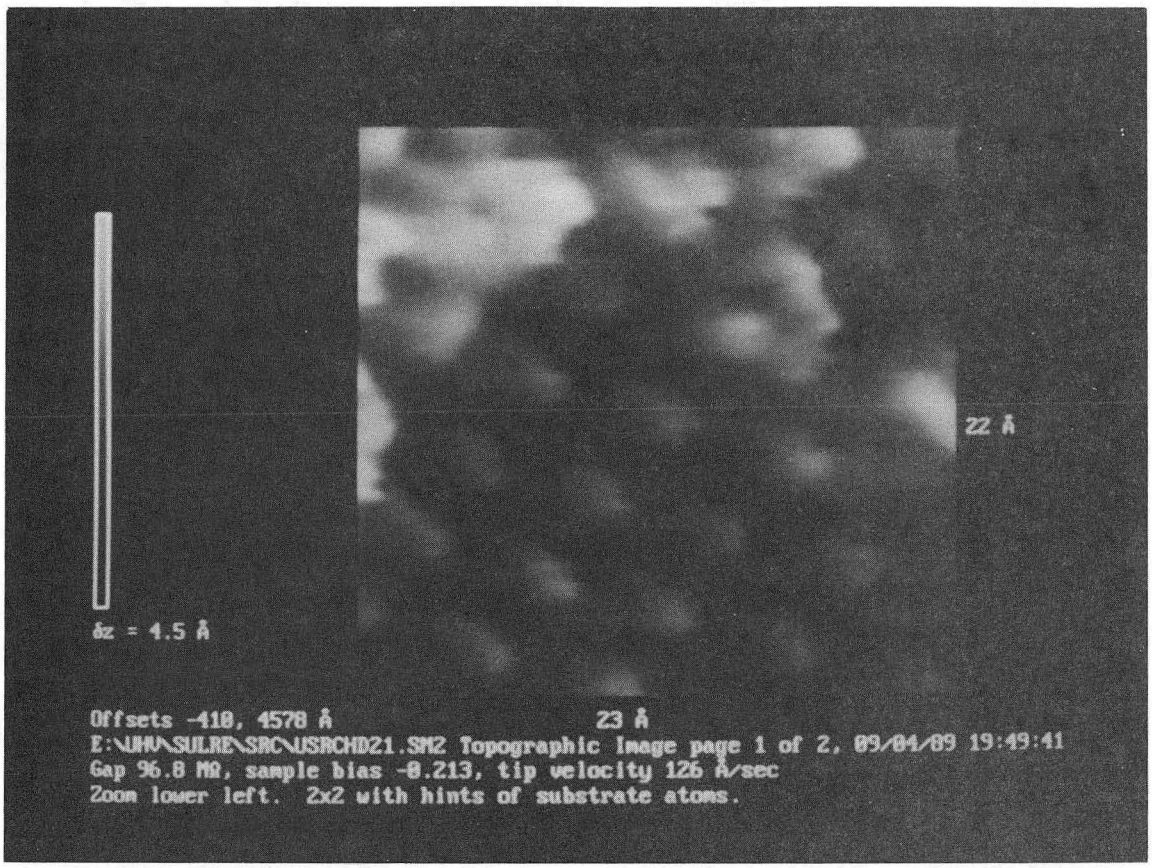

Figure 8.8: Computer graphics magnification of Figure 8.6(c), lower left. Corrugation enhancements in the corner of each p(2×2) unit cell correspond to rhenium atoms without sulfur neighbors (see Fig. 8.7).

BBC 903-2315

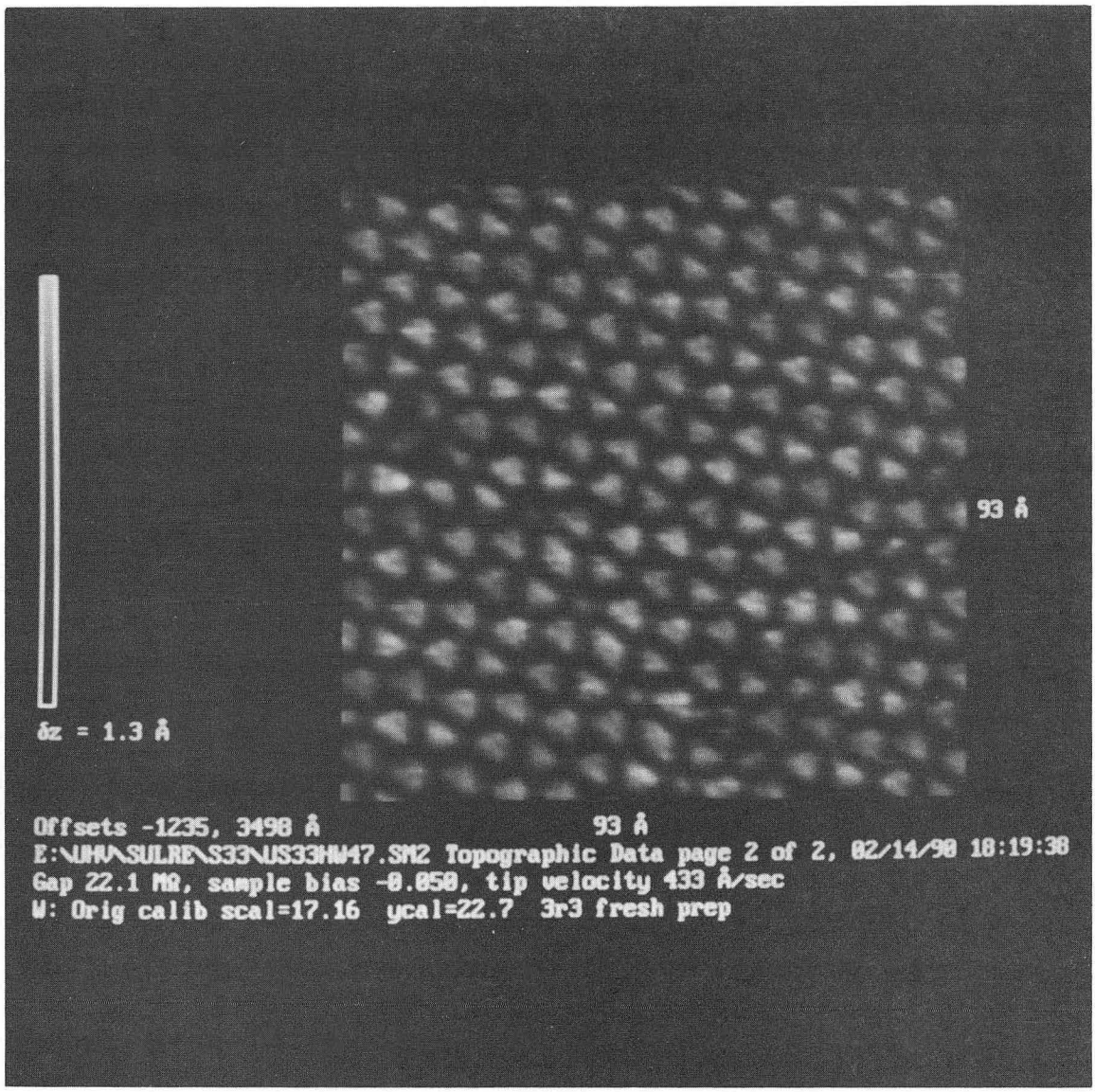

Figure 8.9: (a) $(3\sqrt{3}\times3\sqrt{3})$R30° overlayer on the Re(0001) surface. An anti-phase domain boundary exists, traversing the image from center-bottom to center-left.

BBC 903-2233

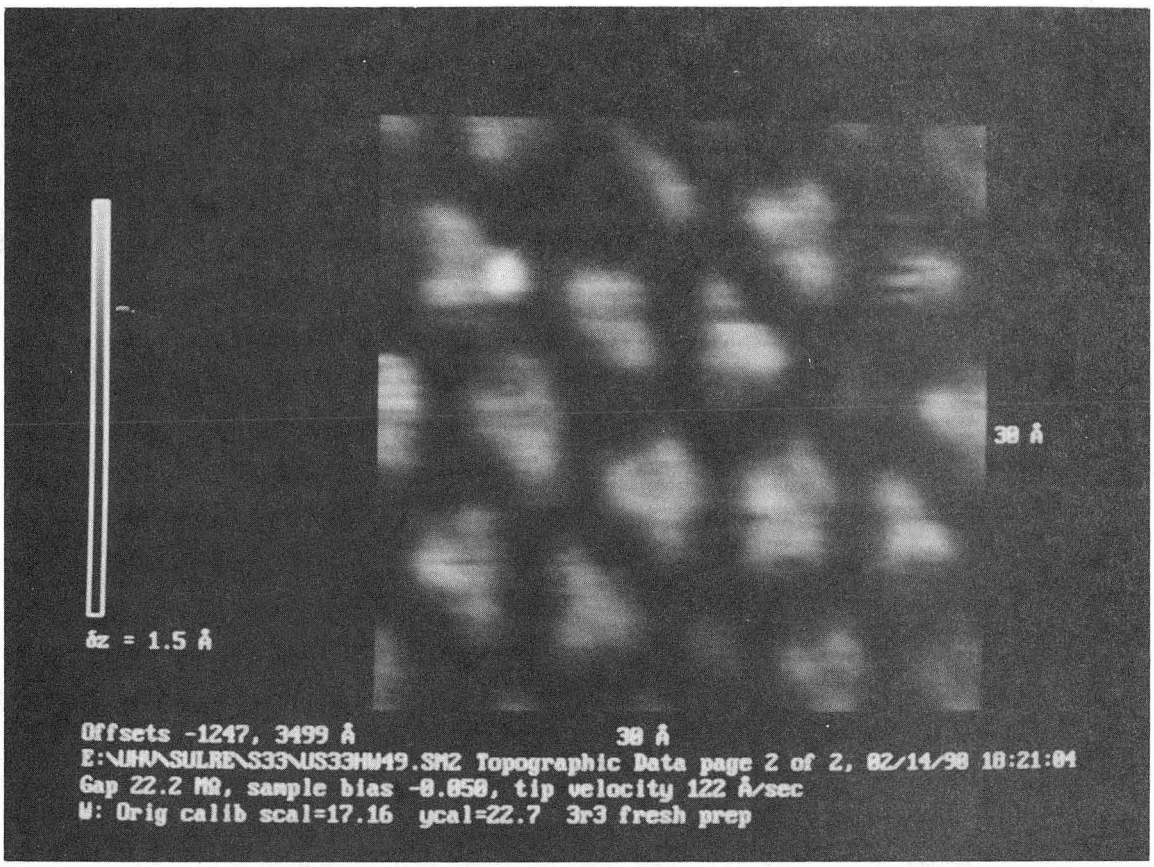

Figure 8.9: (b) High resolution image of the $(3\sqrt{3}\times3\sqrt{3})$R30° overlayer. Single atoms are resolved. Sulfur binds as single atoms, and three- and four-atom clusters.

BBC 903-2343

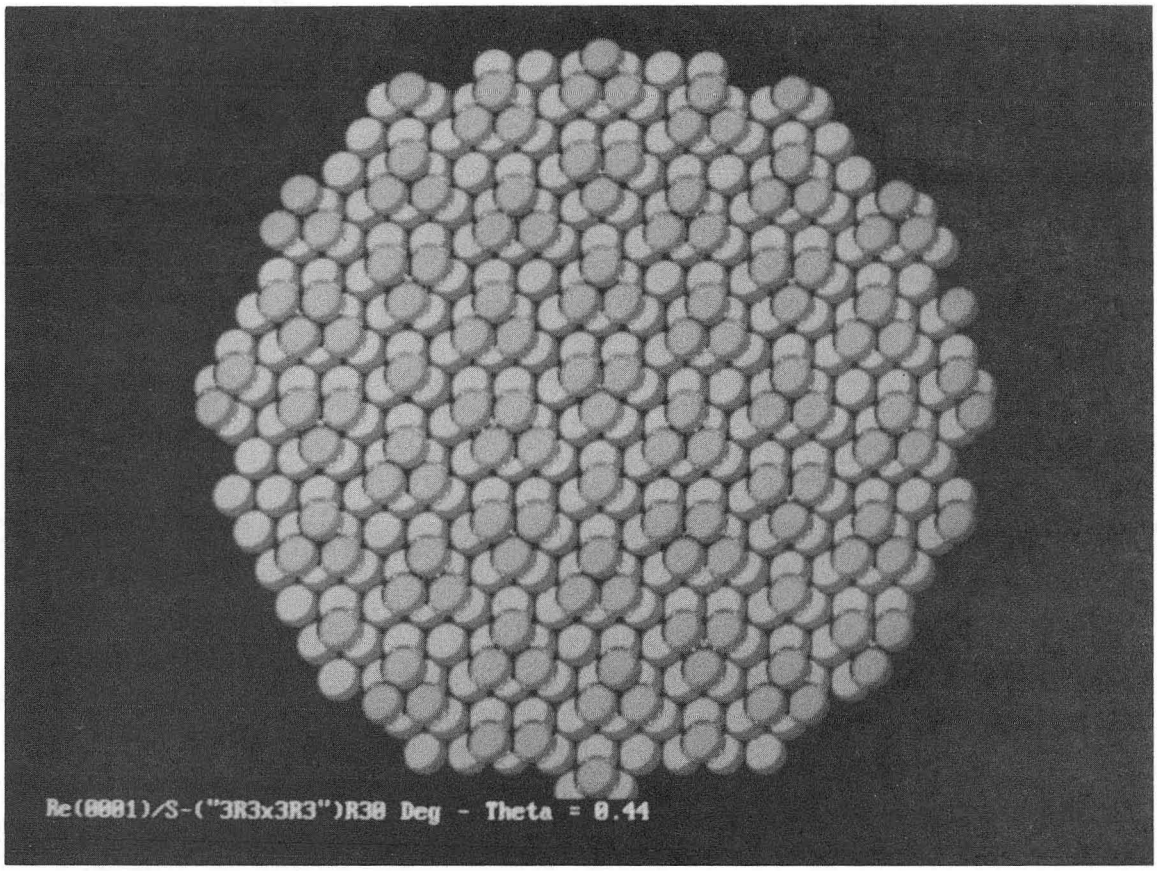

Figure 8.10: Real space model of the Re(0001)/S-($3\sqrt{3}\times3\sqrt{3}$)R30° surface. The anti-phase domain boundary is also shown.

BBC 903-2345

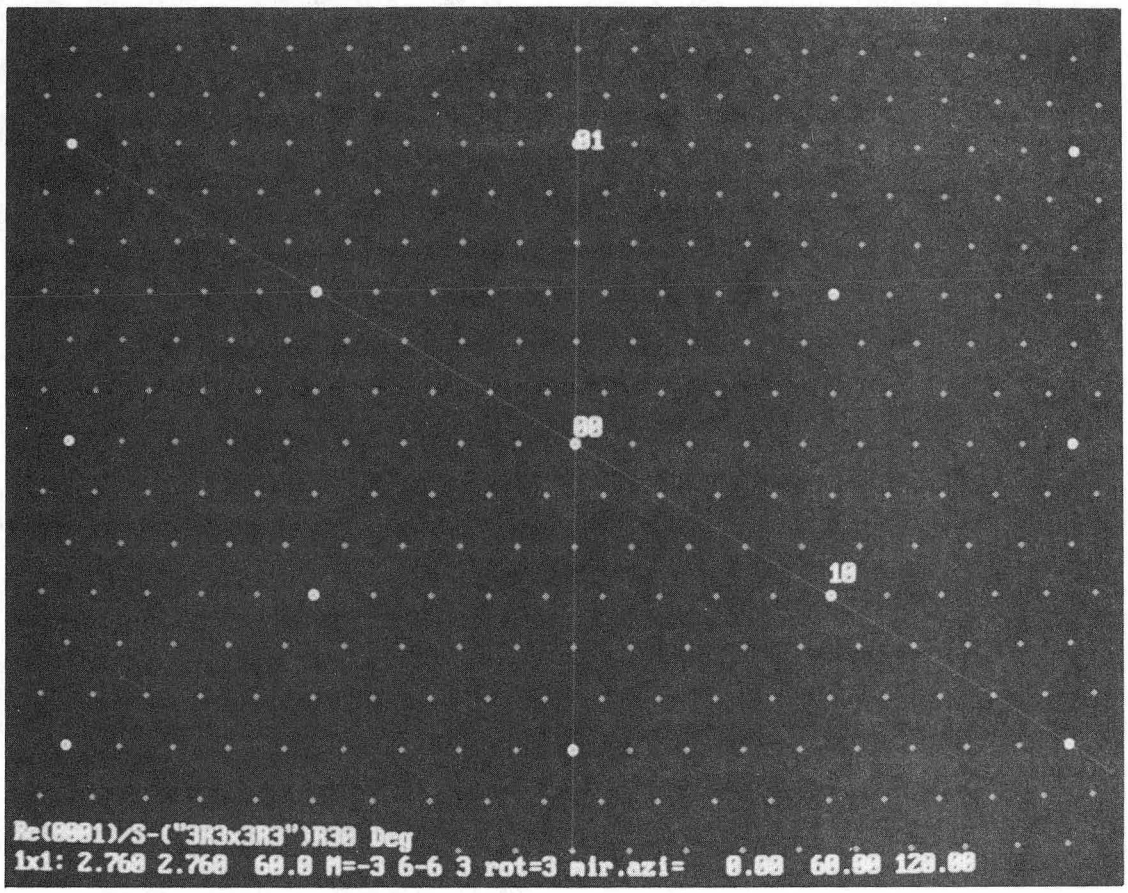

Figure 8.11: Fourier transform, using a single-atom basis, of the $(3\sqrt{3}\times3\sqrt{3})$R30° structure depicted as a LEED pattern.

BBC 904-2749

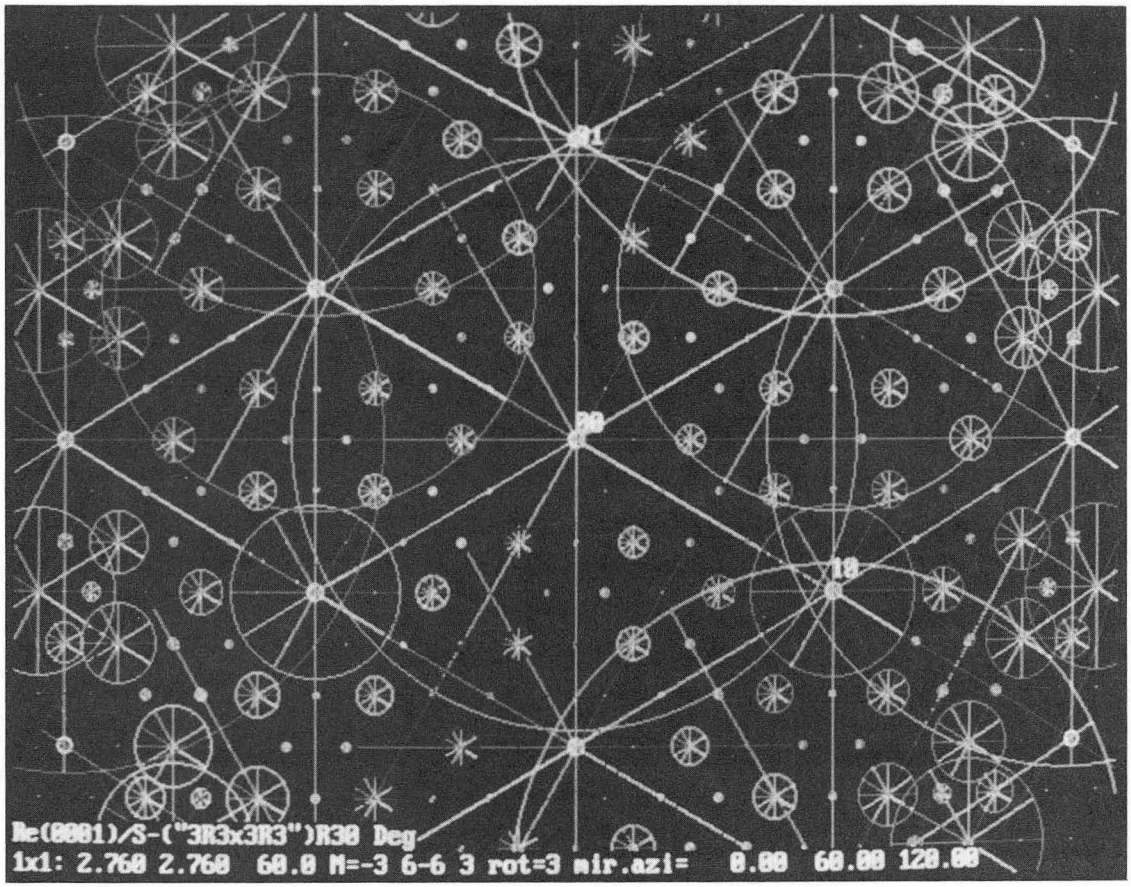

Figure 8.12: Results from a kinematic calculation for the $(3\sqrt{3}\times3\sqrt{3})$R30° overlayer. The circle radius increases with beam intensity. Along the (11) direction, the spot extinctions and intensity reductions are displayed.

BBC 904-2751

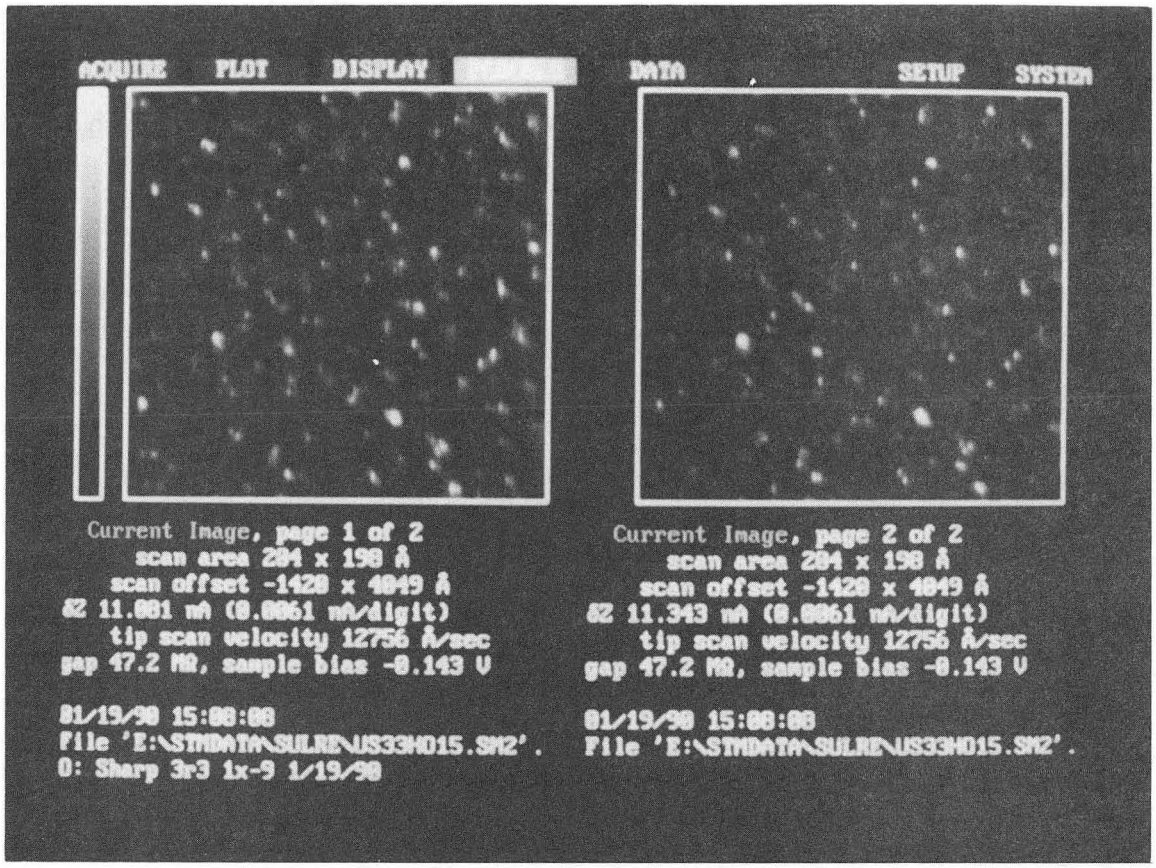

Figure 8.13: Representative image for some areas of a $(3\sqrt{3}\times3\sqrt{3})$R30° overlayer. Formation of some trimers, even at low local coverage is seen. Areas such as this may explain the coverage range measured by AES.

BBC 903-2243

$\begin{bmatrix} 3 & 1 \\ 1 & 3 \end{bmatrix}$ Overlayer

From Figure 8.14 the information on the Re(0001)/S-$\begin{bmatrix} 3 & 1 \\ 1 & 3 \end{bmatrix}$ surface unit cell was obtained. Sulfur tetramers form the lattice basis. The high resolution image in Figure 8.15 resolves the individual atoms in the tetramer. These two images show two of the three rotationally equivalent domains seen with LEED. The STM has been found to be sensitive to the surface LDOS (see Part II). Sensitivity limits have not been well documented, though. The lack of a mirror plane encompassing the substrate first and second layers produces an asymmetry in the surface electronic structure. The corrugation enhancement seen for one atom in the sulfur tetramer again indicates the STM is sensitive to effects created by sub-surface layers (see Section 7.3 in the previous chapter).

A variety of surface structures is also observed for the $\begin{bmatrix} 3 & 1 \\ 1 & 3 \end{bmatrix}$ overlayer. Figure 8.16 presents images and models of these structures. This provides further evidence that the measured AES coverage range is an average of several structures existing simultaneously on the surface.

$(2\sqrt{3}\times2\sqrt{3})$R30° Overlayer

The $(2\sqrt{3}\times2\sqrt{3})$R30° saturation coverage overlayer has been studied previously in air.[16] High resolution images were obtained indicating a three-fold symmetric hexagonal sulfur basis. More effort in this study was directed towards imaging the subsaturation coverage structures. While Figure 8.17 does not indicate three-fold symmetry, it clearly shows the hexagonal sulfur basis of this overlayer. An interesting feature in the image is the horizontal grain boundary. Near the boundary, sulfur cannot form hexagons, and instead packs in small clusters as seen in lower coverage structures.

Summary

- For sulfur adsorbed on the Re(0001) surface two regimes exist. At $\Theta_S \leq 0.25$, isolated atoms are found. At $\Theta_S > 0.25$ sulfur clusters form.

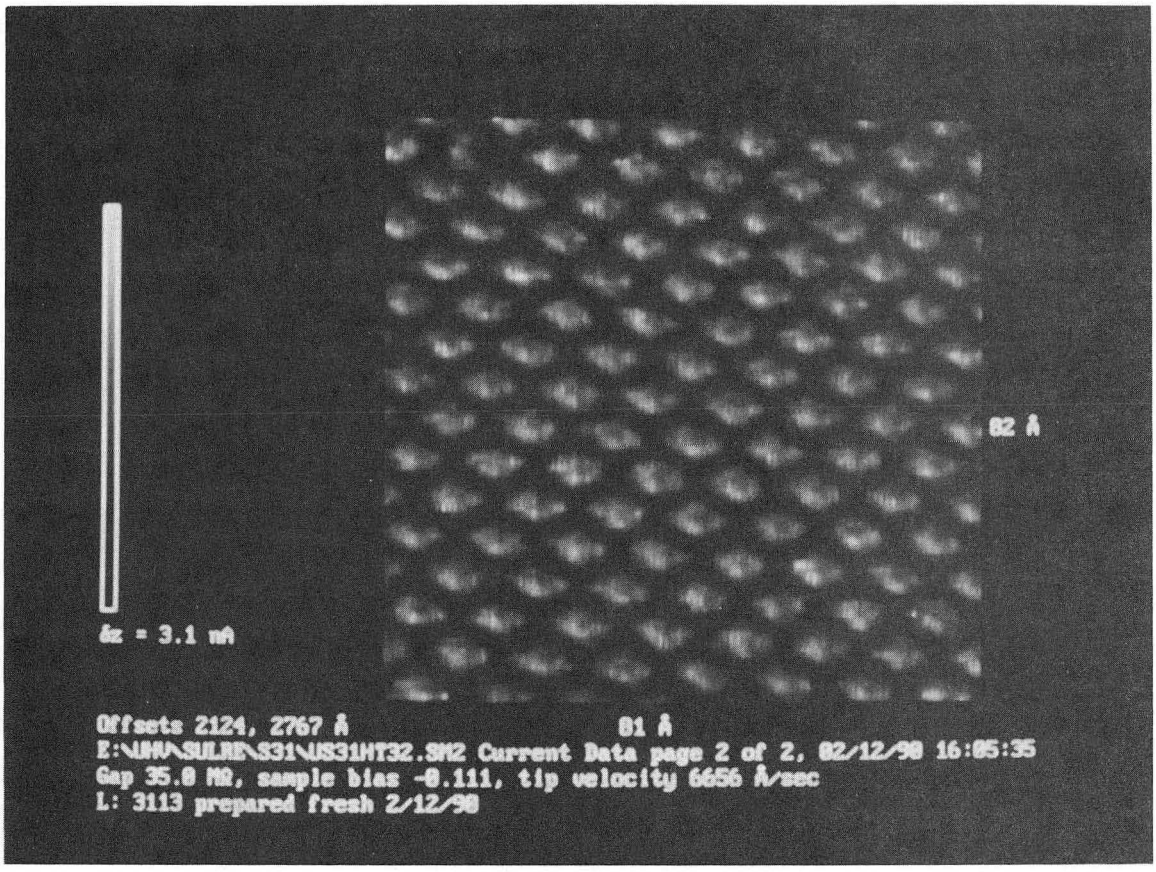

Figure 8.14: $\begin{bmatrix} 3 & 1 \\ 1 & 3 \end{bmatrix}$ overlayer. The unit cell basis is formed by sulfur tetramers.

BBC 903-2339

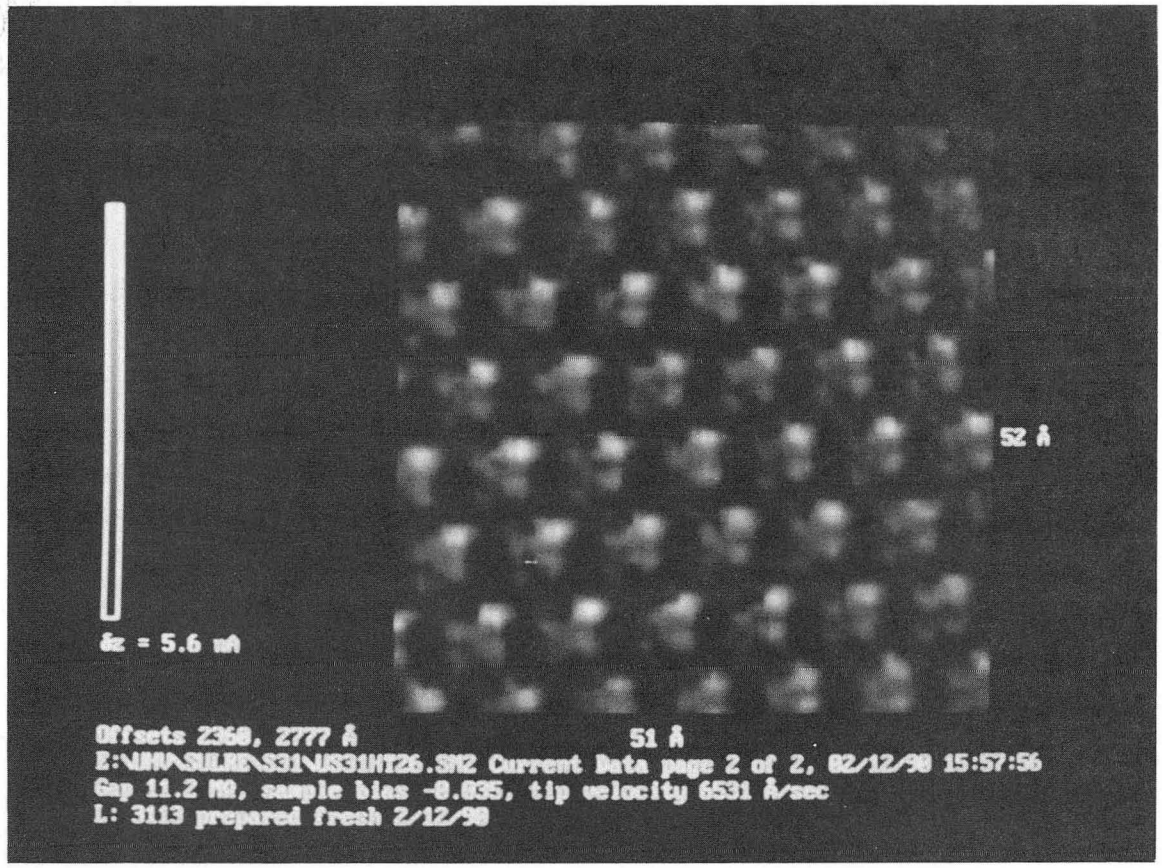

Figure 8.15: (a) High resolution image of the $\begin{bmatrix} 3 & 1 \\ 1 & 3 \end{bmatrix}$ overlayer. The lack of a mirror plane encompassing the substrate first and second layers along the minor tetrameric axis is imaged as a larger corrugation for one sulfur atom. This rotational domain is rotated 60° from the domain imaged in Figure 8.14.

BBC 903-2337

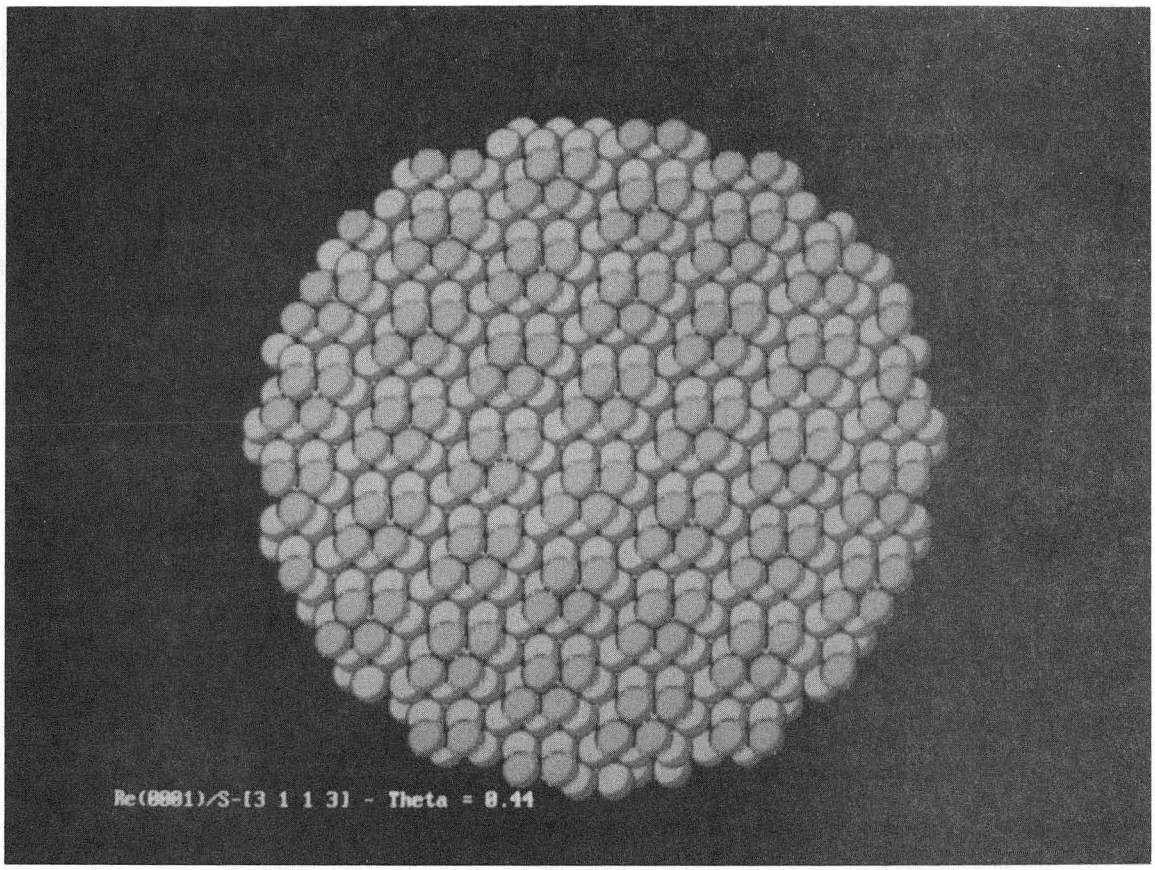

Figure 8.15: (b) Real space model for the Re(0001)/S-$\begin{bmatrix} 3 & 1 \\ 1 & 3 \end{bmatrix}$ system.

BBc 903-2289

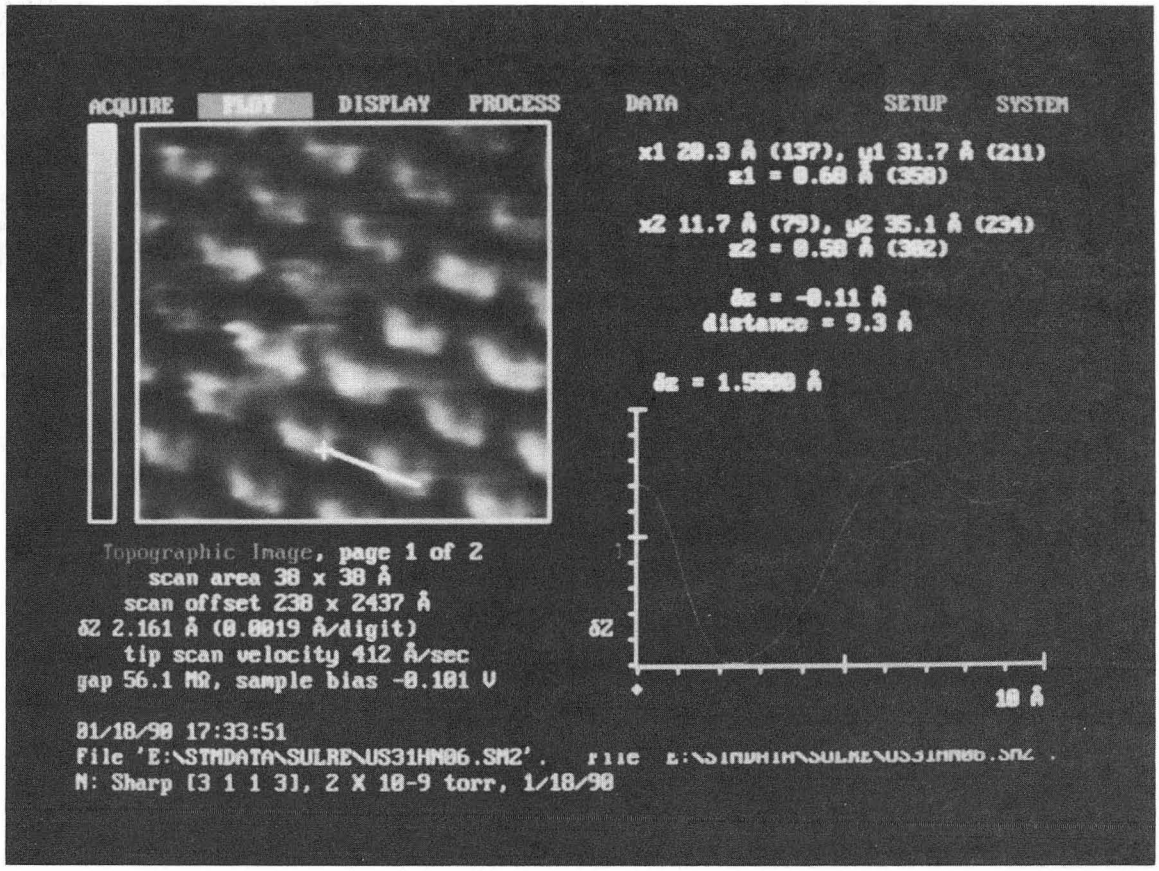

Figure 8.16: (a) Three atom basis for the $\begin{bmatrix} 3 & 1 \\ 1 & 3 \end{bmatrix}$ overlayer.

BBC 903-2253

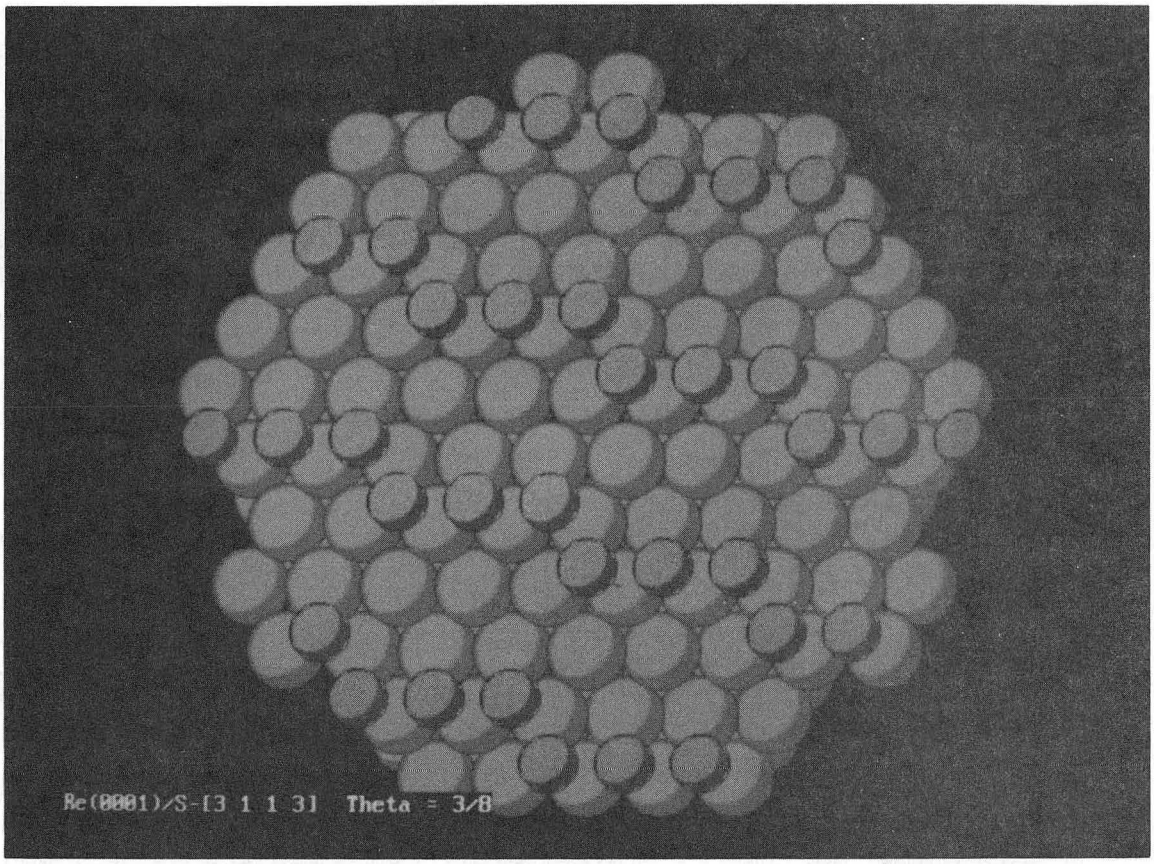

Figure 8.16: (b) Real space model for the three atom basis.

BBC 903-2283

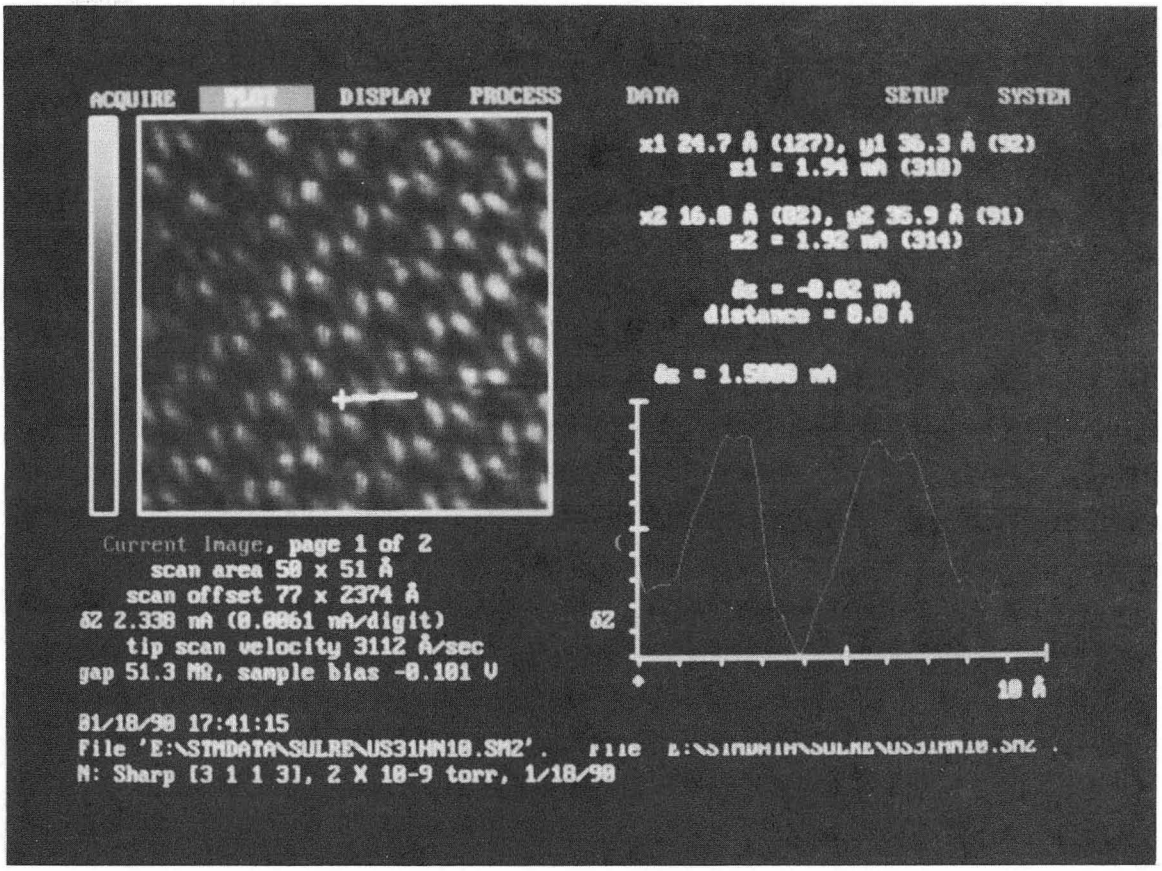

Figure 8.16: (c) Two atom basis for the $\begin{bmatrix} 3 & 1 \\ 1 & 3 \end{bmatrix}$ overlayer.

BBC 903-2261

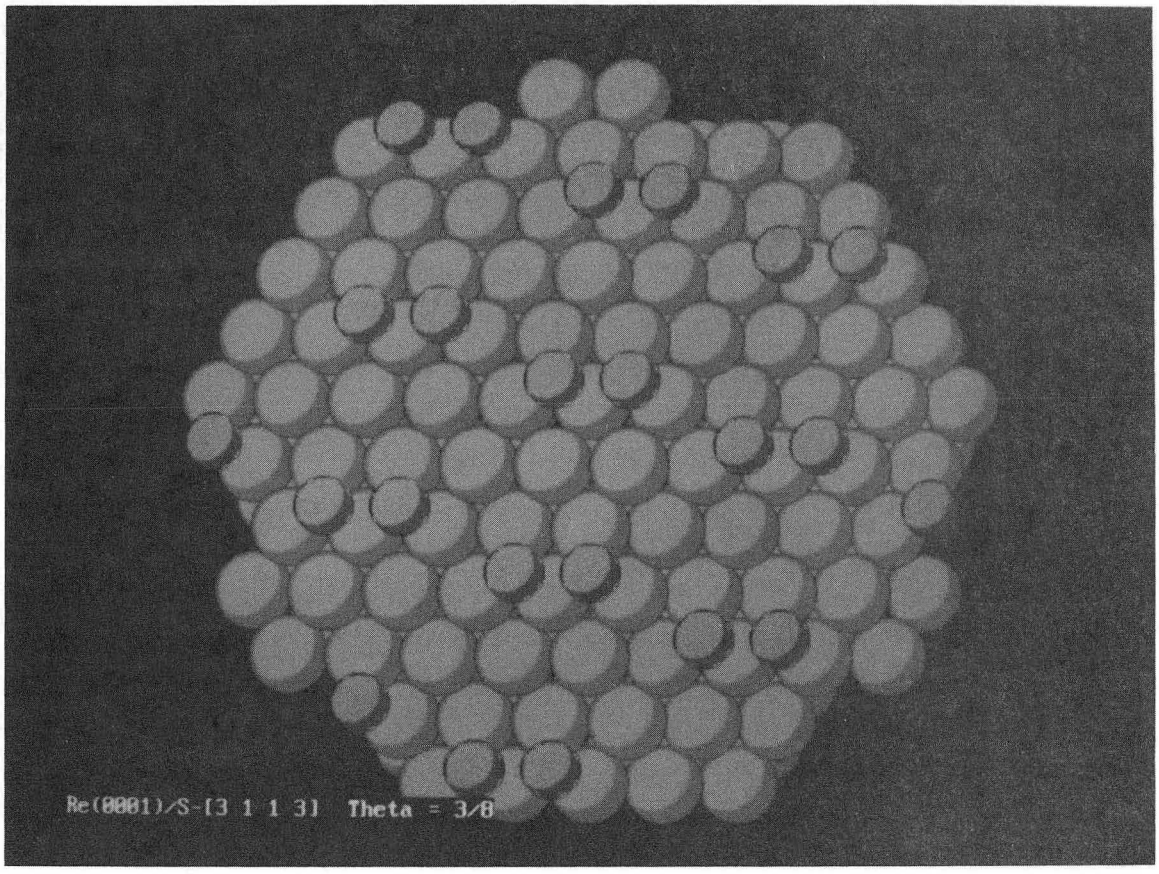

Figure 8.16: (d) Real space model for the two atom basis.

BBC 903-2285

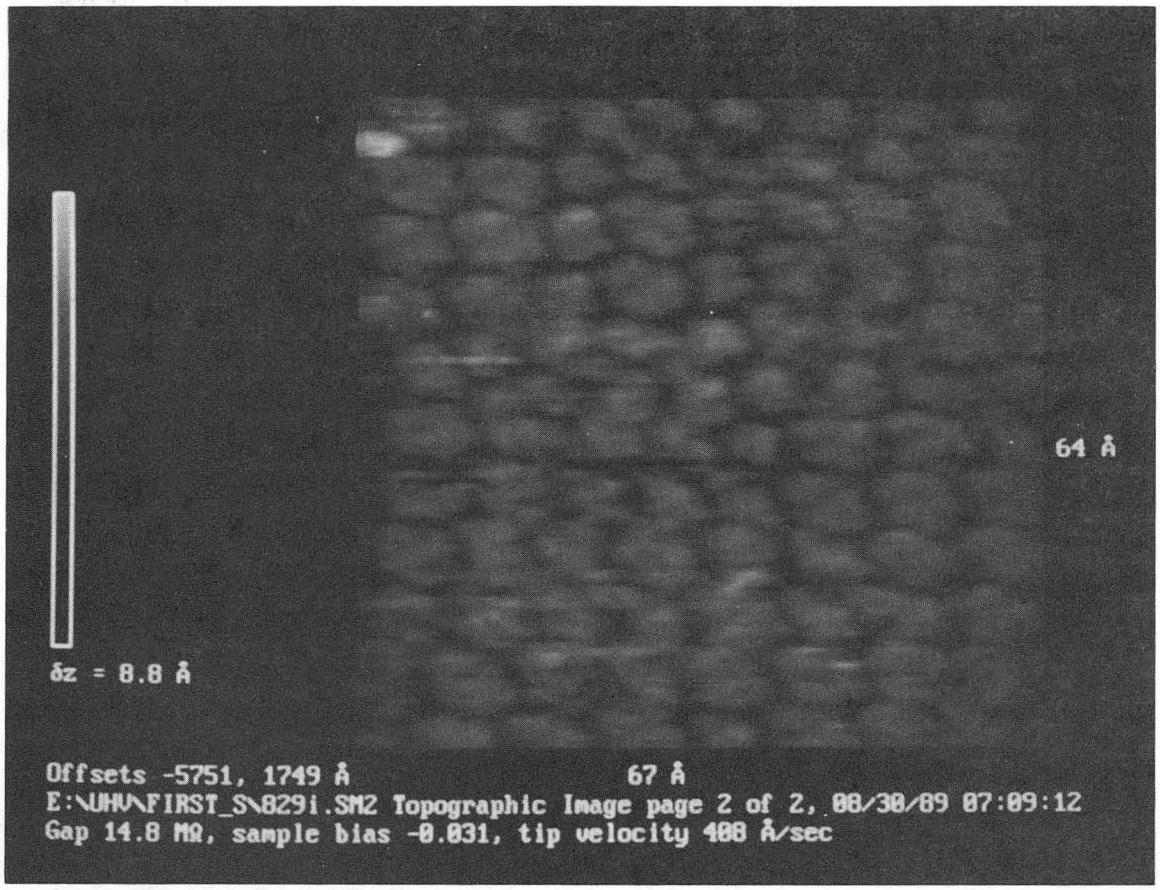

Figure 8.17: (a) Image of the Re(0001)/S-($2\sqrt{3}\times2\sqrt{3}$)R30° surface.

BBC 890-10232

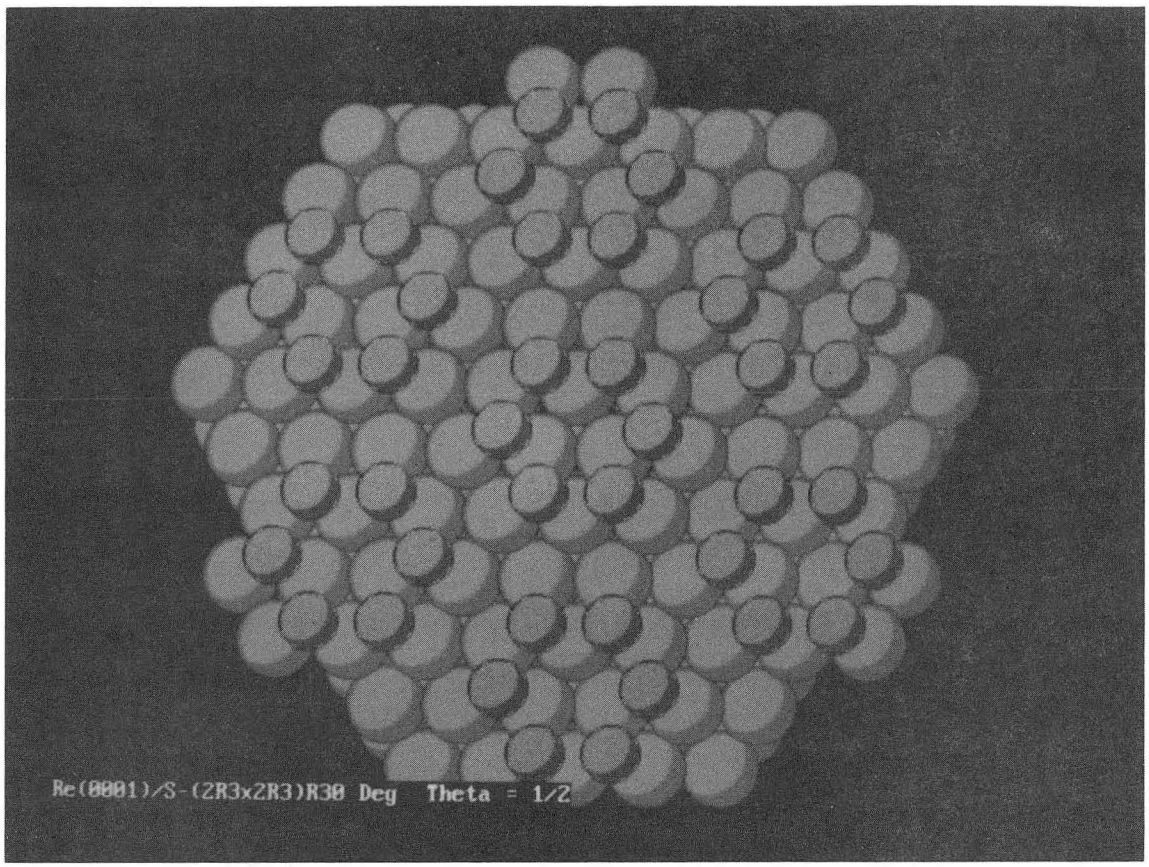

Figure 8.17: (b) Real space model of the Re(0001)/S-($2\sqrt{3}\times2\sqrt{3}$)R30° surface.

BBc 903-2291

- At low coverage, the sulfur overlayer and rhenium substrate are imaged simultaneously. This shows the three-fold adsorption site is favored.

- The stable structures observed by LEED have been imaged. New structures existing in small domains have also been imaged. Presently, only STM observes these surface features directly.

- STM images the overlayer defects, steps and grain boundaries of this chemisorption system.

The STM results for the Re(0001)/S system are given in Table 8.3. The coverages are calculated based on the ideal surface unit cell. Approximate coverage values indicate structures where a range best describes the overlayer. Currently, studies are continuing on this system. Preliminary results indicate the STM can be used to create surface structure changes.[24] These results are not yet well understood, but seem to indicate the STM can be a powerful tool for nanometer scale surface modification, complementing its ability to solve complex surface structures.

[24] *c.f.* E. J. van Loenen, D. Dijkkamp, A. J. Hoeven, J. M. Lenssinck, and J. Dieleman, *Journal of Vacuum Science and Technology A*, vol. 8, p. 574, 1990.

Structure	Coverage
$c(\sqrt{3}\times5)$rect	0.20
$p(2\times2)$	0.25
$(3\sqrt{3}\times3\sqrt{3})R30°$	~0.44
$\begin{bmatrix} 3 & 1 \\ 1 & 3 \end{bmatrix}$	~0.47
$(2\sqrt{3}\times2\sqrt{3})R30°$	0.50

Table 8.3: Summary of STM results for the Re(0001)/S chemisorption system.

Appendix A

Design Sketches for the Ultra-High Vacuum Scanning Tunneling Microscopy System.

AA: 0.250 wide slots are 0.050 deep. Holes are countersunk 4-40 (slot & top both sides)

1 of 2

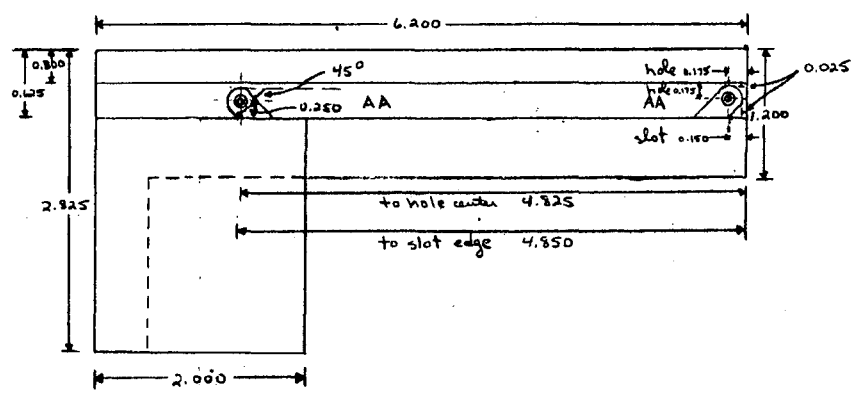

SIDE VIEW

viton thickness
0.060

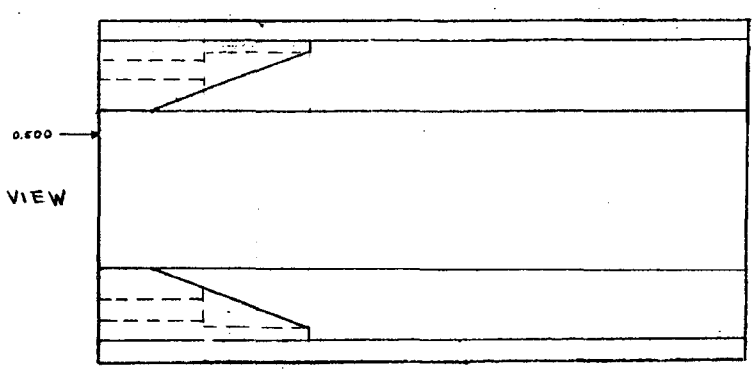

BOTTOM VIEW

304 SS

SUSPENSION SUPPORT

UHV TUBE STM

8/23/88
D. Zaglinski

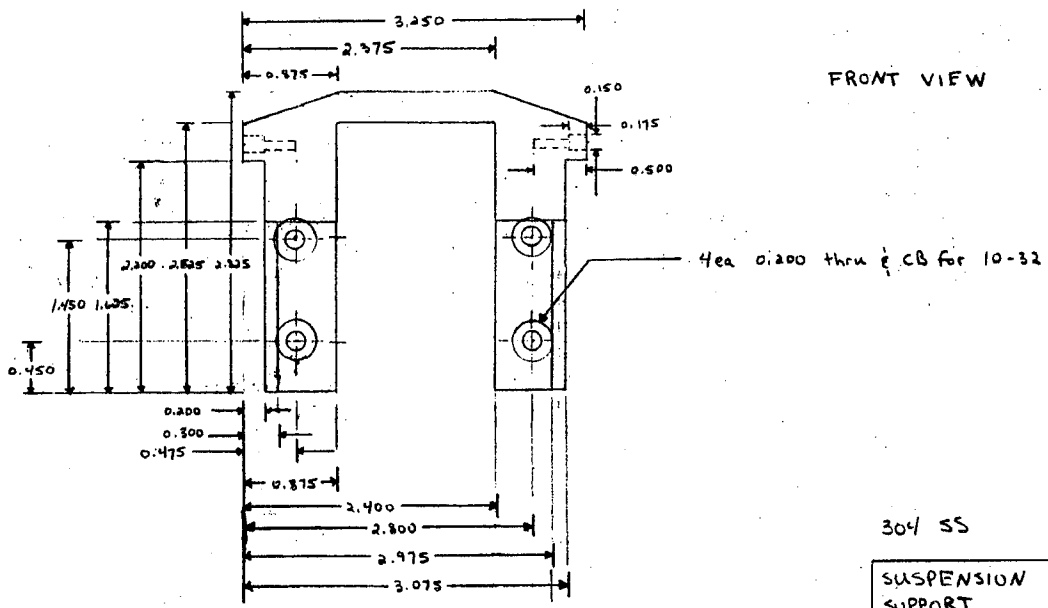

FRONT VIEW

304 SS

SUSPENSION SUPPORT

UHV TUBE STM

8/23/88
D. Zeglinski

1 ea.

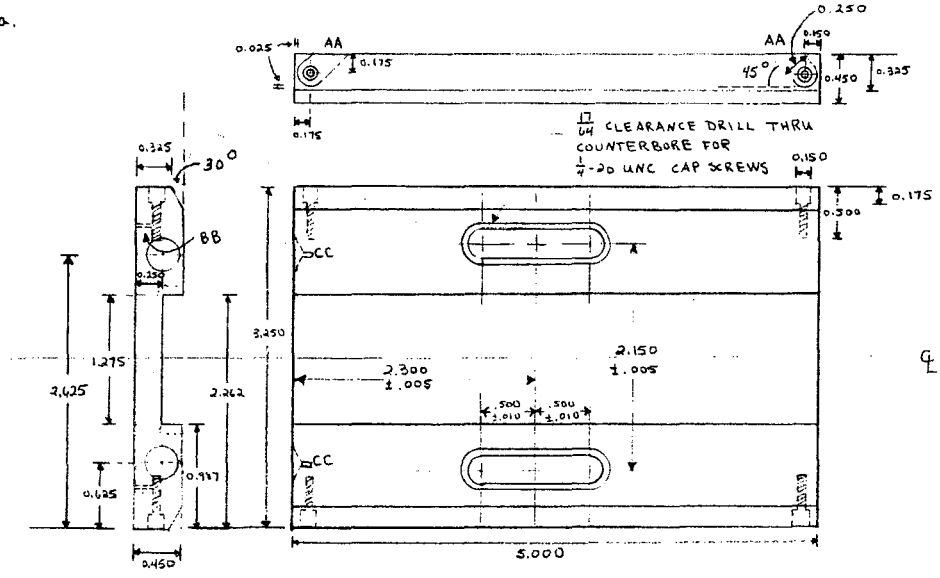

SS washer 8 ea.

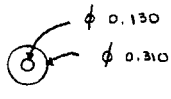

0.025 TH

SS 4-40 Socket Head Screw 8 ea

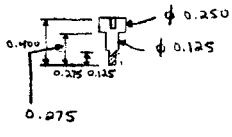

AA: 0.250 wide slots are 0.050 deep. Holes are countersunk 4-40 (slot & tap both edges)

BB: provide 1/16 pump out hole for each 4-40 tapped hole

CC: 120° countersink to 0.100 depth one edge only

REVISION A : COUNTERBORED 1/4-20 CLEARANCE SLOTS

BASEPLATE
UHV TUBE STM

304 SS
REVISION A
8/16/88
D. Zeglinski

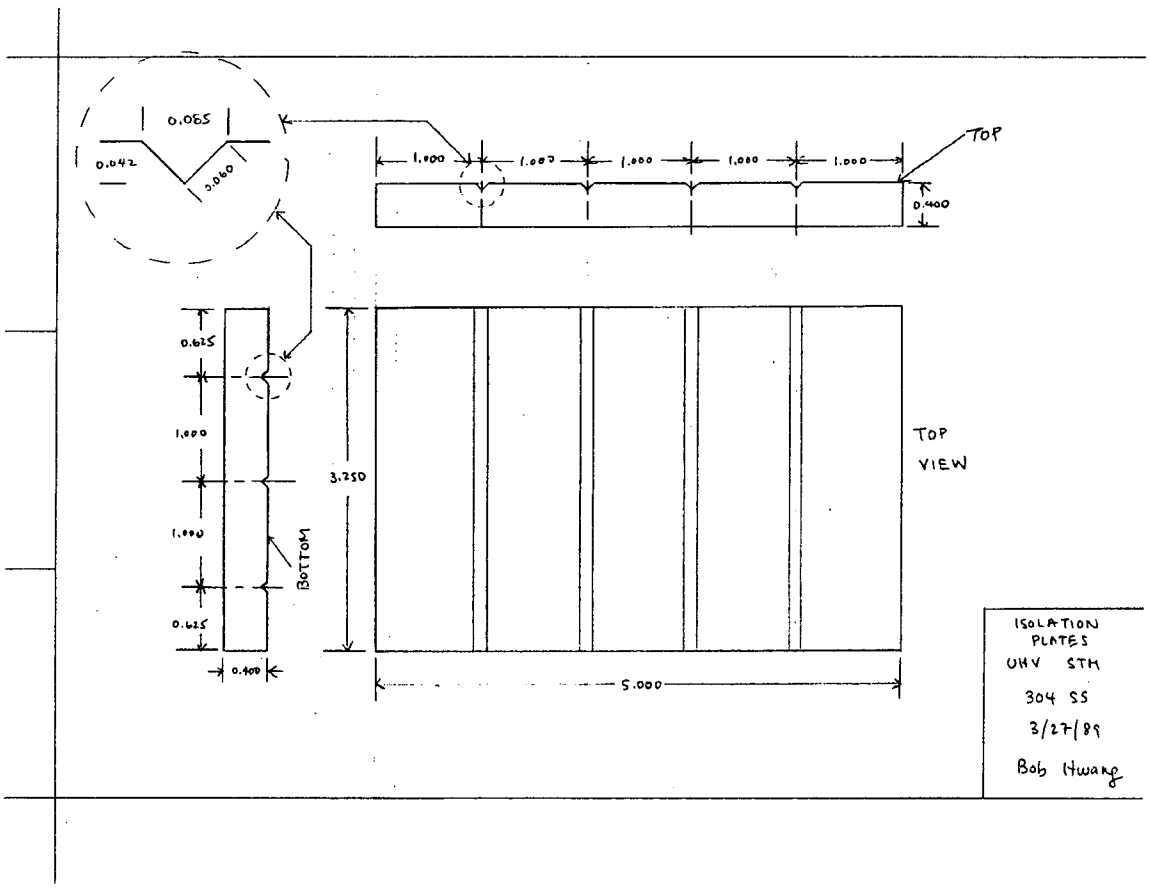
0.065
0.042
0.060
1.000
1.000
1.000
1.000
1.000
TOP
0.4400
0.625
1.000
1.000
0.625
0.400
BOTTOM
3.250
5.000
TOP
VIEW
ISOLATION
PLATES
UHV STM
304 SS
3/27/89
Bob Hwang

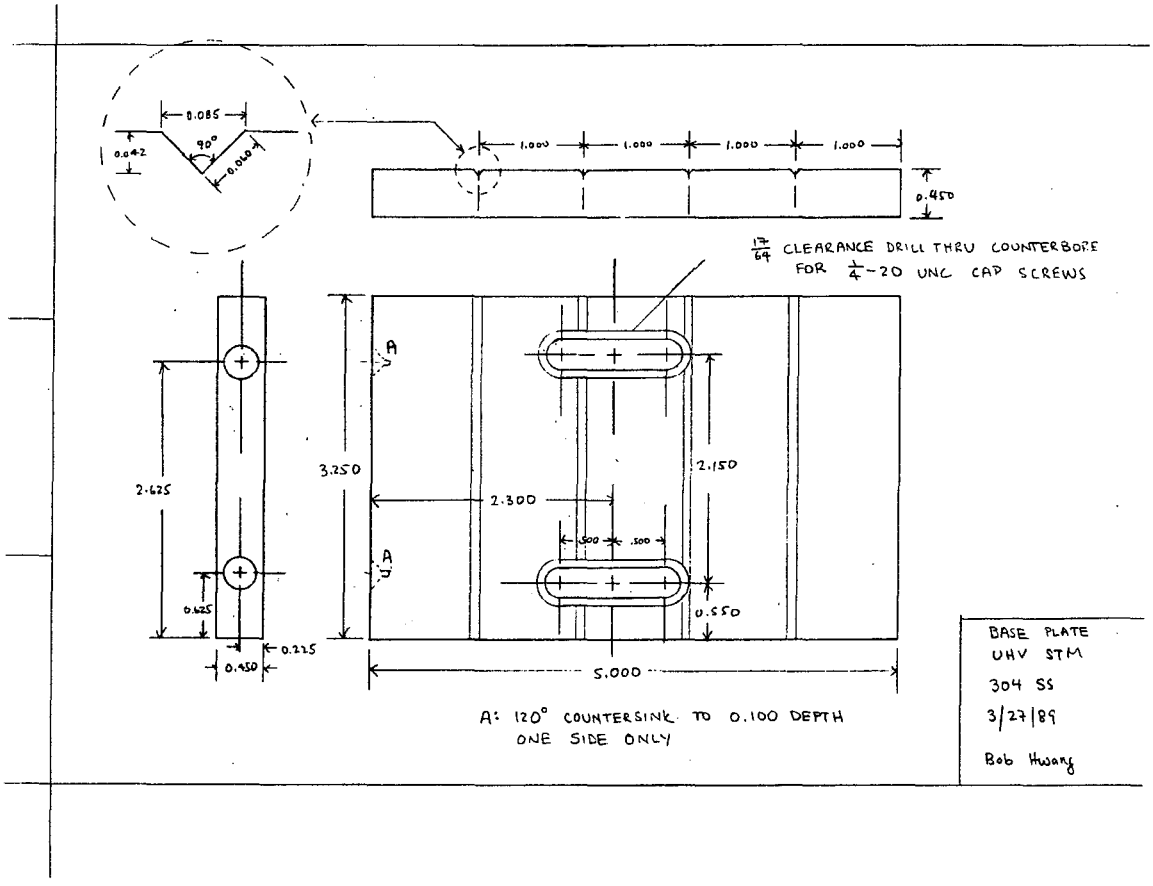
0.085
90°
0.042
0.060
1.000
1.000
1.000
1.000
0.450
17/64 CLEARANCE DRILL THRU COUNTERBORE
FOR 1/4-20 UNC CAP SCREWS
A
A
2.625
3.250
2.300
2.150
.500
.500
0.625
0.550
0.225
0.450
5.000
A: 120° COUNTERSINK TO 0.100 DEPTH
ONE SIDE ONLY
BASE PLATE
UHV STM
304 SS
3/27/89
Bob Hwang

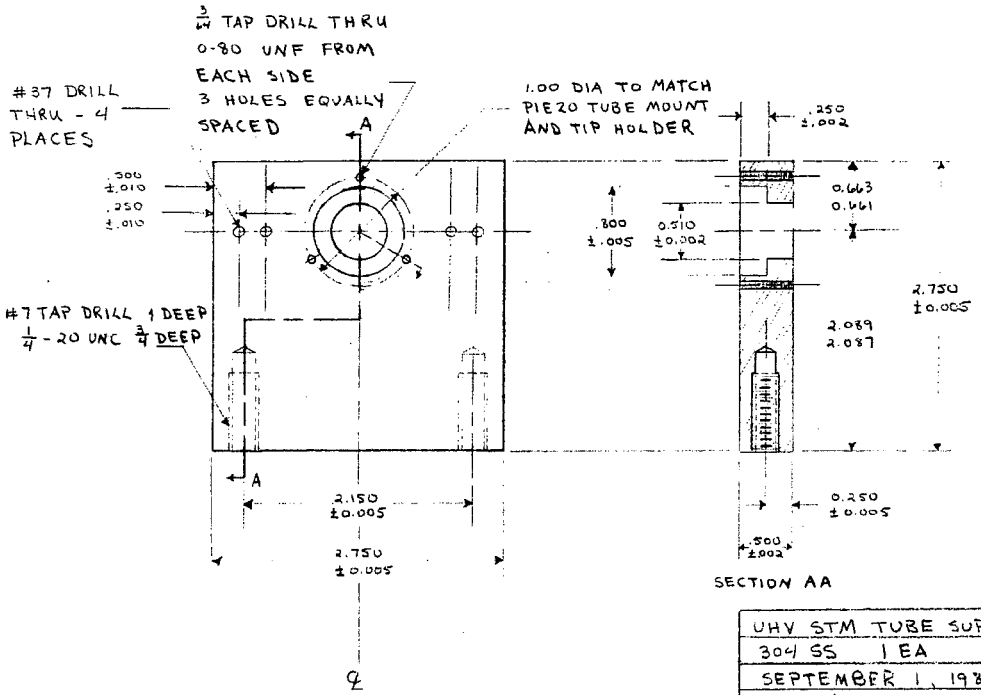

UHV STM TUBE SUPPORT PLATE	
304 SS	1 EA
SEPTEMBER 1, 1988	
D. Zeglinski	
9/28/88 Revision B : Thru-holes	

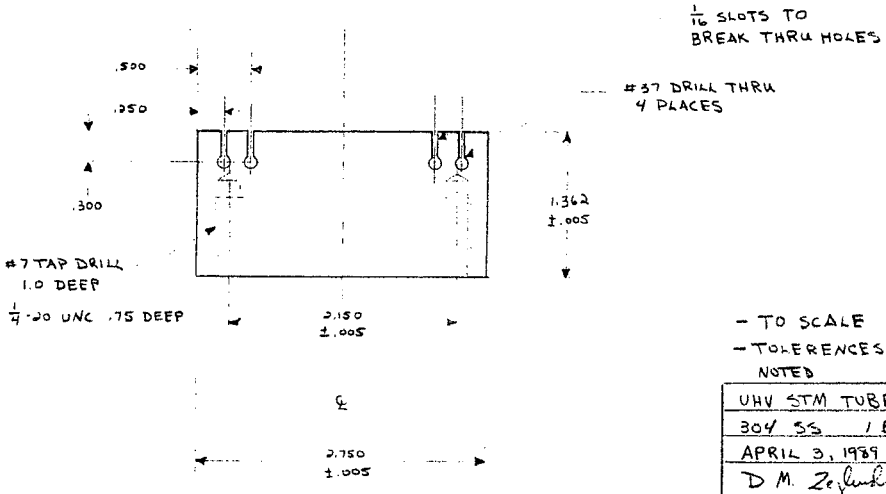

- TO SCALE
- TOLERENCES ±.010 EXCEPT WHERE NOTED

UHV STM TUBE SUPPORT PLATE
304 SS 1 EA
APRIL 3, 1989
D M. Zeglinski

Note: only shown are changes to be machined on part provided

SCALE X2

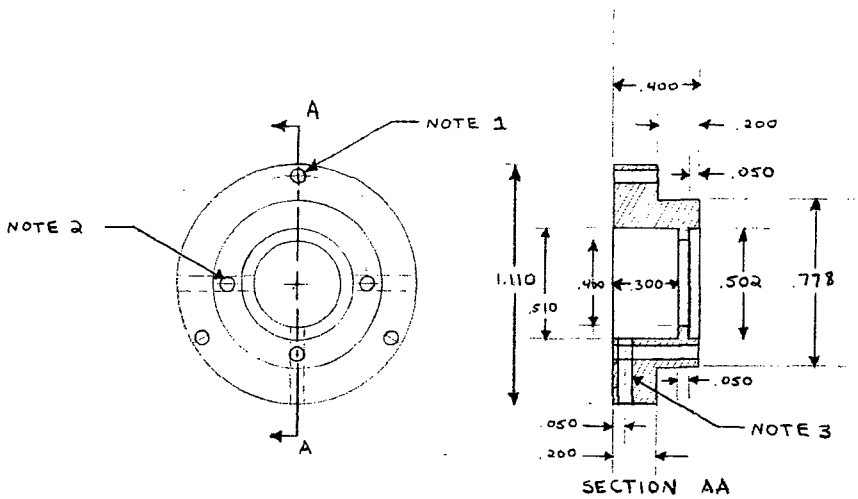

±0.005

NOTE 1: DRILL ASSEMBLED WITH PART B - #53 THRU-DRILL - 3 PLACES ON 1.000 BC @ 120°

NOTE 2: DRILL THRU - $\frac{1}{16}$ DRILL - 3 PLACES ON 0.640 BC @ 90°

NOTE 3: DRILL THRU 0.050 ℄ FROM EDGE @ 90° - $\frac{1}{16}$ DRILL INTERSECTING WITH THRU-HOLE DESCRIBED IN NOTE 2

PIEZO TUBE MOUNT
PART A

VESPEL
UHV TUBE STM
7/11/89
D.M. Zeglinski

SCALE X2

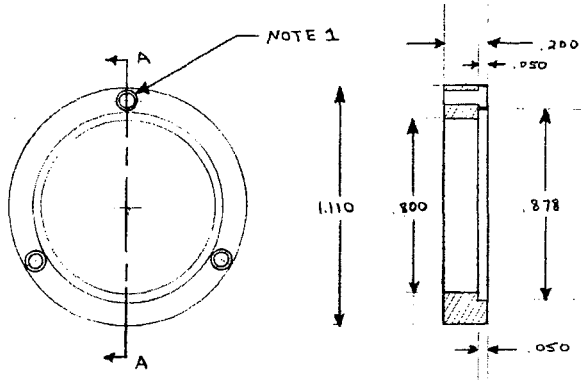

COUNTERBORE THIS SIDE

± 0.005

NOTE 1 : DRILL & CBORE ASSEMBLED WITH PART A - 0-80 UNF RH SCREWS - 3 PLACES ON 1.000 BC @ 120°

ASSEMBLE SO THAT BOTTOM OF PART B MATES WITH TOP OF PART A

PIEZO TUBE MOUNT
PART B

VESPEL
UHV TUBE STM
7/11/89
D M. Zaleski

1 ea.

SCALE X 2

0.500"

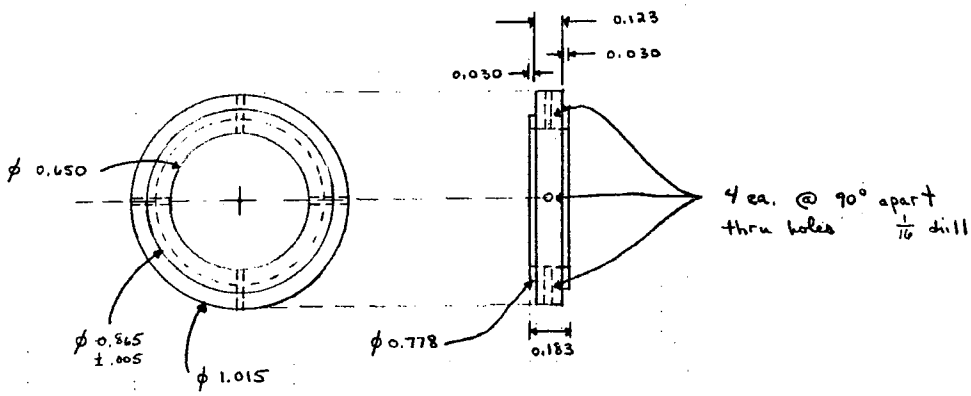

VESPEL

PIEZO TUBE / QUARTZ TUBE COUPLER

UHV TUBE STM

8/22/88
D. Zeglinski

TIP HOLDER

VESPEL
UHV TUBE STM
7/18/89

D. M. Zeglinski

SCALE X4

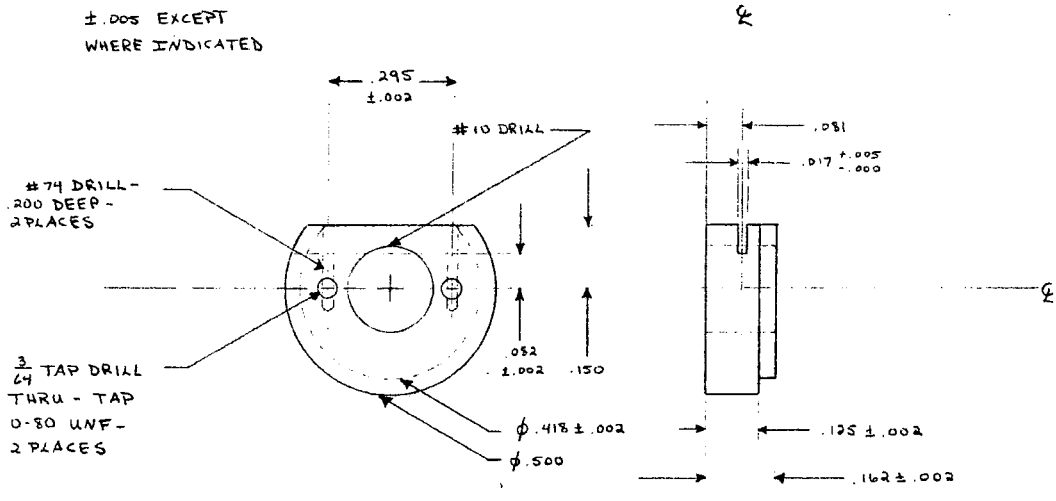

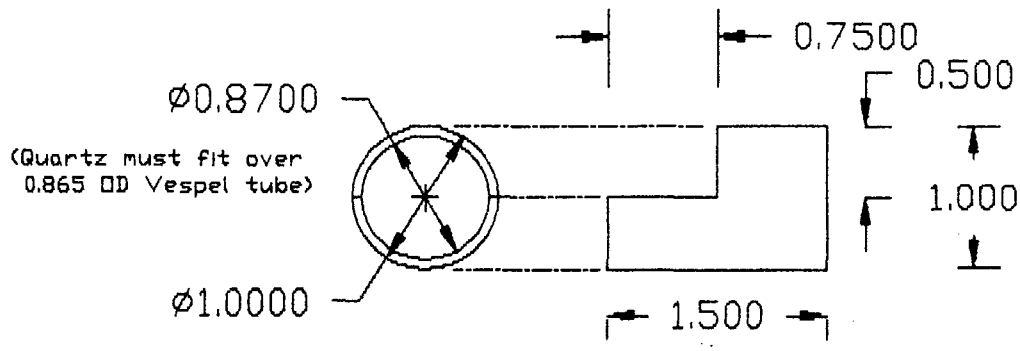

Material: Quartz

Tolerance: 0.005

Scale 1X

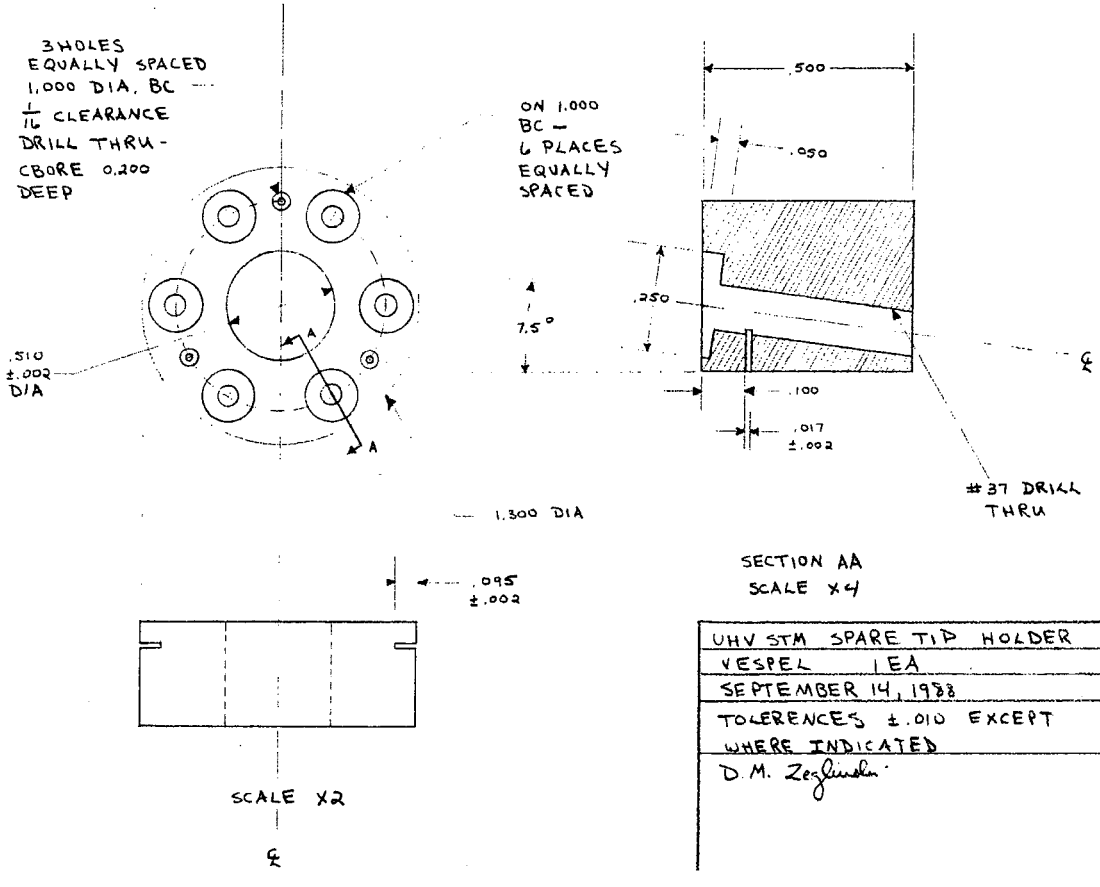
3 HOLES
EQUALLY SPACED
1.000 DIA. BC
1/16 CLEARANCE
DRILL THRU -
CBORE 0.200
DEEP
ON 1.000
BC -
6 PLACES
EQUALLY
SPACED
.500
.050
.250
7.5°
.510
±.002
DIA
A
A
.100
.017
±.002
#37 DRILL
THRU
1.300 DIA
.095
±.002
SCALE X2
SECTION AA
SCALE X4
UHV STM SPARE TIP HOLDER
VESPEL 1 EA
SEPTEMBER 14, 1988
TOLERENCES ±.010 EXCEPT
WHERE INDICATED
D.M. Zeglinski

SCALE 4X

10 EA

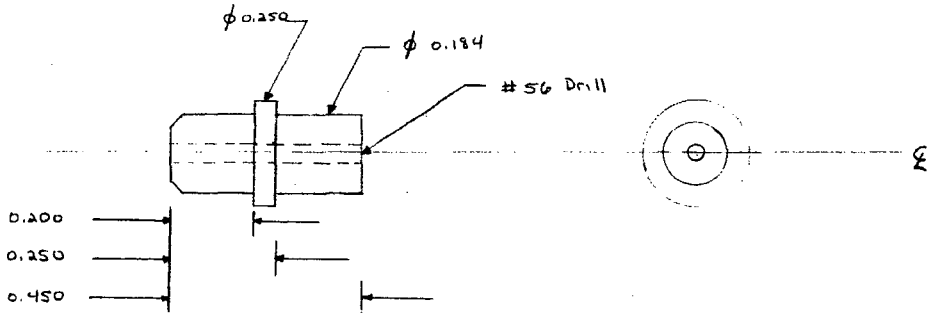

TIP HOLDER

UHV TUBE STM
ALUMINUM
8/24/88

D. Zoglmeier

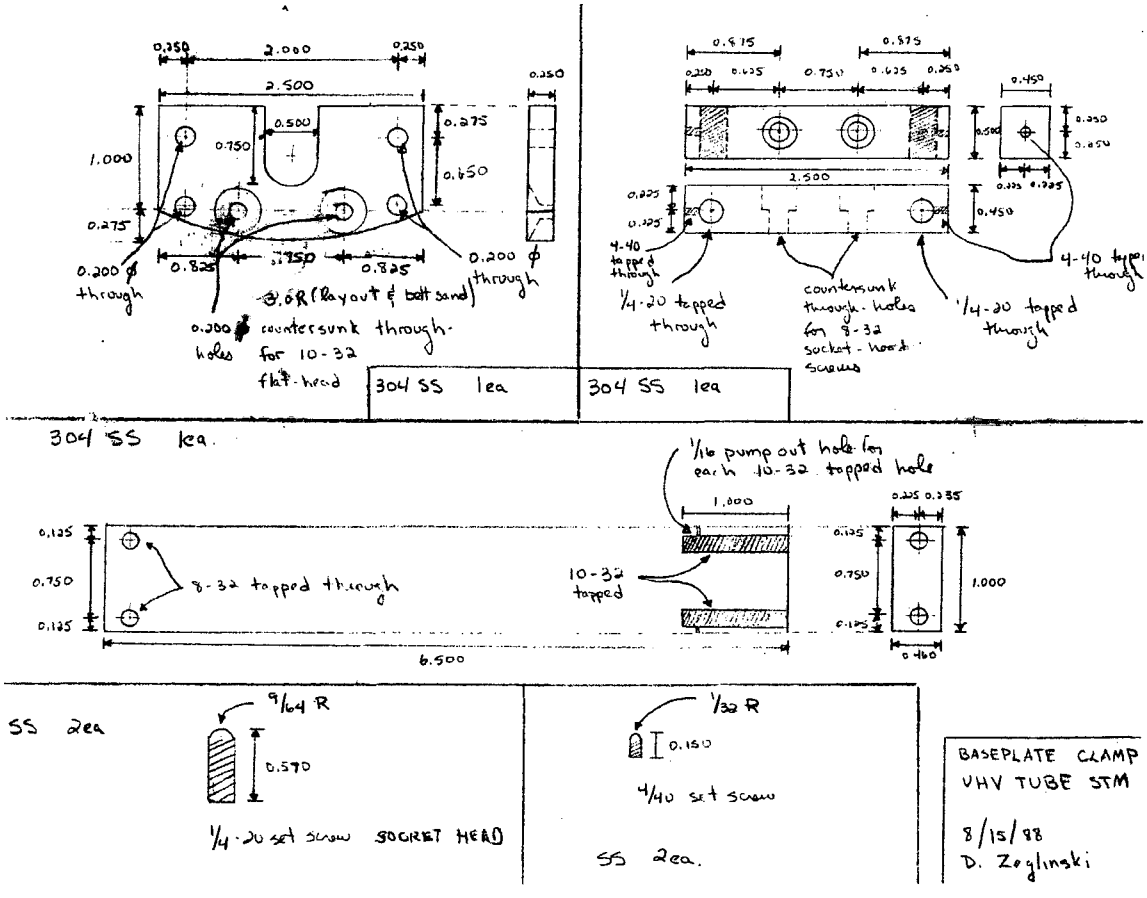
0.250
2.000
0.250
2.500
0.500
0.750
1.000
0.275
0.650
0.250
0.275
0.825
0.750
0.825
0.200 ϕ through
0.200 ϕ through
0.0R (layout & batt sand)
0.200 ϕ countersunk through-holes for 10-32 flat-head
304 SS 1ea
0.875
0.875
0.250
0.625
0.750
0.625
0.250
0.450
0.250
0.250
0.500
2.500
0.225
0.225
0.450
0.225
0.225
4-40 tapped through
1/4-20 tapped through
countersunk through-holes for 8-32 socket-head screws
1/4-20 tapped through
4-40 tapped through
304 SS 1ea
304 SS 1ea.
1/16 pump out hole for each 10-32 tapped hole
1.000
0.225
0.225
0.125
0.750
0.125
8-32 tapped through
10-32 tapped
0.125
0.750
0.125
1.000
6.500
0.460
SS 2ea
9/64 R
0.570
1/4-20 set screw SOCKET HEAD
1/32 R
0.150
4/40 set screw
SS 2ea.
BASEPLATE CLAMP
UHV TUBE STM
8/15/88
D. Zoglinski

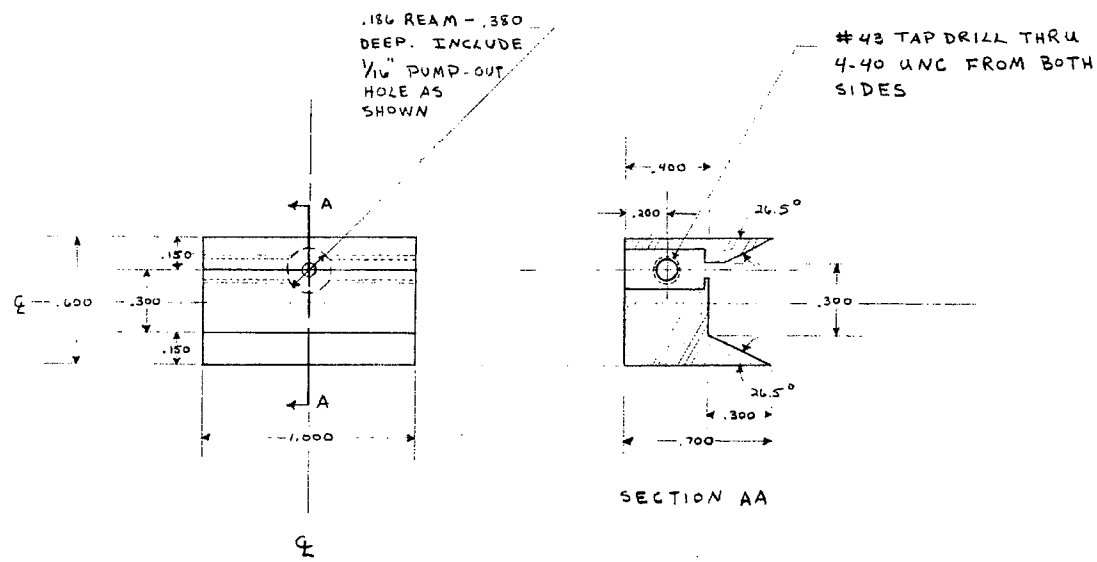

SCALE X2

UHV STM CLAMP LOCATOR
304 SS 1 EA
OCTOBER 6, 1988
DIMENSIONS ±0.010 EXCEPT AS INDICATED
D. M. Zezlinski

SCALE X2

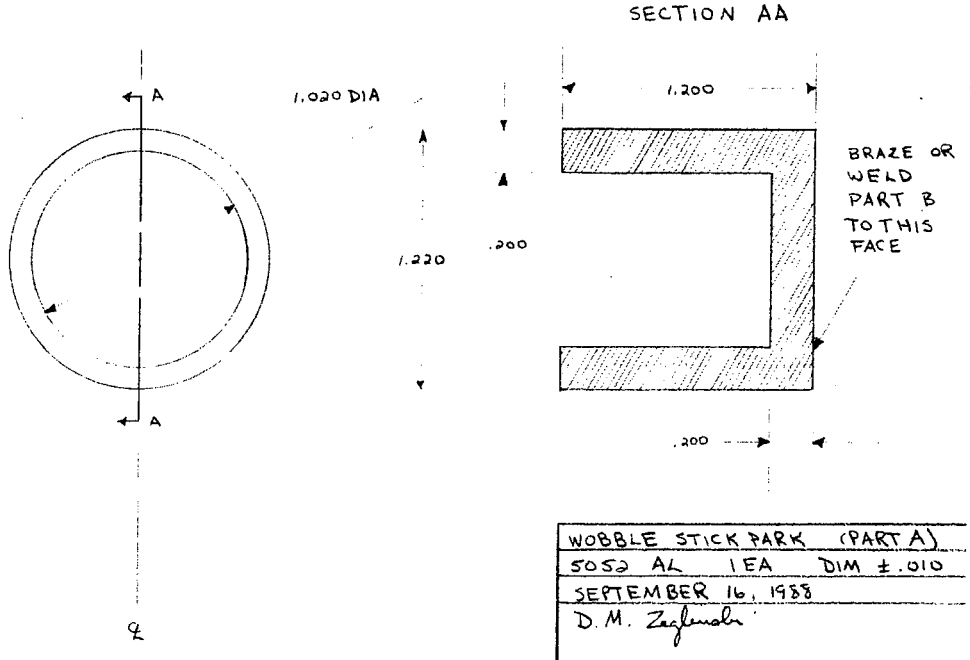

WOBBLE STICK PARK (PART A)		
5052 AL	1 EA	DIM ±.010
SEPTEMBER 16, 1988		
D. M. Zaglmaier		

TO SCALE

WOBBLE STICK PARK (PART B)
0.190 THICK 5052 AL CBL # 9501-11513
FEBRUARY 16, 1989
D. M. ZEGLINSKI
ALL TOLERANCES ±.010

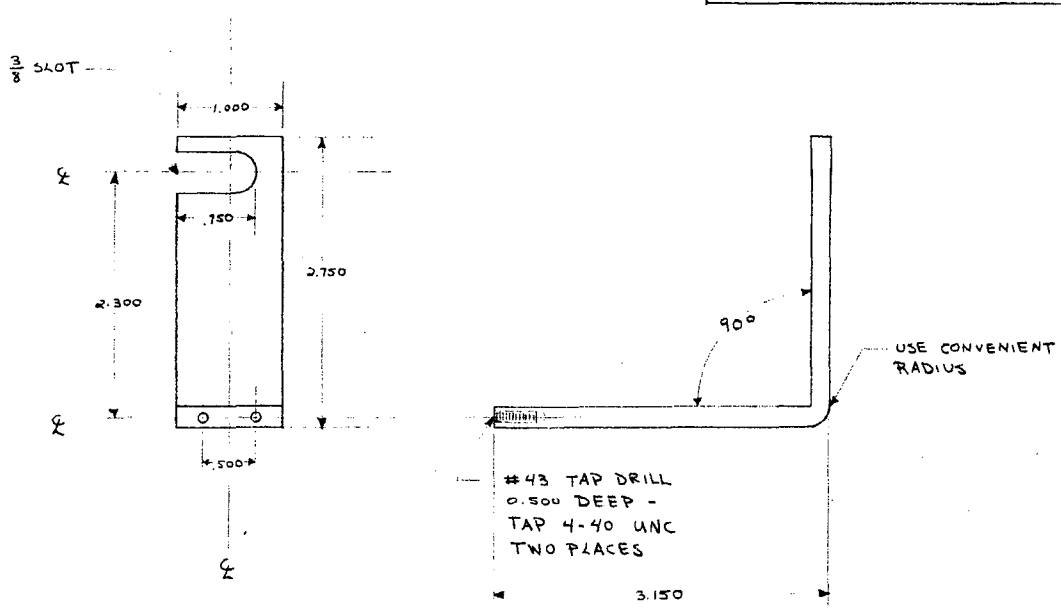

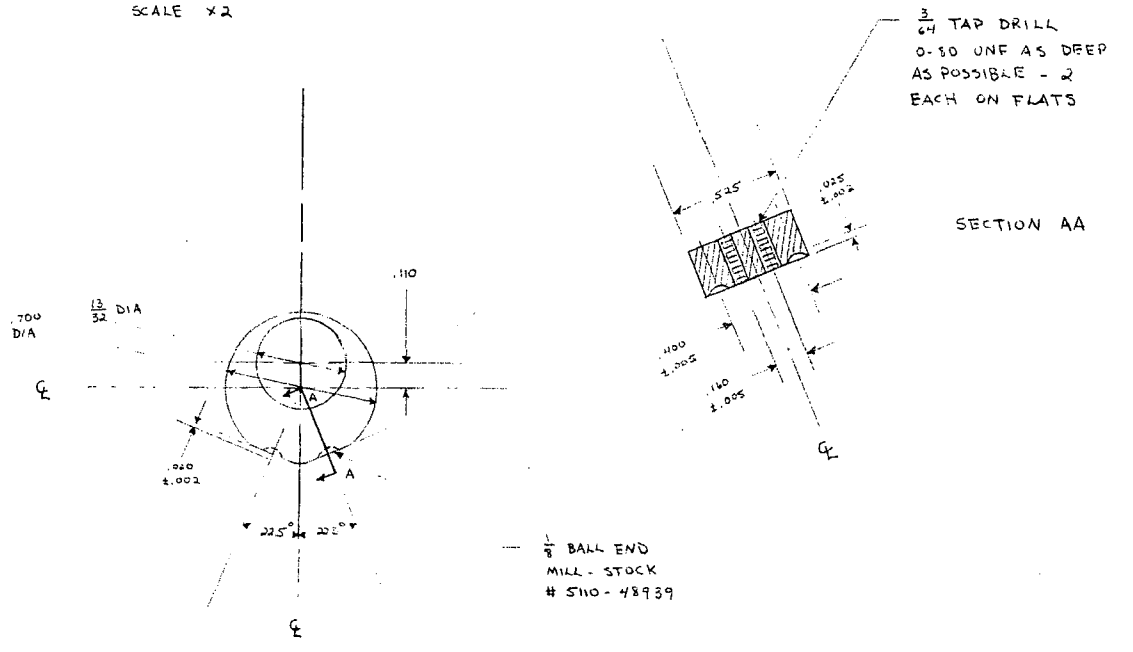

UHV STM SAMPLE HOLDER	REV. 2
304 SS	1 EA
OCTOBER 30, 1988	
D.M. Zoglinski	
ALL DIMENSIONS ±0.010 EXCEPT WHERE INDICATED	

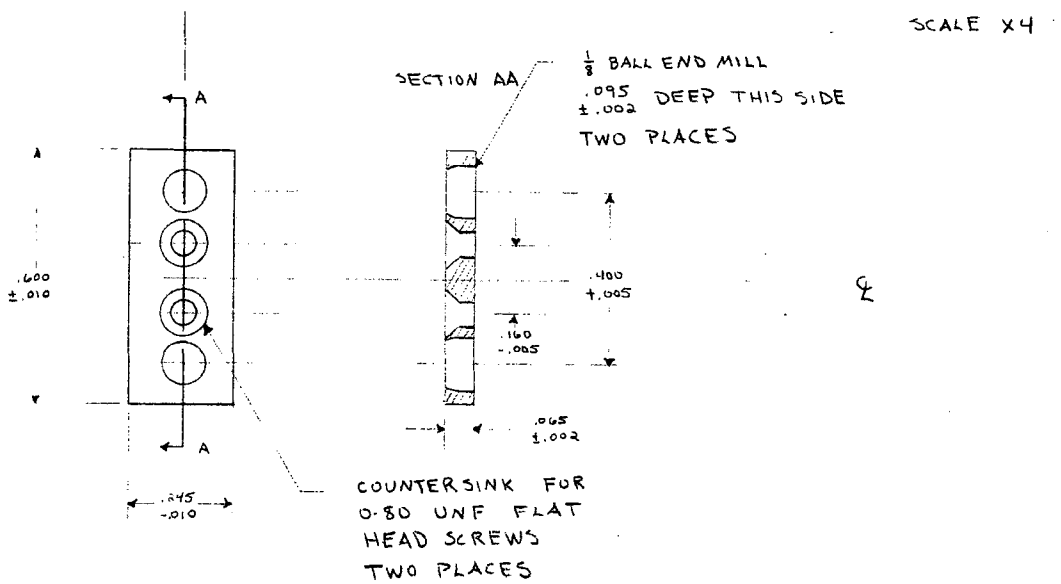

UHV STM SAMPLE HOLDER
RETAINING PLATES
304 SS 2 EA
OCTOBER 13, 1988
D. M. Zeglinski

S.T.M. 05/01/87 W.Wong

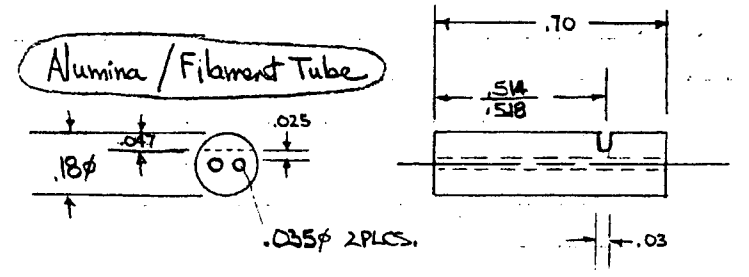

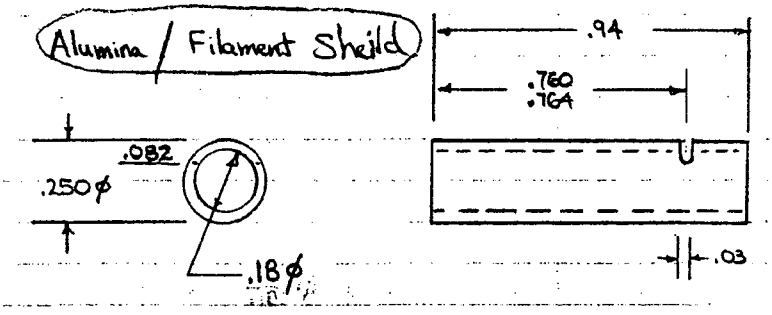

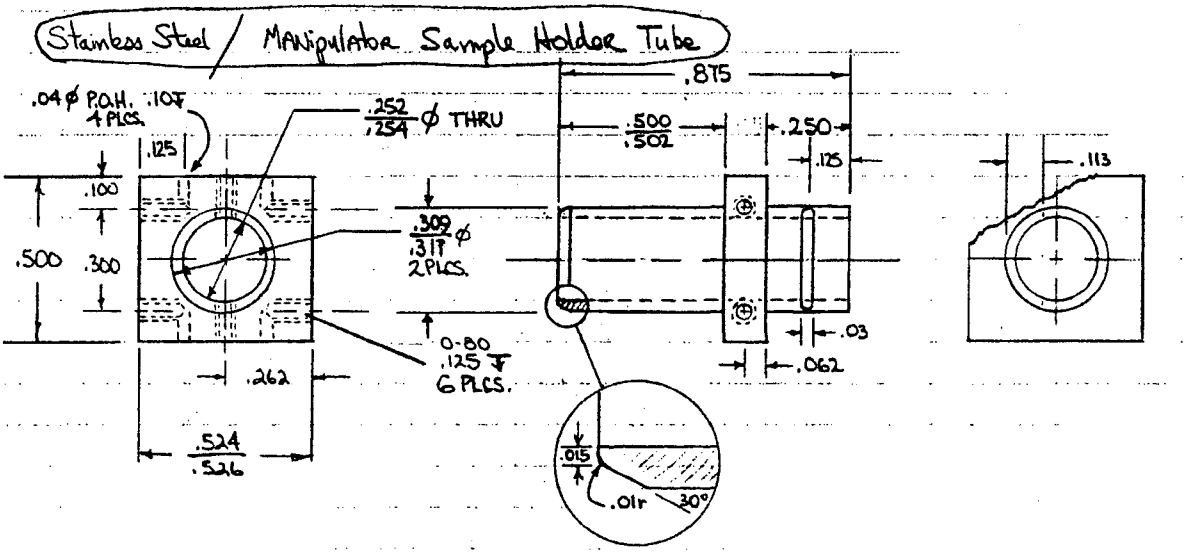

LAWRENCE BERKELEY LABORATORY
CENTER FOR ADVANCED MATERIALS
1 CYCLOTRON ROAD
BERKELEY, CALIFORNIA 94720